

INVESTIGATION AND COMPARISON OF THE THERAPEUTIC EFFECTS  
OF PALBOCICLIB-LOADED MAGNETIC NANOPARTICLES ON 2D, 3D  
AND EX-VIVO BREAST CANCER MODELS

A THESIS SUBMITTED TO  
THE GRADUATE SCHOOL OF NATURAL AND APPLIED SCIENCES  
OF  
MIDDLE EAST TECHNICAL UNIVERSITY

BY

MARYAM PARSIAN

IN PARTIAL FULFILLMENT OF THE REQUIREMENTS  
FOR  
THE DEGREE OF DOCTOR OF PHILOSOPHY  
IN  
BIOTECHNOLOGY

AUGUST 2022



Approval of the thesis:

**INVESTIGATION AND COMPARISON OF THE THERAPEUTIC  
EFFECTS OF PALBOCICLIB LOADED MAGNETIC NANOPARTICLES  
ON 2D, 3D AND EX-VIVO BREAST CANCER MODELS**

submitted by **MARYAM PARSIAN** in partial fulfillment of the requirements for  
the degree of **Doctor of Philosophy in Biotechnology, Middle East Technical  
University** by,

Prof. Dr. Halil Kalıpçılar  
Dean, Graduate School of **Natural and Applied Sciences** \_\_\_\_\_

Assoc. Prof. Dr. Yesim Soyer  
Head of the Department, **Biotechnology** \_\_\_\_\_

Assoc. Prof. Dr. Can Ozen  
Supervisor, **Biotechnology, METU** \_\_\_\_\_

Prof. Dr. Ufuk Gunduz  
Co-Supervisor, **Biotechnology, METU** \_\_\_\_\_

**Examining Committee Members:**

Assoc. Prof. Dr. Pelin Mutlu  
Biotechnology Dep., Ankara University \_\_\_\_\_

Assoc. Prof. Dr. Can Ozen  
Biotechnology Dep., METU \_\_\_\_\_

Assoc. Prof. Dr. Bala Gur Dedeoglu  
Biotechnology Dep., Ankara University \_\_\_\_\_

Assist. Prof. Dr. Ahmet Acar  
Biology Dep., METU \_\_\_\_\_

Assoc. Prof. Dr. Ender Yildirim  
Mechanical Engineering Dep., METU. \_\_\_\_\_

Date: 03.08.2022

**I hereby declare that all information in this document has been obtained and presented in accordance with academic rules and ethical conduct. I also declare that, as required by these rules and conduct, I have fully cited and referenced all material and results that are not original to this work.**

Name Last name: Maryam Parsian

Signature:



## ABSTRACT

### INVESTIGATION AND COMPARISON OF THE THERAPEUTIC EFFECTS OF PALBOCICLIB-LOADED MAGNETIC NANOPARTICLES ON 2D, 3D AND EX-VIVO BREAST CANCER MODELS

Parsian Maryam  
Doctor of Philosophy, Biotechnology  
Supervisor: Assoc. Prof. Dr. Can Ozen  
Co-Supervisor: Prof. Dr. Ufuk Gunduz

August 2022, 140 pages

The development of new tissue culture models is needed in cancer research and personalized medicine to better predict patients' responses to treatment. Using live tumor cells as a testing platform for drug development and identifying optimal therapy is a promising strategy. We described a new tissue culture approach that combines a microfluidic chip with the micro-dissected breast cancer tumor slices. The tumors from MDA-MB-231, SKBR-3, and MCF-7 cell lines were created in CD1 nude mice cultured in this microfluidic chip as an ex vivo culture. 'Tumor-on-a-chip' devices are suitable for precision medicine since the viability of tissue samples is maintained during the culture period by continuously feeding fresh media and eliminating metabolic wastes from the tissue. This microfluidic system allows living tumor tissue to be kept alive and tested in laboratory conditions for 96 hours.

Traditional chemotherapy methods used in cancer treatment cause side effects and drug resistance, thus reducing treatment efficacy and success. Therefore, in recent years, efforts have been focused on drug targeting and controlled drug release systems in cancer treatment. Nano-sized iron oxide particles have gained

importance in drug targeting and controlled release due to their targetability under a magnetic field. Palbociclib (Ibrance®) is a chemotherapeutic agent used to treat ER-positive and HER-negative metastatic breast cancer.

Synthesis of PAMAM dendrimer coated magnetic nanoparticles (DcMNPs) was followed by conjugation of Palbociclib to the nanoparticles and characterization. The cytotoxicity of Palbociclib and Palbociclib conjugated magnetic nanoparticles were examined and compared on the breast cancer cells in the 2D, 3D (hanging droplet method, and ex-vivo cultures. The confocal microscopy images revealed bare magnetic nanoparticles' uptake and internalization differences in three cultural methods. These analyses have shown that nanoparticles can be targeted in the presence of magnets and can penetrate into the interior parts in 3D and ex vivo cultures.

It is known that the cells grown in 3D culture have different morphology and gene expression profiles when compared to cells in 2D culture. The changes in the expression levels of genes related to breast cancer development after applying Palbociclib conjugated DcMNP or free Palbociclib to 2D, 3D, and ex vivo cultures were investigated by the qRT-PCR method. Studies in 3D and ex-vivo environments will give rise to the development of rapid diagnostic and targeted personalized chemotherapy methods when performed with tumor specimens taken from the patients.

Keywords: Ex-vivo culture, Microfluidics, 3D culture, Magnetic PAMAM dendrimer, Palbociclib

## ÖZ

# **PALBOCİCLİB YÜKLÜ MANYETİK NANOPARÇACIKLARIN 2D, 3D VE EX-VİVO MEME KANSERİ MODELLERİ ÜZERİNDEKİ TERAPÖTİK ETKİSİNİN MOLEKÜLER DÜZEYDE İNCELENMESİ VE KARŞILAŞTIRILMASI**

Parsian, Maryam  
Doktora, Biyoteknoloji  
Tez Yöneticisi: Doç. Dr. Can Ozen  
Ortak Tez Yöneticisi: Prof. Dr. Ufuk Gündüz

Ağustos 2022, 140 sayfa

Hastaların tedaviye yanıtlarını daha iyi tahmin etmek için kanser arařtırmalarında ve kişiselleřtirilmiř tıpta yeni doku kültürü modellerinin geliřtirilmesine ihtiyaç vardır. İlaç geliřtirme ve optimal tedavinin belirlenmesi için bir test platformu olarak canlı tümör hücrelerinin kullanılması umut verici bir stratejidir. Mikrodisseke meme kanseri tümör dilimleri ile mikroakıřkan çipi birleřtiren yeni bir doku kültürü yaklařımını tanımladık. MDA-MB-231, SKBR-3 ve MCF-7 hücre çizgilerinden gelen tümörler, bir ex vivo kültür olarak bu mikroakıřkan çipte kültürlenerek CD1 çıplak farelerde yaratıldı. 'Çipte tümör' cihazları hassas tıp için uygundur çünkü doku örneklerinin canlılıęı kültür periyodu boyunca sürekli olarak taze besiyeri besleyerek ve dokudaki metabolik atıkları ortadan kaldırarak korunur. Bu mikroakıřkan sistem, canlı tümör dokusunun canlı tutulmasına ve 96 saat laboratuvar kořullarında test edilmesine olanak tanır.

Hastaların tedaviye yanıtlarını daha iyi tahmin etmek için kanser arařtırmalarında ve kiřiselleřtirilmiř tıpta yeni doku kùltürü modellerinin geliřtirilmesine ihtiyaç vardır. İlaç geliřtirme ve optimal tedavinin belirlenmesi için bir test platformu olarak canlı tümör hücrelerinin kullanılması umut verici bir stratejidir. Mikrodisseke meme kanseri tümör dilimleri ile mikroakıřkan çipi birleřtiren yeni bir doku kùltürü yaklařımını tanımladık. MDA-MB-231, SKBR-3 ve MCF-7 hücre hatlarından CD1 çıplak farelerde oluřturulan tümörler, ex vivo kùltür olarak mikroakıřkan çiplerde kùltürlendi. 'Çipte tümör' cihazları hassas tıp için uygundur çünkü doku örneklerinin canlılıęı kùltür periyodu boyunca sürekli olarak taze besiyeri ile beslenerek ve dokudaki metabolik atıkları ortadan kaldırılarak korunur. Bu mikroakıřkan sistem, canlı tümör dokusunun canlı tutulmasına ve 96 saat laboratuvar kořullarında test edilmesine olanak tanır.

Kanser tedavisinde kullanılan geleneksel kemoterapi yöntemleri yan etkilere ve ilaç direncine neden olarak tedavi etkinlięini ve bařarısını azaltmaktadır. Bu nedenle son yıllarda kanser tedavisinde ilaç hedefleme ve kontrollü ilaç salım sistemleri üzerine çalıřmalar yoęunlařmıřtır. Nano boyutlu demir oksit (manyetit, Fe<sub>3</sub>O<sub>4</sub>) parçacıklar, manyetik alan altında hedeflenebilir olmaları nedeniyle ilaç hedeflemede ve kontrollü salımda önem kazanmıřtır.

Palbociclib (Ibrance®), ER-pozitif ve HER-negatif metastatik meme kanserini tedavi etmek için kullanılan bir kemoterapötik ajandır.

Bu çalıřmada PAMAM dendrimer kaplı manyetik nanopartiküllerin (DcMNP'ler) sentezlendi, Palbociclib'in nanopartiküllere konjugasyonu ve karakterizasyonu gerçekteřtirildi. Palbociclib ve Palbociclib konjuge manyetik nanopartiküllerin sitotoksitesisi, 2D, 3D (asılı damlacık yöntemi ve ex-vivo kùltürlerde) meme kanseri hücreleri üzerinde incelenerek ve karřılařtırıldı. Konfokal mikroskopi görüntüleri, üç kùltür yönteminde çıplak manyetik nanoparçacıkların alım ve içselleřtirme farklılıklarını ortaya çıkardı. Manyetik alan varlıęında

nanoparçacıkların hedeflenebildiği, 3D ve ex vivo tümör dokusunda iç kesimlere kadar girebildiği gösterildi.

3D kültürde üretilen hücrelerin, 2D kültürdeki hücelere kıyasla farklı morfoloji ve gen ekspresyon profillerine sahip olduğu bilinmektedir. Nanoparçacıklara bağlı veya serbest Palbosiklib'in 2D, 3D ve ex vivo kültürlerine uygulandıktan sonra meme kanseri gelişimi ile ilgili olan genlerin ifade düzeylerinde meydana getirdiği değişiklikler qRT-PCR yöntemi ile incelenmiştir. 3D ve ex-vivo ortamlardaki çalışmalar, hastalardan alınan tümör örnekleri ile yapıldığında hızlı tanısal ve hedefe yönelik kişiye özel kemoterapi yöntemlerinin geliştirilmesine ışık tutacaktır.

Anahtar Kelimeler: Ex-vivo kültür, Mikroakışkanlar, 3D kültür, Manyetik PAMAM dendrimer, Palbosiklib.

Dedicated to  
To my father, who always believed in me  
but never saw this adventure.

## ACKNOWLEDGMENTS

First of all, I would like to express my deepest gratitude to my supervisors Prof. Dr. Ufuk Gündüz, and Assoc. Prof. Dr. Can Ozen, for their excellent academic guidance, advice, great support, and encouragement throughout this study.

I would like to thank my examining committee members, Assoc. Prof. Dr. Ender Yildirim, Assoc. Prof. Dr. Pelin Mutlu, Assoc. Prof. Dr. Bala Gur Dedeoglu, and Assist. Prof. Dr. Ahmet Acar for their kind participation and valuable comments during this research.

This thesis would not progress or come to an end if it was not for the comprehensive and consistent support, encouragement, as well as kind and pleasant collaboration, and encouraging comments of the thesis study from Assoc. Prof. Dr. Pelin Mutlu and Assoc. Prof. Dr. Ender Yildirim. I could not ask for better mentors who are so full of wisdom, kindness, and humor. Now that I am closing this section of my life and career, all the long way through this challenging way, they were not merely mentoring me; I actually learned from them how being a good human being is more valuable and then you will become the best in whatever you are doing.

I would like to express my heartfelt gratitude to Ali Can Atik and Nalan Kamaly for their help during my thesis experiments. I am always grateful to them. I would like to thank Dr. Nusret Taheri and Assoc. Prof. Dr. Serap Yalcin for technical assistance.

I am deeply thankful to Assist. Prof. Dr. Negar Taghavi, Dr. Çağrı Urfalı, Ayca Nabioglu, and Esra Metin, the members of Lab 206 (D. K.) for their help,

friendship, and contributions throughout my study. Those were the days when it was fun to go to the “Çardak.”

It has been a blessing to be surrounded by wonderful friends whose companionship is as precious as my loved ones. My time in Ankara became meaningful with my good friends and several invaluable friendships. Special thanks to my good friends Farnaz Kimya, Dr. Maryam Najafi, Dr. Elmira pourreza, Parinaz Ashrafi, Raha Shabani, Neda Esmailzadeh, Dr. Shabnam Mehrdash, Ali Rad Yousefnia, Assoc. Prof. Dr. Metin Yuksel, Assist. Prof. Dr. Atefeh Lafzi, Sahar Habibi, and Nima Bonyadi for their priceless company and help during my study and living in Turkey.

I would like to express my wholehearted appreciation and thanks to my mother, Mansoreh Zargar Salehi, my sister Farzaneh Parsian and my brother Amir Parsian, my brother and sister-in-law, Jalil Jodeiri Rad and Sima Gerami, for their endless love, trust, and support in every step of my life. Special thanks to my nephew and nieces, Ata Jodeyri Rad, Mahya Jodeyri Rad, and Asal Parsian, for their persuasion and encouragement. It was delightful to see their successes and robust growth, even from long distances. So you know that I will always be with you. I also want to extend a special thank you to Mahya, a young, beautiful scholar who I am confident will make a significant contribution to the world.



## TABLE OF CONTENTS

|  |      |
|--|------|
| ABSTRACT.....  | v    |
| ÖZ.....  | vii  |
| ACKNOWLEDGMENTS .....  | xi   |
| TABLE OF CONTENTS.....   | xiii |
| LIST OF TABLES .....   | xvi  |
| LIST OF FIGURES .....  | xvii |
| LIST OF ABBREVIATIONS.....   | xxi  |
| 1 CHAPTER 1 .....  | 1    |
| INTRODUCTION   |      |
| 1.1 Microfluidic Devices .....   | 1    |
| 1.2 Breast Cancer .....  | 3    |
| 1.3 Chemotherapy .....   | 4    |
| 1.4 Palbociclib.....   | 5    |
| 1.5 Targeting Therapy.....   | 7    |
| 1.6 2D vs. 3D Cell Cultures .....  | 9    |
| 1.7 Ex-vivo Cultures .....   | 11   |
| 1.8 Objective of the Thesis: .....   | 12   |
| 2 CHAPTER 2 .....  | 15   |
| DEVELOPMENT OF A MICROFLUIDIC PLATFORM TO MAINTAIN<br>VIABILITY OF MICRO-DISSECTED TUMOR SLICES IN CULTURE |      |

|       |   |    |
|-------|---|----|
| 2.1   | Experimental Section.....   | 16 |
| 2.1.1 | The Microfluidic Chip Design.....   | 16 |
| 2.1.2 | Mold and PDMS Device Fabrication .....  | 21 |
| 2.2   | Ex-vivo Breast Cancer Models.....   | 24 |
| 2.2.1 | Preparation and Injection of Cells for In-vivo Culture.....                                   | 24 |
| 2.2.2 | Preparation of the Tumors and Micro-dissected Tumor Slices .....                              | 24 |
| 2.2.3 | Culture of Micro-dissected Tissues .....  | 27 |
| 2.3   | Results & Discussion.....   | 31 |
| 2.3.1 | Tumor Tissue Analyses by Hematoxylin-Eosin Staining .....                                     | 31 |
| 2.3.2 | Assessment of Cell Viability of Micro-dissected Tissue Cultures .....                         | 32 |
| 2.3.3 | Mass Transfer Analysis of Oxygen and Carbon Dioxide.....                                      | 34 |
| 2.3.4 | Micro-dissected Tumor Slice Viability Analysis .....  | 36 |
| 2.4   | Conclusion:.....  | 41 |
| 3     | CHAPTER 3 .....   | 43 |
|       | PALBOCICLIB CONTAINING MAGNETIC PAMAM DENDRIMERS:<br>CONJUGATION AND CHARACTERIZATION STUDIES |    |
| 3.1   | Experimental Section.....   | 44 |
| 3.1.1 | Synthesis of Magnetic PAMAM Dendrimers .....  | 44 |
| 3.1.2 | Loading of Palbociclib on Magnetic PAMAM Nanoparticles (DcMNPs) ....                          | 44 |
| 3.1.3 | Synthesis of Magnetic PAMAM-Palbociclib Conjugate .....                                       | 45 |
| 3.1.4 | Characterization of Drug Conjugated DcMNPs.....   | 46 |
| 3.2   | Results & Discussions .....   | 47 |
| 3.2.1 | Loading and Conjugation of Palbociclib on Magnetic PAMAM Dendrimer                            | 47 |
| 3.2.2 | Characterization of Palbociclib Conjugated G5.5 PAMAM DcMNPs .....                            | 51 |

|       |  |     |
|-------|--|-----|
| 3.3   | Conclusion: .....  | 55  |
| 4     | CHAPTER 4 .....  | 57  |
|       | COMPARISON OF THE THERAPEUTIC EFFECTS OF PALBOCICLIB<br>AND PALBOCICLIB CONJUGATED MAGNETIC NANOPARTICLES<br>ON 2D, 3D, AND EX-VIVO BREAST CANCER MODELS |     |
| 4.1   | Experimental Section .....   | 58  |
| 4.1.1 | Cell Culture (2D culture) .....  | 58  |
| 4.1.2 | Three-dimensional (3D) Hanging Drop Culture Method .....   | 62  |
| 4.1.3 | Ex-vivo Culture.....   | 66  |
| 4.2   | Results and Discussions.....   | 71  |
| 4.2.1 | 2D Culture Results .....   | 71  |
| 4.2.2 | 3D Hanging Droplet Results.....  | 83  |
| 4.2.3 | Ex-vivo Culture Results.....   | 99  |
| 4.3   | Conclusion .....   | 113 |
| 5     | CHAPTER 5 .....  | 115 |
|       | CONCLUDING REMARKS   |     |
| 6     | REFERENCES .....   | 120 |
| A.    | Measuring Cell Death by Propidium Iodide (PI) Uptake .....   | 131 |
| B.    | Anticancer Drug Sensitivity Testing in MCF-7 Ex-vivo Cultures .....  | 132 |
| C.    | MCF-7 ex-vivo culture RT-PCR results .....   | 133 |
|       | CURRICULUM VITAE.....  | 135 |

## LIST OF TABLES

### TABLES

|   |    |
|---|----|
| Table 3.3.1. HPLC result for PAL-PAMAM conjugation. ....  | 50 |
| Table 3.3.2. The comparison of different drug loading and conjugation methods in terms of drug payload in DcMNPs..... | 50 |

## LIST OF FIGURES

### FIGURES

|   |    |
|---|----|
| Figure 1.1. An example of a microfluidic device. ....   | 1  |
| Figure 1.2. Schematic views of Organ-on-a-chip platforms.....   | 2  |
| Figure 1.3. The relative grading, molecular stratification, therapy requirement, and prognosis.....   | 4  |
| Figure 1.4. Palbociclib mechanism of action.....  | 6  |
| Figure 1.5. A schematic representation for smart nanoplateforms.. ....  | 8  |
| Figure 1.6. Representation of human, in vitro 2D, 3D, and organ-on-a-chip systems and current issues. ....  | 10 |
| Figure 1.7. The hanging drop method.....  | 11 |
| Figure 2.1. Schematic representation of the microfluidic chip used in tumor viability analysis. ....  | 16 |
| Figure 2.2. Microfluidic chip composition. ....   | 17 |
| Figure 2.3. Flow profiles were obtained using COMSOL Multiphysics.....  | 18 |
| Figure 2.4. Description of the domains and the boundary conditions. ....  | 19 |
| Figure 2.5. Electrical circuit analogy of the microfluidic network.....   | 20 |
| Figure 2.6. Brass molds Fabrication .....   | 21 |
| Figure 2.7. Schematic view of PDMS molding method .....   | 22 |
| Figure 2.8. Photograph of a PDMS chip sandwiched by PMMA slide layers by using binder clips. ....   | 23 |
| Figure 2.9. Developing breast cancer model in Cd-1 nude mice.....   | 25 |
| Figure 2.10. (A) Tumor size measurements with Vernier caliper, (B) Embedding of tumor in the low melting agarose before slicing, (C) Slicing of a tumor by Vibratome, and (D) Tumor slice (~350µm)..... | 26 |
| Figure 2.11. Representative scheme of ex-vivo culture arrangement.....  | 27 |
| Figure 2.12. Overview of incubators and placement of chips inside incubators. ...   | 28 |
| Figure 2.13. Well-plate culture system. ....  | 29 |

|   |    |
|---|----|
| Figure 2.14. A) MDA-MB-231 tumor image under a stereo microscope, B) H&E images of MDA-MB-231 tumor slice sections on the first day. ....                   | 31 |
| Figure 2.15. Confocal imaging and maximum intensity projection of MDA-MB-231 micro-dissected tissues. ....  | 33 |
| Figure 2.16. The mean sum intensities of MDA-MB-231 (A) and SKBR-3 (B) tumors from three different positions of two slices of micro-dissected tissues ..... | 34 |
| Figure 2.17. Comparison of the amount of LDH released from MDA-MB-231 tissues in the microfluidic and well-plate system over four days.....                 | 37 |
| Figure 2.18. LDH release from SKBR-3 tissues at microfluidic and well-plate systems. ....   | 39 |
| Figure 2.19. Comparison of the metabolic activity of the tumor slices in microfluidic and well-plate systems in terms of glucose consumption.....           | 40 |
| Figure 3.1. Schematic for Palbociclib-Succinic acid- G5.5 PAMAM conjugation.  | 46 |
| Figure 3.2. FTIR spectra.....   | 51 |
| Figure 3.3. Zeta potential.....   | 53 |
| Figure 3.4. TEM images.....   | 53 |
| Figure 3.5. SEM images .....  | 54 |
| Figure 4.1. Spheroid images in the hanging drop method.....   | 62 |
| Figure 4.2. Schematic view of the microfluidic system. ....   | 66 |
| Figure 4.3. A) Schematic, B) real representation of microfluidic chips' incubation systems. ....  | 67 |
| Figure 4.4. Cellular uptake of FITC-DcMNPs by MCF-7 cells by confocal microscopy. ....  | 71 |
| Figure 4.5. Cellular uptake of fluorescent DcMNPs .....   | 72 |
| Figure 4.6. Density plot of SSC and FSC signals of MCF-7, MDA-MB-231, and SKBR-3 cells.....   | 73 |
| Figure 4.7. Mean SSC signal kinetics of FITS-MNP at MCF-7, MDA-MB-231, and SKBR-3 cells. ....   | 74 |
| Figure 4.8. Intensity analysis at different incubation times for MCF-7, MDA-MB-231, and SKBR-3 cell lines .....   | 74 |

|  |     |
|--|-----|
| Figure 4.9. LDH activity .....   | 75  |
| Figure 4.10. CellTiter-Glo® Cell Viability Assay.....  | 77  |
| Figure 4.11. Bax/Bcl-2 gene expression ratios .....  | 79  |
| Figure 4.12. Expression levels of CDH1 gene.....   | 80  |
| Figure 4.13. Expression levels of MDR1 gene .....  | 82  |
| Figure 4.14. Expression levels of mTOR gene.....   | 83  |
| Figure 4.15. The Size and Viability image at different depths of 3D A) MCF-7, B) SKBR-3, and C) MDA-MB-231 by confocal microscopy. ....        | 85  |
| Figure 4.16. Confocal images of internalization of fluorescently labeled DcMNPs into 3D-MCF-7 spheroids after 96 hours.....                    | 87  |
| Figure 4.17. Confocal images of internalization of fluorescently labeled DcMNPs into 3D-MDA-MB-231 spheroids after 96 hours. ....              | 88  |
| Figure 4.18. Confocal images of internalization of fluorescently labeled DcMNPs into 3D-SKBR-3 spheroids after 96 hours.....                   | 89  |
| Figure 4.19. Confocal images of Palbociclib and PAL-DcMNPs treated 3D MCF-7 cells stained with FDA and PI. ....                                | 91  |
| Figure 4.20. Confocal images of Palbociclib and PAL-DcMNPs treated 3D SKBR-3 cells stained with FDA and PI. ....                               | 92  |
| Figure 4.21. Confocal images of control and Palbociclib treated 3D MDA-MB-231 cells stained with FDA and PI. ....                              | 93  |
| Figure 4.22. CellTiter-Glo® 3D Cell Viability Assay.....   | 94  |
| Figure 4.23. LDH activity .....  | 95  |
| Figure 4.24. Expression levels of IL6 genes.....   | 96  |
| Figure 4.25. Expression levels of IL8 genes.....   | 97  |
| Figure 4.26. Bax/Bcl-2 gene expression ratios .....  | 98  |
| Figure 4.27. Expression levels of BRCA1 genes.....   | 98  |
| Figure 4.28. Confocal microscope images of FITC-DcMNPs internalization in microdissected slices in the microfluidic system after 24 hours..... | 101 |
| Figure 4.29. The mean sum intensities of MDA-MB-231 (A) and SKBR-3 (B) tumors. ....  | 103 |

|   |     |
|---|-----|
| Figure 4.30. Confocal imaging and maximum intensity projection of MDA-MB-231 micro-dissected tissues. ....    | 103 |
| Figure 4.31. Confocal imaging and maximum intensity projection of SKBR-3 micro-dissected tissues. ....        | 104 |
| Figure 4.32. LDH release from tumor sections formed with SKBR-3 cells. ....                                   | 106 |
| Figure 4.33. LDH release from tumor formed with MDA-MB-231 cells. ....  | 106 |
| Figure 4.34. Glucose consumption on MDA-MB-231 SKBR-3 tissues at the tissues of the microfluidic system. .... | 108 |
| Figure 4.35: Expression levels of Bcl2 genes .....  | 109 |
| Figure 4.36: Expression levels of IL6 genes .....   | 110 |
| Figure 4.37: Expression levels of BRCA1 genes .....   | 111 |
| Figure 4.38: Expression levels of MDR1 genes.....   | 112 |



## LIST OF ABBREVIATIONS

### ABBREVIATIONS

|                   |   |
|-------------------|---|
| <b>BAX</b>        | Bcl-2 Associated X Protein                      |
| <b>BCL-2</b>      | B-Cell Lymphoma 2                               |
| <b>BRCA1</b>      | Breast Cancer Susceptibility Gene 1             |
| <b>CDH1</b>       | E-Cadherin 1                                    |
| <b>DOX</b>        | Doxorubicin                                     |
| <b>DMSO</b>       | Dimethyl Sulfoxide                              |
| <b>EDC</b>        | N -ethylcarbodiimide hydrochloride              |
| <b>ECM</b>        | Extra cellular Matrix                           |
| <b>FDA</b>        | Fluorescein Diacetate                           |
| <b>IL-6</b>       | Interleukin 6                                   |
| <b>IL-8</b>       | Interleukin 8                                   |
| <b>LDH</b>        | Lactate Dehydrogenase                           |
| <b>MF</b>         | Microfluidic                                    |
| <b>MIP</b>        | Maximum Intensity Projection                    |
| <b>MDR1</b>       | Multi-Drug Resistance 1                         |
| <b>MNP</b>        | Magnetic Nanoparticle                           |
| <b>mTOR</b>       | Mammalian Target Of Rapamycin                   |
| <b>PAL</b>        | Palbociclib                                     |
| <b>PAL-DcMNPs</b> | Palbociclib Conjugated Magnetic PAMAM Dendrimer |
| <b>PAMAM</b>      | Poly Amidoamine                                 |
| <b>PBS</b>        | Phosphate Buffer Saline                         |
| <b>PCTE</b>       | Polycarbonate Membrane Filters                  |
| <b>PDMS</b>       | Polydimethylsiloxane                            |
| <b>PI</b>         | Propidium Iodide                                |
| <b>P53</b>        | Tumor protein 53                                |
| <b>SA</b>         | Succinic acid                                   |



# CHAPTER 1

## INTRODUCTION

### 1.1 Microfluidic Devices

Microfluidic devices have become very useful for studying biological tissues, liquid biopsy, and simulating tissues and organs<sup>1-2-3</sup>. Basically, microfluidics relates to the development of devices that move or analyze tiny amounts of liquid that are smaller than a droplet. Microfluidic devices are characterized by microchannels with diameters ranging from submicron, as nanofluidics, to a few millimeters. Due to the ability to conduct accurate and controlled experiments at a lower cost and faster pace, microfluidics has become increasingly popular in biology<sup>4</sup>. Microfluidic systems can analyze samples by only a few sample handling steps with less volume, chemicals, and reagents, leading to a reduction in global costs and a faster pace of application<sup>5</sup>.

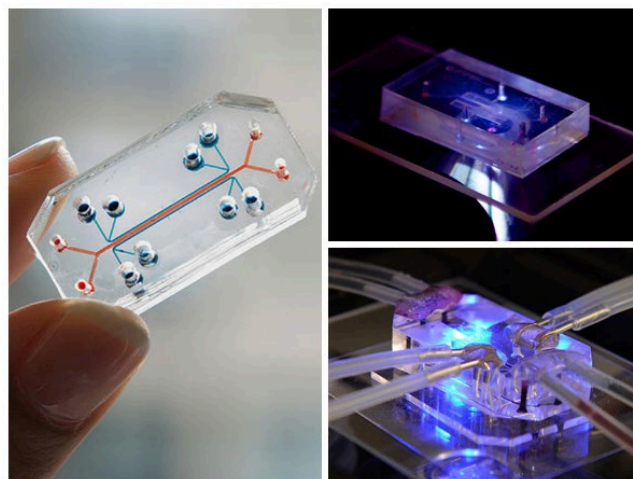


Figure 1.1. An example of a microfluidic device. (Photos: National Center for Advancing Translational Sciences)

The microfluidic devices better mimic the in vivo environment than traditional in vitro culture methods, and research is moving towards developing a "human-on-a-chip" that enables fluid contact between tissues or organ-mimicking cell structures on a microfluidic platform<sup>6-7</sup>. Tissue-on-a-chip devices developed for culture-on-chip tissue biopsy, toxicity studies, separation and detection of antibody-labeled cells from tumor cells, perfusion of living heart tissue by electrochemical monitoring, and examination of radiation-induced cell death in tissue<sup>6-8-9-10</sup>. Thus, the importance of long-term culture with sufficient nutrients, oxygen, and better handling of waste products in microfluidic devices is beginning to be recognized<sup>8-11-12-13</sup>.

A microfabricated chip made of polydimethylsiloxane (PDMS) containing an array of microchannels etched or molded into it can act as a culture vessel for cells and easily accommodate medium flow or circulation. In addition, tissue pieces, such as tumor slices, were cultured in microfluidic devices to better preserve their function than traditional culture methods<sup>14-15</sup>.

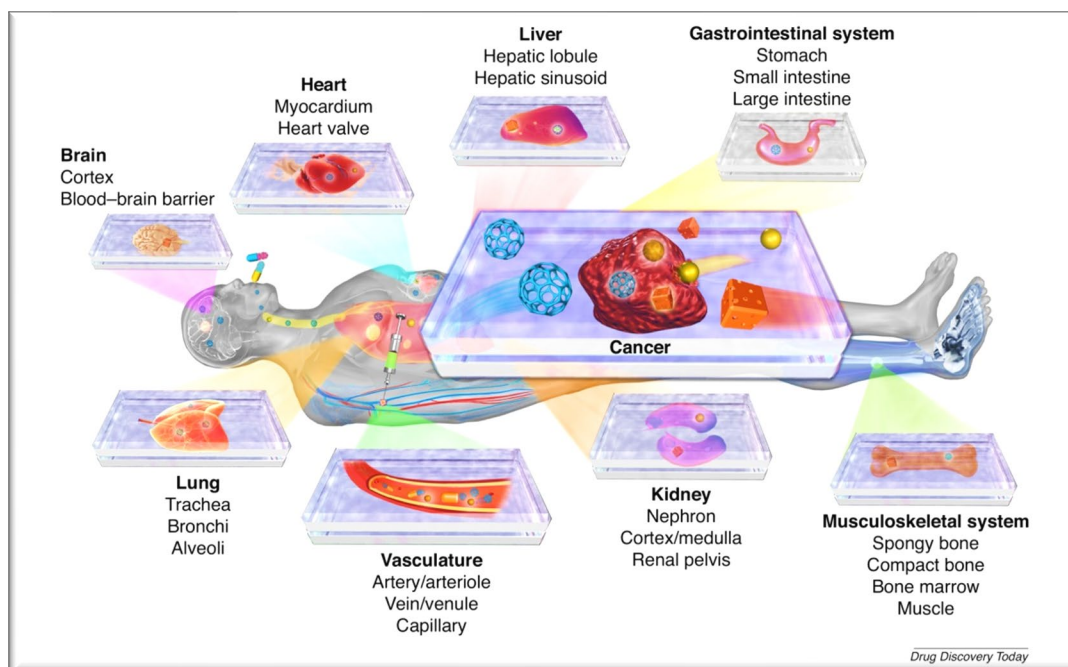


Figure 1.2. Schematic views of Organ-on-a-chip platforms used for personalized medicine and drug screening<sup>16</sup>.

A promising alternative would be directly testing alternative drugs on small amounts of cancer tissue taken from patients inside microfluidic biochips. For instance, patient-derived liver and colorectal carcinoma models are used for drug screening processes by cancer-on-a-chip platforms<sup>17-18</sup>. In addition, developing detection methods to measure the viability of tissues and chemotherapy testing simultaneously are novel approaches in 3D ex-vivo tissue culture from patients<sup>9-19</sup>.

## **1.2 Breast Cancer**

Recent statistics from the World Health Organization (WHO) report indicate that cancer is the leading cause of death, with an estimated ten million deaths per year worldwide<sup>20</sup>. Among the different types of cancers, breast cancer is known to be the most common type of cancer in women all over the world, and its mortality rates are increasing. Numerous histological and immune-molecular studies in the past decade demonstrated that breast cancer is highly heterogeneous. Various biomarkers, including hormonal receptor markers, may be used to detect and treat breast cancer based on its growth pattern, cytological features, and expression of biomarkers. However, the FDA has approved only four biomarkers for detecting breast cancer in body fluids; cancer antigens (CA 15-3 and CA 27-29), human epidermal growth factor receptor 2 (HER2), and circulating tumor cells (CTC)<sup>21</sup>.

Breast cancer is classified as luminal A and B, normal and basal subtypes due to the progesterone receptor (PR), estrogen receptor (ER), and human epidermal growth factor receptor 2 (HER2)<sup>21-22</sup>. Each subtype has various prognoses and therapeutic sensitivities. The luminal A and luminal B subtypes are ER+ and are responsive to hormone therapy. Also, luminal B and HER2 groups are HER2+ and are potential candidates for Trastuzumab, Lapatinib, and Pertuzumab therapy<sup>23</sup>.

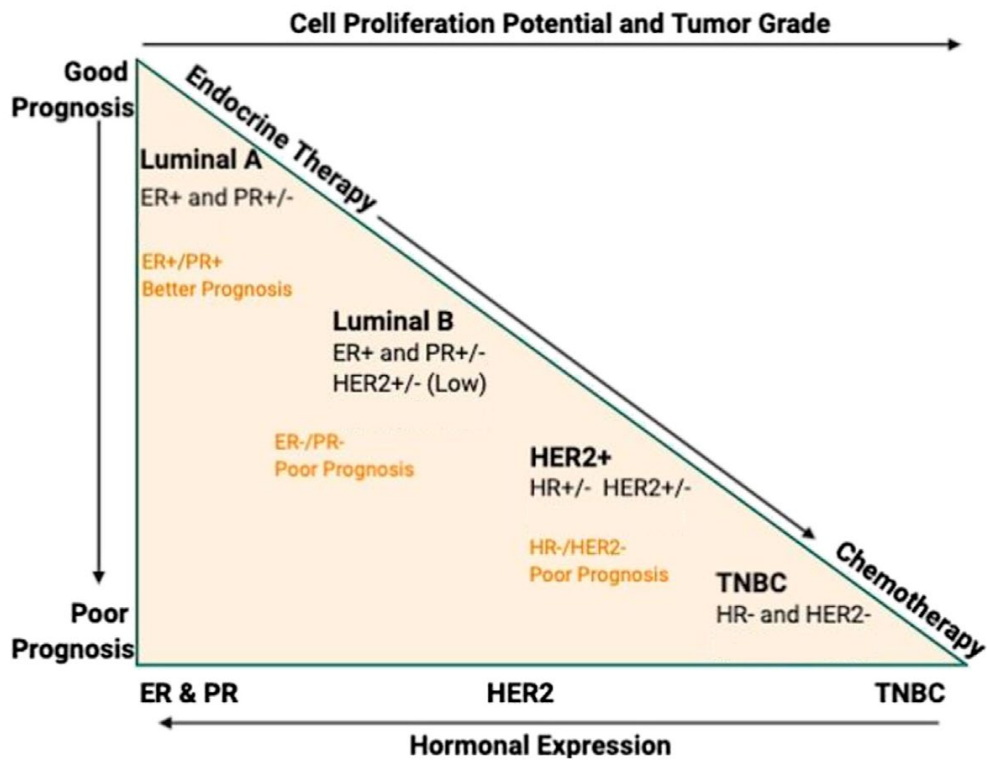


Figure 1.3. The relative grading, molecular stratification, therapy requirement, and prognosis. Cancer grade and cellular proliferation are inversely proportional to breast cancer hormone expression<sup>21</sup>.

The most prevalent therapeutic approaches for breast cancer treatment include chemotherapy, radiation, and surgery<sup>24</sup>. Of these methods, chemotherapy which is frequently used in the treatment of breast cancer, remains the most effective therapy and aims to remove cancerous cells by using cytotoxic agents. However, the chemotherapy regimen is influenced by the cancer subtype, stage, and drug resistance<sup>25</sup>.

### 1.3 Chemotherapy

Chemotherapy, which aims to destroy cancer cells by using cytotoxic agents, is commonly used in breast cancer treatment<sup>26</sup>. Cancer stage and drug resistance are important factors for determining the chemotherapy regimen. Although

chemotherapy has been successful in many aspects, the main problem is the side effects caused in the normal cells and the drug resistance in the cells<sup>27</sup>. Resistance to structurally and functionally unrelated drugs is called multiple drug resistance, a severe problem in chemotherapy applications. Therefore, new generation targeted chemotherapy methods are being used to eliminate these effects<sup>28</sup>.

During the significant progress in cancer treatment over the past few decades, the need for personalized therapies gained much attention<sup>29</sup>. Unfortunately, anticancer drug candidates have a very high attrition rate and only about 5% of drugs successfully complete phase III clinical trials<sup>30</sup>. Besides these problems, a significant number of cancer patients are non-responsive to regular chemotherapy treatment. Furthermore, the adverse side effects of chemotherapy with low clinical benefits are seen in many patients<sup>31</sup>. The lack of relevant models with appropriate human cancer nature and complexity is one of the problems that reduce the development of anticancer therapies. Therefore, developing novel drug testing tools and technologies besides new strategies for efficiently monitoring therapeutic agents is attractive to enhance treatment outcomes and specificity while minimizing toxicity<sup>32-33-5</sup>.

#### **1.4 Palbociclib**

Palbociclib (Ibrance®) is a type of targeted drug agent for treating ER-positive and HER-negative metastatic breast cancer. ER + / HER- metastatic breast cancers constitute sixty percent of metastatic breast cancers. It has been shown that Palbociclib, which is used in this type of advanced and aggressive breast cancer, together with hormone therapy, increases treatment efficiency<sup>34</sup>.

Palbociclib is the first drug approved as an inhibitor of CDK4 and CDK6. It inhibits the proliferation of cancer cells by inhibiting CDK4 and CDK6 from cyclin-dependent kinases. The cell cycle is controlled by cyclin and cyclin-dependent kinases (CDK). The G1-S phase transition is regulated by the interaction

of CDK4/6 kinases with cyclin D. Cyclin D is a direct target for estrogen or other growth factors, and its amount is frequently increased in ER+ breast cancers. By phosphorylating CDK4/6, retinoblastoma protein (Rb) releases the E2F transcription factor, and E2F provides the expression of genes necessary for the G1-S phase transition. Specific inhibitors such as p16, p18, p21, and p27 inhibit CDK4/6<sup>35-36</sup>.

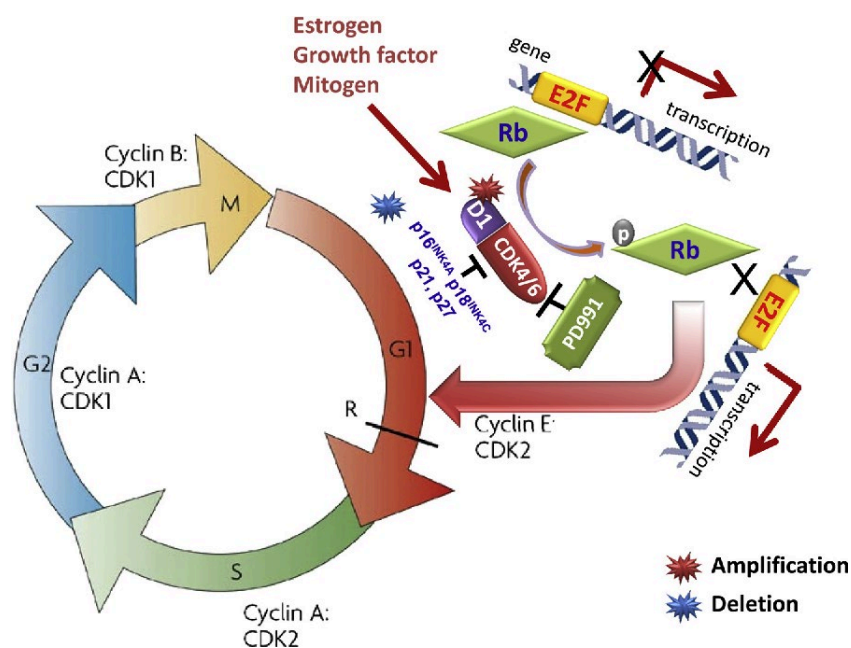


Figure 1.4. Palbociclib mechanism of action<sup>37</sup>.

Palbociclib is also a drug with many side effects, such as other chemotherapeutics. The drug's most common side effects are a reduction in white blood cells, weakness, anemia, upper respiratory tract infection, nausea, wounds in the mouth, thrombocytopenia, peripheral neuropathy, and nosebleeds<sup>34</sup>.

Palbociclib is only very soluble at pH levels below 4.0, and its solubility level is markedly reduced over pH 4.0. To reduce solubility and enhance bioavailability, Palbociclib was formulated with biodegradable chitosan-polypropylene glycol carriers. In vitro studies demonstrated excellent drug release kinetics and biocompatibility for Palbociclib-loaded nanocarriers<sup>38</sup>.



## 1.5 Targeting Therapy

In the battle against malignant tumors, chemotherapy is the most common strategy. Despite chemotherapy applications being successful in many ways; however, it is not trouble-free. The inability of anticancer agents to selectively attack tumor cells remains the most significant obstacle to successful chemotherapy<sup>39</sup>. Also, some primary drawbacks refer to poor solubility, nonspecific delivery, high toxicity, and short circulating half-lives of the drugs<sup>40</sup>. More strategies have been discovered to optimize these drawbacks with an increasing understanding of cancer biology and technological advancements. The expeditious development of nanomedicine relieved the way. It is becoming increasingly common to combine chemotherapy with gene therapies, immunology, and small molecules in order to treat cancer effectively. Encapsulating drugs into various nanocarriers is an ideal approach to combinational therapy and drug delivery systems. Several smart nanoplateforms are being developed that respond to internal stimuli or external stimuli such as changes in enzymes, pH, hypoxia, redox and magnetic field, temperature, light, ultrasound.

Iron oxide-based magnetic nanoparticles (MNPs) have gained importance as drug targeting systems due to their simple structure, easy synthesis, and the ability to alter their properties for different biological purposes. Such nanoparticles carrying anticancer agents can be condensed in tumor cells with the help of an externally applied magnetic field<sup>41</sup>. However, extensive surface modifications are required to increase the stability of the magnetic nanoparticles in the organism and to protect the nanoparticles from attack by the immune system cells. Organic polymers such as poly-amidoamine (PAMAM) dendrimer, polyethylene glycol, chitosan, and aminosilane are widely used polymers for the coating of these nanoparticles<sup>41-42-43</sup>.

Poly-amidoamine (PAMAM) dendrimer is a well-defined, special three-dimensional structure and has a multivalent surface and internal cavities that can play an essential role in drug delivery systems. PAMAM dendrimers are spherically branched polymers with numerous amine or carboxyl-terminal groups capable of forming stable complexes with chemotherapeutic drugs and

oligonucleotides. PAMAM dendrimers are suitable and durable carrier systems with properties such as having nanometer size, controllable molecular weights, biocompatibility, and non-immunogenic properties. Host and guest interaction causes to dramatically an increase in the encapsulation of drugs between branches. Several experiments indicated that higher transfection efficiency and lower toxicity could be obtained by using the completion of DNA with PAMAM, as well as for the completion between siRNA and PAMAM dendrimers<sup>40-44</sup>.

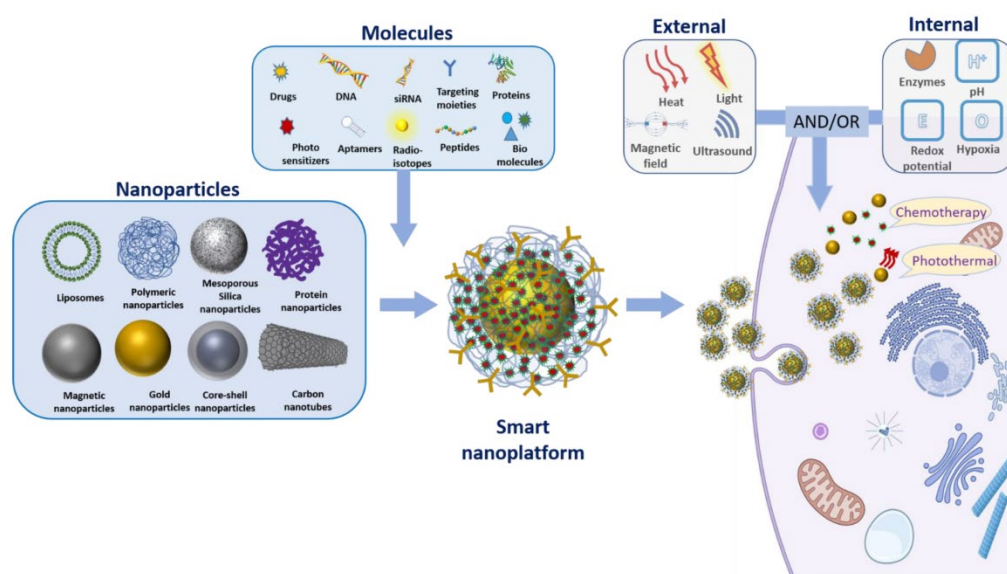


Figure 1.5. A schematic representation for smart nanoplatforms. Different nanoparticles, therapeutic molecules, targeting moieties, and various external or internal stimuli types are often used to develop smart nanoparticles<sup>45</sup>.

The drug conjugated PAMAM dendrimers are pH-sensitive. The polymer rapidly cleaved in acidic pH; however, it was strong enough in physiological conditions. The pH differences between tumors (pH 5.6-6.8) and healthy tissues (pH 7.0-7.4) investigated different microenvironments to release drugs from PAMAM dendrimers. This form of delivery minimizes payload exposure to healthy tissues and maximizes the dose to the site of disease<sup>40-45</sup>.

## 1.6 2D vs. 3D Cell Cultures

There are some limitations in the pre-clinical cancer models used in cancer research studies. Two-dimensional cell culture affords simplicity and low cost. Still, it has severe limitations because it is generally unable to fully mimic the tumor microenvironment by losing biological, chemical, and mechanical cues. In two-dimensional (2D) culture systems, cells are grown as monolayers on flat solid surfaces, lacking cell-cell and cell-matrix interactions which are present in native tumors. In addition, cells in their natural environment assume very different morphologies and gene expression compared to 2D cultured cells<sup>46</sup>.

In contrast, three-dimensional (3D) culture systems offer the unique opportunity to culture cancer cells alone or with various cell types in a spatially relevant manner, encouraging cell-cell and cell-matrix interactions that closely mimic the native environment of tumors<sup>47</sup>. Cancer cells grown in 3D culture systems have distinct phenotypes of adhesion, growth, migration, and invasion, as well as profiles of gene and protein expression. These interactions cause the 3D-cultured cells to acquire morphological and cellular characteristics relevant to *in vivo* tumors. Thus, 3D cell cultures have morphological and physiological features closer to the tumor structure compared to 2D cell cultures<sup>48</sup>.

In recent years, 3D artificial matrices have been used as an alternative model system to close the gap between 2D cell culture and complex animal systems<sup>49</sup>. In addition, the way cancer cells present their receptors and respond to anticancer drugs are different in the 2D and 3D culture conditions. For example, studies have shown that cancer cells are more resistant to cancer drugs in 3D cultures than in 2D cultures<sup>48</sup>.

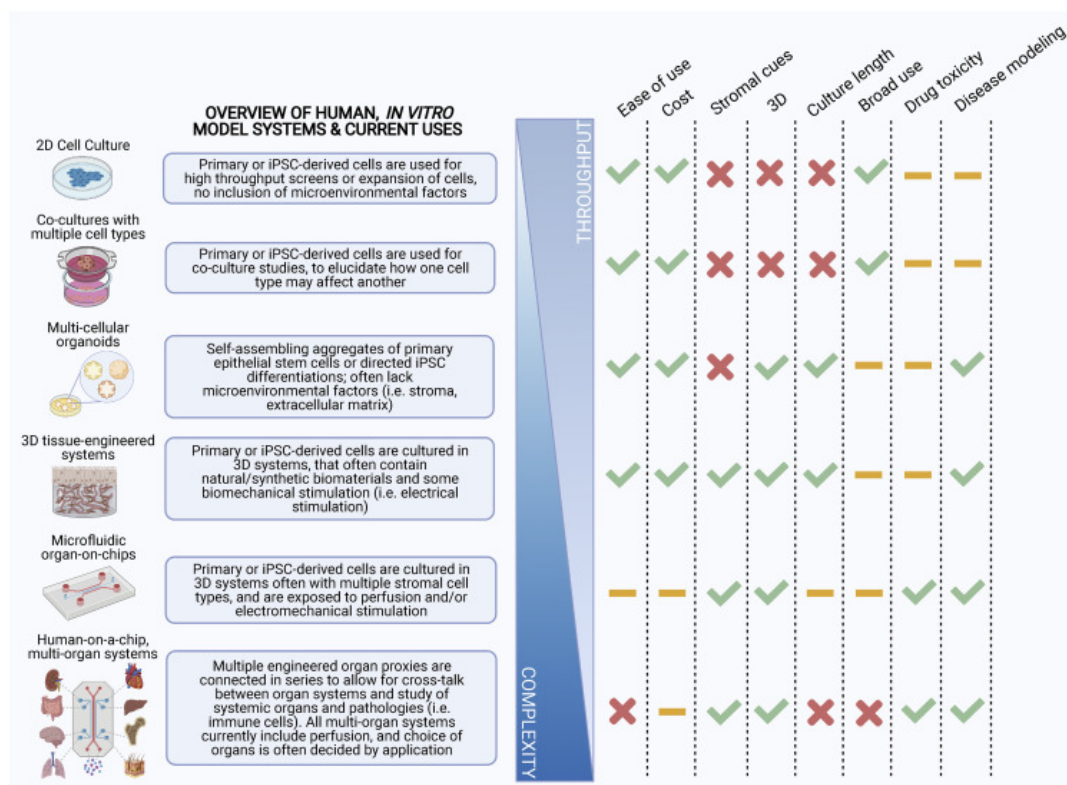


Figure 1.6. Representation of human, in vitro 2D, 3D, and organ-on-a-chip systems and current issues<sup>50</sup>.

The hanging drop method will produce cells in plates that do not contain scaffold and will be incubated under physiological conditions until actual 3D spheroids are formed. In this technique, droplets of the cell suspension are dispensed onto the underside of a Petri dish lid or spheroid culture array plates. The droplet hangs due to surface tension, and the cells in suspension spontaneously aggregate into spheroids under gravity<sup>47</sup>. In this method, cells are in direct contact with each other and with extracellular matrix components. This method will allow the production of tissue-like structures since cancer cells produced in the 3D matrix have different gene and protein expression profiles as well as phenotypes such as adhesion, growth, migration, and invasion. In addition, their response to receptor expressions and anticancer drugs will differ in 2D and 3D culture conditions<sup>51</sup>.

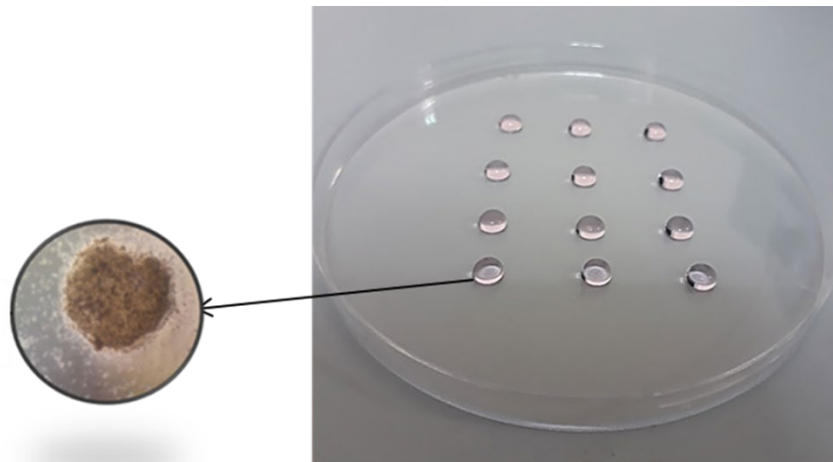


Figure 1.7. The hanging drop method.

### 1.7 Ex-vivo Cultures

Recently, studies on spheroids produced by 3D cell culture and organoid models have been increasing. It begins to bridge the gap between traditional 2D cell culture and tissue culture. However, spheroids have a limited ability to mimic the complex tissue architecture and cell composition of human tumors. From this point of view, they cannot represent the natural tumor tissue that is taken from patients in terms of different genetic makeup, tumor grade, or responsiveness to therapy<sup>9-31-52</sup>. This has triggered the search for alternative or complementary therapeutic strategies with traditional tissue culture methods. Ex-vivo cultures obtained from xenografts generated by tumor cells in immunodeficient mice constitute a structure much closer to the tumor microenvironment<sup>53</sup>. Ex-vivo cultures can supply suitable environments for experimental studies for the actual testing of therapeutics on real tissues from patients<sup>54</sup>. But, this method has some significant problems, such as the inability to maintain viability and metabolic activity over a sufficient number of days for different analytical purposes. Since they lack any functional vasculature ex-vivo primary tissues, they are prone to premature death and leave no time to test neither therapies nor obtain a reasonable output<sup>55</sup>. Solid tumors are characterized by hypoxic and necrotic areas resulting from the high metabolic activity of tumor

tissue and lack of oxygen supply due to insufficient vasculature. Hypoxic areas of solid tumors have an increased resistance to chemotherapy and radiation compared to better-oxygenated tumor tissue<sup>56</sup>. In addition, the metabolic waste content of tumor sites is generally higher than normal tissue's microenvironment<sup>57</sup>. Hypoxemia can be reduced by slicing the tissue into thin slices (250–500 $\mu$ m) of relatively large (~4mm) diameter, with the smaller dimensions facilitating the transport of nutrients and oxygen to the center<sup>32-8</sup>. Since the sections taken in this tissue culture method are very thin, there is no oxygen and nutrient deficiency, and the viability of the cells continues in the culture medium for a week. In addition, recently, researchers have successfully extended the culture time of tissues or cell aggregates in their microfabrication device or biochips by several weeks<sup>54</sup>.

## **1.8 Objective of the Thesis:**

In recent years, studies on controlled and targetable drug systems have been intensified in order to increase the effectiveness of the drugs used in cancer treatment on cancer cells and prevent damage to healthy cells. Magnetic nanoparticles with very small sizes are important in directing the desired amount of drugs to the desired region and gain importance among the new generation targeted chemotherapy systems. However, there are some limitations in the preclinical cancer models used in this research.

Cell culture models are known to be lacking in the tumor microenvironment, which has a significant effect on tumor biology and therapeutic response. On the other hand, in vivo studies are quite laborious and costly. In recent years, 3D artificial matrices have been used to close the gap between 2D cell culture and complex animal systems. However, 3D culture also has a limited ability to mimic the complex tissue architecture and cell composition of human tumors. Microfluidic biochips with combined micro-dissected tissues (ex-vivo culture) are a new culture method and suitable system to overcome 2D and 3D culture methods problems. This new strategy is an ideal model for tissue viability testing, new drugs, and drug

life cycle from preclinical to patient use in terms of the most suitable treatment regimen selection.

Based on the above discussions, the objectives of the thesis study can be listed as follows:

1. Design, construction, and characterization of a microfluidic biochip. This new biochip is an ideal model for tissue viability testing, new drugs, and drug life cycle from preclinical to patient use in terms of selecting the most suitable treatment regimen.
2. A new method for conjugating Palbociclib onto magnetic nanoparticles coated with PAMAM dendrimer. To the best of our knowledge, there is few reports have been published for Palbociclib being loaded on a drug delivery system.
3. Comparing the efficacy of drug and drug conjugated nanoparticles in 2D, 3D, and ex-vivo cultures. There is no knowledge of the literature comparing the efficacy of drug conjugated nanoparticles in 2D, 3D, and ex-vivo cultures. Palbociclib is a new drug and has not previously studied the effect on the cells by binding to magnetic PAMAM nanoparticles.

For these reasons, this study has an original value. It can provide the most appropriate condition for experimental studies for empirically testing therapeutics in the growing field of personalized medicine.





## CHAPTER 2

### **DEVELOPMENT OF A MICROFLUIDIC PLATFORM TO MAINTAIN VIABILITY OF MICRO-DISSECTED TUMOR SLICES IN CULTURE**

One of the issues limiting the development of personalized medicine is the absence of realistic models that reflect the nature and complexity of tumor tissues. We described a new tissue culture approach that combines a microfluidic chip with the micro-dissected breast cancer tumor. 'Tumor-on-a-chip' devices are suitable for precision medicine since the viability of tissue samples is maintained during the culture period by continuously feeding fresh media and eliminating metabolic wastes from the tissue. However, the mass transport of oxygen, which arguably is the most critical nutrient, is rarely assessed. According to our results, transportation of oxygen provides satisfactory *in vivo* oxygenation within the system. A high level of dissolved oxygen, around 98-100% for every 24 hours, was measurable in the outlet medium. The microfluidic chip system developed within the scope of this study allows living and testing tumor tissues under laboratory conditions. In this study, tumors were generated in CD-1 mice using MDA-MB-231 and SKBR-3 cell lines. Micro-dissected tumor tissues were cultured both in the newly developed microfluidic chip system and in conventional 24-well culture plates. Two systems were compared for two different types of tumors. The confocal microscopy analyses, LDH release, and glucose consumption values showed that the tissues in the microfluidic system remained more viable with respect to the conventional well plate culturing method, up to 96 hours. The new culturing technique described here may be superior to conventional culturing techniques for developing new treatment strategies, such as testing chemotherapeutics on tumor samples from individual patients.



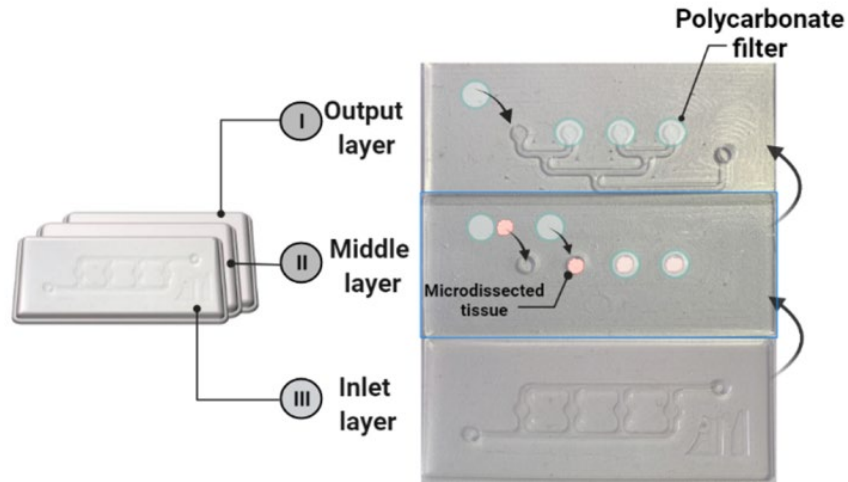


Figure 2.2. Microfluidic chip composition. I. Bottom layer (outlet layer), II. Middle layer (Tissue chamber), III. Upper layer (Inlet layer).

Figure 2.3 compares the flow profile in one tissue chamber with filters to that without filters simulated by using COMSOL Multiphysics. PCTE filters and the tumor slice were modeled as porous media with Darcian flow. Through simulations, it was demonstrated that the use of polycarbonate filters allows a uniform flow of medium through the dissected tumor. The streamlines in the chamber are homogeneously distributed (Figure 2.3.d), in contrast to those in the case without the filter (Figure 2.3.c).

Based on the manufacturer's data, the porosity and the permeability of the filter were set as 0.05 and  $4 \times 10^{-14} \text{ m}^2$ . The PCTE filters have nominal  $8 \text{ }\mu\text{m}$  diameter pores with  $1 \times 10^5 \text{ cm}^{-2}$  density, and also the filters are track-etched, yielding almost cylindrical through holes across the thickness of the filter, concluding the porosity is:

$$\text{Equation 2.1. } c_{filter} = \frac{\pi(8 \times 10^{-4})^2}{4} (1 \times 10^5) \approx 0.05$$

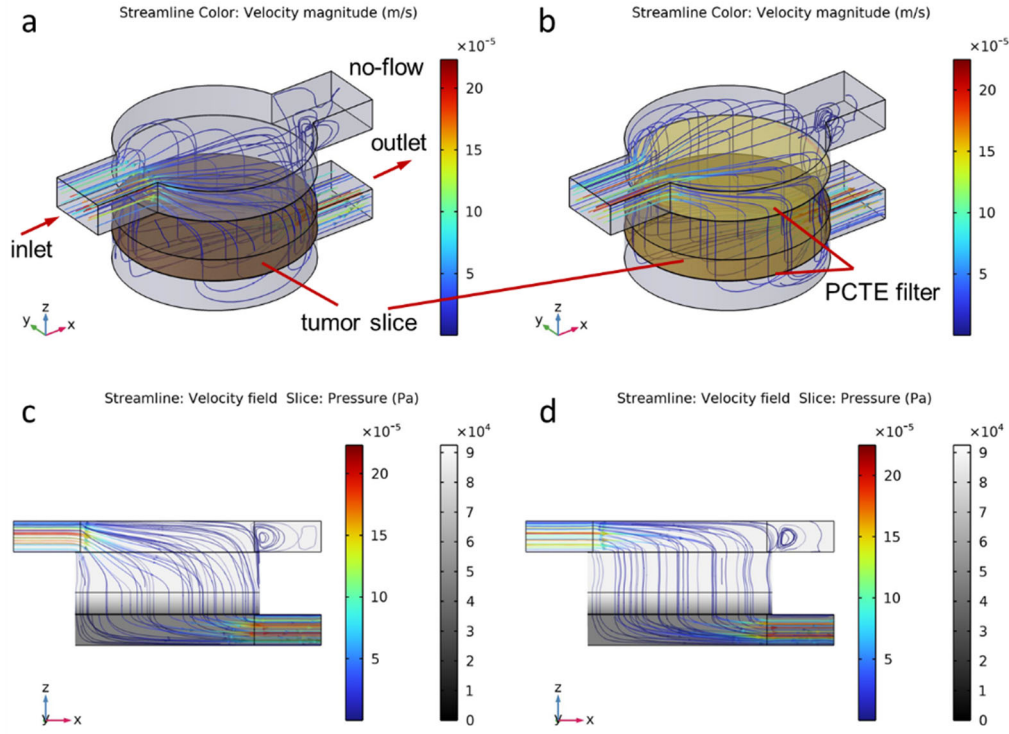


Figure 2.3. Flow profiles were obtained using COMSOL Multiphysics. Laminar flow physics was utilized with a constant flow rate of 5ml/day at the inlet and zero pressure at the outlet. The PCTE filter and the tumor slice were modeled as porous media with Darcian flow. (a) Unfiltered chamber geometry, (b) Filtered chamber geometry, (c) Flow profile observed in the chamber in the unfiltered condition, and (d) Flow profile observed in the chamber in the filtered condition.

Based on the flow rate across the filter under known pressure stated in the manufacturer data again, we estimated the flow resistance of the filter is  $0.58 \times 10^{11}$  Pa.s/m<sup>3</sup>. Given this information, we simulated flow across a single PCTE filter under unit pressure and tried to find out the permeability of the filter in Darcy's law that would result in the same flow resistance. Accordingly, we found that the permeability of the filter is:

$$\text{Equation 2.2. } \kappa_{filter} = 4 \times 10^{-14} \text{m}^2.$$

Similarly, the porosity and the permeability of the tumor slice were set as  $c_{tumor} = 0.82$  and  $\kappa_{tumor} = 3.10 \times 10^{-17} \text{m}^2$  by referring to Ref. <sup>58</sup>.

Figure 2.4 shows the solution domain and the boundary conditions. Apart from the porous polycarbonate filters and the tumor slice, where Darcy's law applies, the flow was modeled as a laminar flow.

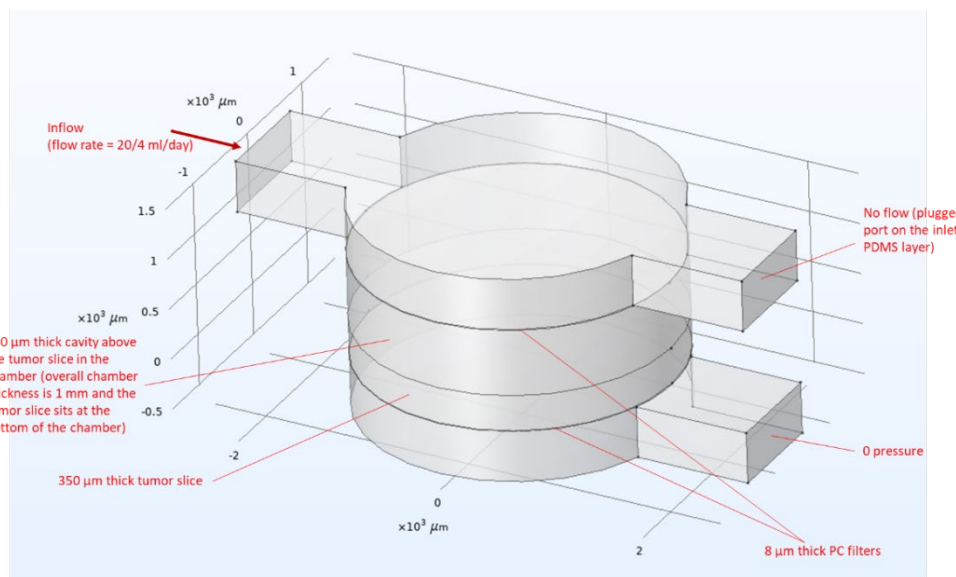


Figure 2.4. Description of the domains and the boundary conditions. The tumor slice and the PC filters were modeled as porous media with Darcian flow.

During the operation, the flow rate across the microfluidic chip was measured as 20 ml/day. Assuming that the flow rates across 4 tissue chambers are equal to each other, the 5 ml/day flow rate was set at the inlet in the simulation model. The outlet was set to zero pressure. Navier-Stokes equations were solved assuming laminar flow with the stated boundary conditions.

The microfluidic circuit can be modeled by referring to the electrical circuit analogy, as illustrated in the figure below. Although the microfluidic network on the inlet layer is unbalanced, the flow across the tissue chambers is determined by the resistances of the branches. Therefore, the flow resistance along each branch is expected to be dominated by the resistance of the polycarbonate filters and the 350 μm thick tissue slice. To prove this, the resistances of the microfluidic channel

segments (as illustrated in figure 2.5) were calculated, and the resistance of the tissue chamber with the membranes was estimated.

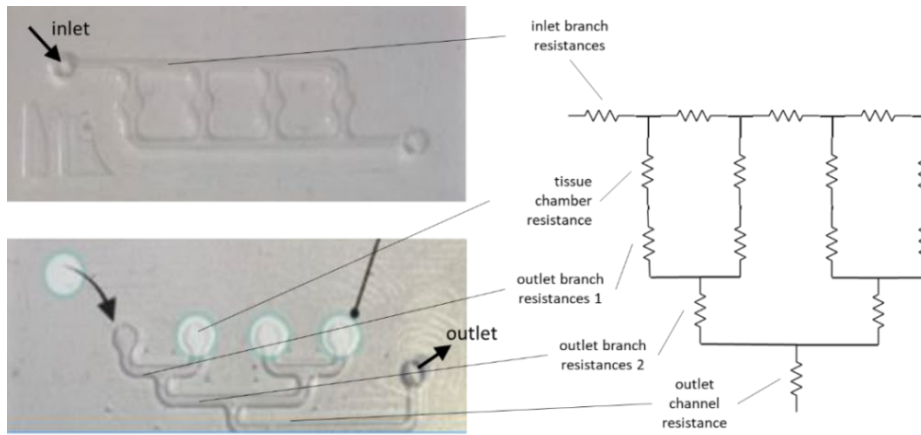


Figure 2.5. Electrical circuit analogy of the microfluidic network

Resistances of the microchannel segments were calculated by referring to the below equation for rectangular channels:

$$\text{Equation 2.3. } R = \frac{12\mu L}{h^3 w} (1 - 0.630h/w)^{-1}$$

Where  $\mu$  is the fluid viscosity,  $L$  is the channel length,  $h$  is the channel height, and  $w$  is the channel width. Assuming aqueous solution with 1 mPa.s viscosity, the flow resistance of each segment was calculated as below (The height and the width of the channels are 0.5 mm and 1 mm, respectively. The lengths of the microchannel segments were extracted from CAD data.)

Resistance of inlet branch:  $8.41 \times 10^{11}$  Pa.s/m<sup>3</sup>

Resistance of outlet branch 1:  $2.79 \times 10^{11}$  Pa.s/m<sup>3</sup>

Resistance of outlet branch 2:  $9.86 \times 10^{11}$  Pa.s/m<sup>3</sup>

Resistance of outlet channel:  $3.08 \times 10^{12}$  Pa.s/m<sup>3</sup>

The simulations resulted in the hydrodynamic resistance of the tissue chamber with the filters, and the tumor slice was in the order of  $10^{15}$  Pa.s/m<sup>3</sup>. This resistance was significantly greater than the hydraulic resistances of the channels, which were

calculated to be in the order of  $10^{11}$  Pa.s/m<sup>3</sup>. The observation that the hydraulic resistance of the microfluidic network was dominated by the chamber resistances justified the assumption of the equality of the flow rates across the tissue chambers.

### 2.1.2 Mold and PDMS Device Fabrication

The top PDMS layer was fabricated as a thin layer (2 mm) to allow oxygen and carbon dioxide regulation within the tissue incubation chamber during testing. In order to facilitate permeation, air inlets were drilled on the top PMMA plate. The layers were fabricated by the standard PDMS molding process. The molds were fabricated as pockets on brass plates by milling (Proxxon FF500 / BL-CNC Milling Machine) (Mechanical Engineering Department, METU), such that the thickness of the layers was directly controlled by the depth of the pockets (Figure 2.6).

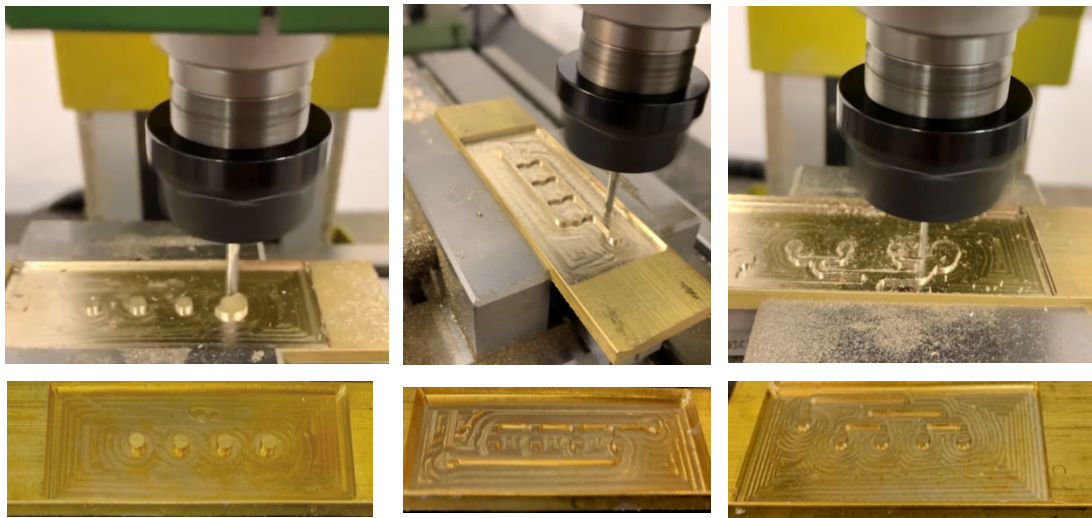


Figure 2.6. Brass molds Fabrication

PDMS monomer mixture was poured on these molds with a curing agent at the rate of 1:10, and it was kept in an oven at 80°C for two hours to ensure curing. Then, the cured PDMS was detached from the brass mold, and the inlet and outlet were opened with the biopsy punch (Figure 2.7).

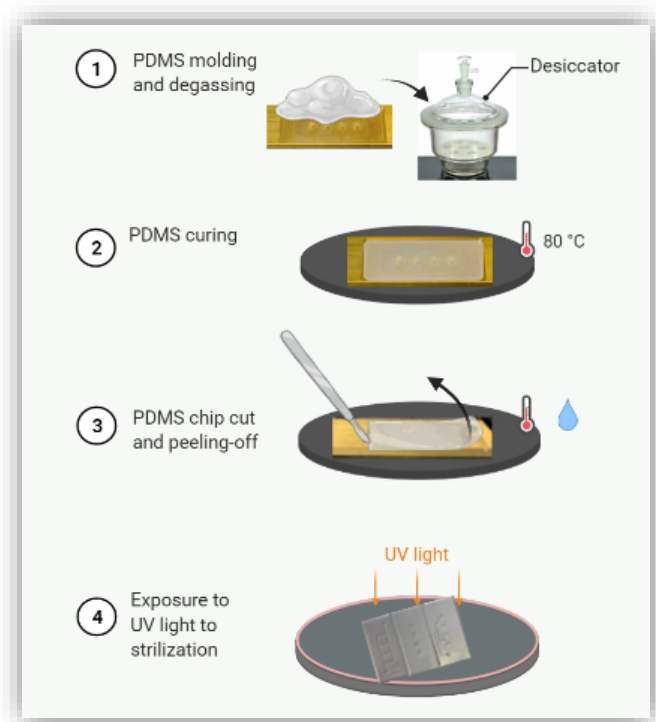


Figure 2.7. Schematic view of PDMS molding method

The layers were sandwiched between two polymethylmethacrylate (PMMA) plates by using binder clips (Figure 2.8). This non-permanent assembly scheme allows the tumor slices to be removed from the chip for further investigation during the experiments.

During the operation, the medium is directed to chambers via the inlet channel posed in the top PDMS layer. The liquid is perfused through the tissue in the chamber and then collected via the exit channel at the bottom PDMS layer. However, since multiple chambers are fed in parallel, it is possible to have bubbles trapped in the inlet channel at the beginning of the operation.



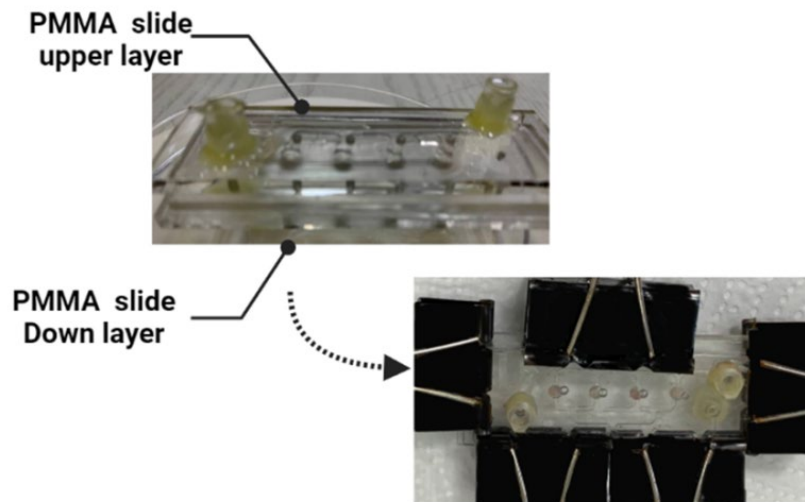


Figure 2.8. Photograph of a PDMS chip sandwiched by PMMA slide layers by using binder clips.

In order to prevent air bubbling problems, PDMS layers were pre-treated with 100% ethanol and, after drying, sterilized under UV light. However, bubbles were observed, especially during the priming of the channels. To capture these air bubbles, a dummy outlet was located at the end of the inlet channel. The bubbles in the inlet channel were captured through this dummy outlet by using a syringe. Once the bubbles were completely removed, this dummy outlet was plugged in and kept closed during the operation. For daily examinations, the media was collected from the outlet on the bottom PDMS layer and used for biochemical analysis.

The amount of dissolved oxygen (DO) and pH were measured from the outlet medium of the non-tissue chip to check gas diffusion through the PDMS layers. The DO was measured by micro-DO- electrode (YSI, 556MPS), and pH was measured by pH-meter (WTW InoLab 720 pH/Cond Meter) from 20ml outlet medium after 24h. In addition, the pH of the outlet medium from the micro-dissected tissue cultured chip was measured during culture time at every 24h.

## **2.2 Ex-vivo Breast Cancer Models**

Female CD-1 athymic (without thymus gland) nude mice (~25 g) were obtained from Kobay A.S. (Ankara, Turkey). The mice were maintained under 12h light/dark cycle in steel micro-isolator cages in 22±2°C temperature and 45-55 percent humidity-controlled room with free access to autoclaved water and food (SDS/RM3, DU, IRR) and handled only under sterile conditions. The use of animals for these experiments was approved by the Animal Ethics Committee of KOBAY DHL A.S. (local ethical comity- 02.01.2017-#208).

### **2.2.1 Preparation and Injection of Cells for In-vivo Culture**

During the exponential phase, cells were collected from the culturing flask and transferred to a 15mL tube. The cells were spun down at 1,500 rpm for 5 minutes. Then the supernatant media were aspirated, and cells were washed with sterile 1X PBS and spin-down. After PBS aspiration, the cell pellets were resuspended in 5ml PBS, and cell viability and cell number were checked at this step. The optimum number of cells between the range of ( $5 \times 10^6$ - $7 \times 10^6$ ) were mixed with either 100µL PBS or 50µL PBS+50µL matrigel according to cell type. The cells were kept on ice until injection. Before each injection, the cells were mixed well. Injections were done subcutaneously to the mice, and the syringe was kept inside for at least 20s to allow the gelling of matrigel at the injection site (Figure 2.9).

### **2.2.2 Preparation of the Tumors and Micro-dissected Tumor Slices**

Tumors were generated in mice by using MDA-MB-231 and SKBR-3 cell lines. Mice were monitored for the development of primary xenograft tumors and weighted at least once a week. Tumors were measured weekly with a Vernier caliper, and once they reached roughly 1×1cm in size, they were removed, and the animal was sacrificed (Figure 2.9).

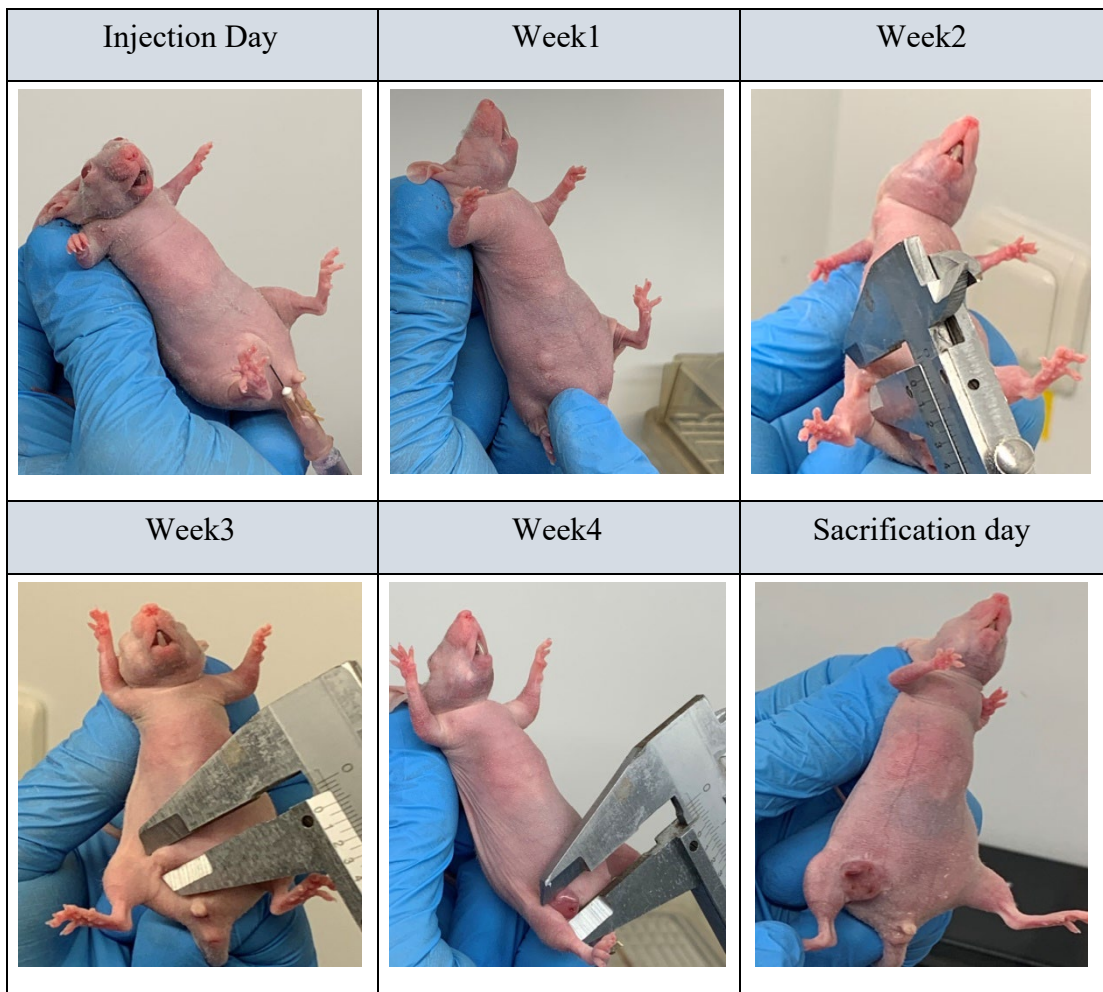


Figure 2.9. Developing breast cancer model in Cd-1 nude mice

All of the surgical procedures began after placing the animals under general anesthesia. Following a subcutaneous incision, the tumor was exposed, measured, and placed in ice-cold (1–2°C) Hank's medium (HBSS, #311-516-CL, Wisent Inc., Saint-Bruno-de-Montarville, Canada) supplemented with 1% Pen-strep (HyColone-Thermo Scientific). For producing the micro-dissected tumor slices, the tumor tissue was embedded into 4% low melting point agarose (SIGMA (A-9539), USA).

The agarose was solidified on ice for at least 10 minutes, thereby creating a supporting structure around the embedded tissue. Next, a traditional Vibratome (The Campden Instrument LTD, 1990) was used to obtain 350µm thick slices from

the tumor tissue inside a 10°C bath containing Hank's Buffered Saline Solution supplemented with 1% Pen-Strep. The produced slices were kept in the same solution and finally further cut into disk-like pieces using a 3mm diameter tissue punch inside Hank's buffer. The final product was a cylindrical micro-dissected tumor tissue of approximately 350µm in height and 3 mm in diameter and had a wet weight of about 3.4µg (Figure 2.10).

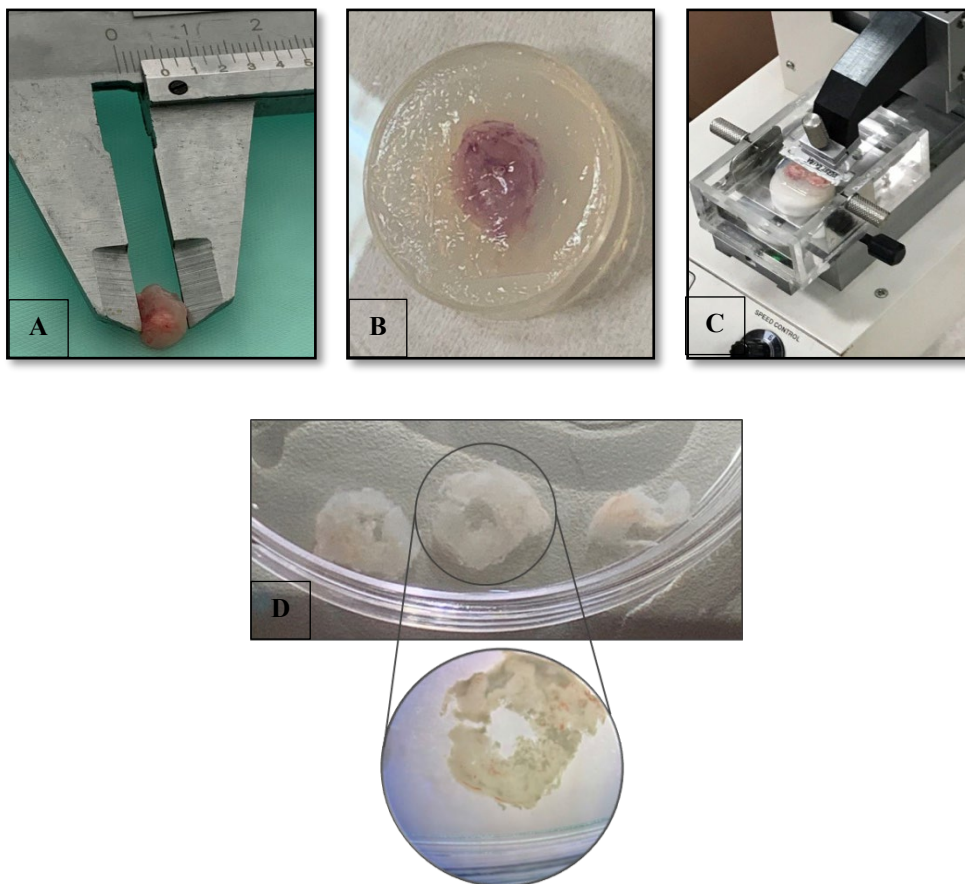


Figure 2.10. (A) Tumor size measurements with Vernier caliper, (B) Embedding of tumor in the low melting agarose before slicing, (C) Slicing of a tumor by Vibratome, and (D) Tumor slice (~350µm).

### 2.2.3 Culture of Micro-dissected Tissues

Immediately after slicing, the tissue slices were incubated by two different methods. The microfluidic chip and 24-well plates with permeable polycarbonate membrane polystyrene transwell plate (Corning, 6.5mm diameter, 8.0  $\mu\text{m}$  pore size) were used. Every week one tumor was removed from one animal and incubated in the same conditions for microfluidic chip and well-plate experiments. The representative scheme of the ex-vivo culture system is given in Figure 2.11.

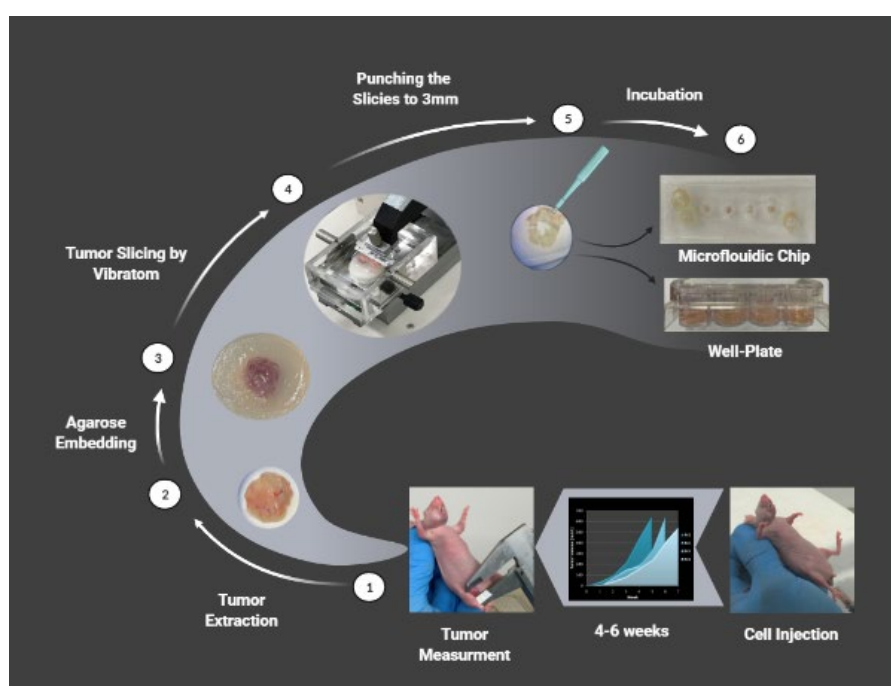


Figure 2.11. Representative scheme of ex-vivo culture arrangement. Preparation of the tumors and microdissection of the tumor for culturing at two systems.

#### 2.2.3.1 Microfluidic Chip

Four micro-dissected tissues were placed in four chambers in the middle layer of the chip, which had been attached by inlet and outlet layers. PDMS layers were fixed by two PMMA layers and placed in an incubator at 37°C for 96 hours (Figure 2.12 A, B). Sterile glass containers (100 ml) containing medium were closed with 2-ports microfluidic reservoir caps. Each container was connected to one chip so



that many microfluidic chips could be operated in parallel. The containers were pressurized through the tubing and a manifold connected to a microfluidic autonomous pressure pump (Elvesys Elveflow AF1, Paris, France) Figure (2.12 C, D).

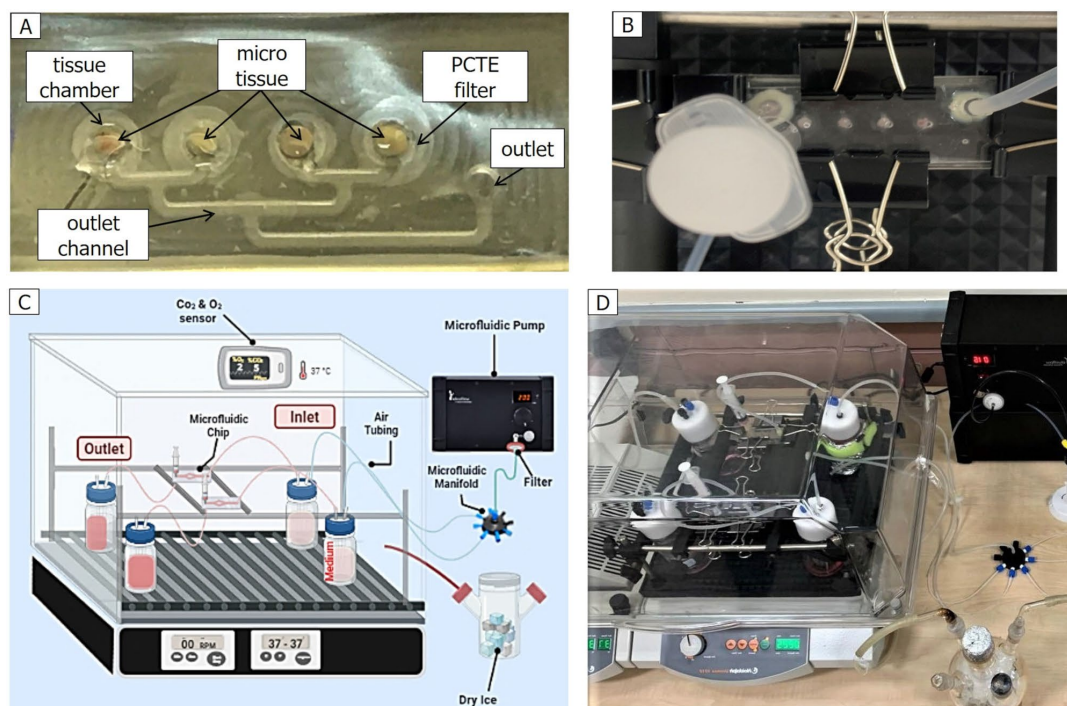


Figure 2.12. Overview of incubators and placement of chips inside incubators. (A, B) Placement of tumor sections in a microfluidic chip. (C) Schematic view of a system. (D) Real view of microfluidic chips incubation systems.

The tumor chip was connected to a container containing the appropriate media and attached to a calibrated pressure pump within an in-house incubator with an installed CO<sub>2</sub> and O<sub>2</sub> sensor. The pressure pump was set to ~19mbar, so the medium was infused continuously into the chip at a rate of 14 μL / min for 96 hours. The dummy outlet on the top PDMS layer was plugged with a 5ml syringe. This outlet was used to capture the air bubbles present in the inlet flow channel. Fresh media was provided to the tissue samples for 96 hours uninterruptedly, and the media coming out of the system was collected daily in 100 ml sterile glass

containers with special 4-port lids. The flow rate was monitored by measuring the volume of the medium collected in the glass container after one day of operation by using the graduations on the container. Infusions were stopped after 96 hours, and micro-dissected tumor samples were removed from the device for post-chip analyses.

### 2.2.3.2 Well Plates

Tissue slices were incubated in a 24-well plate with a transwell permeable plate in 1ml RPMI 1460 medium and incubated at 37°C incubators for 96h. The medium was removed for the metabolic activity test and replaced by a fresh medium every 24h (Figure 2.13).

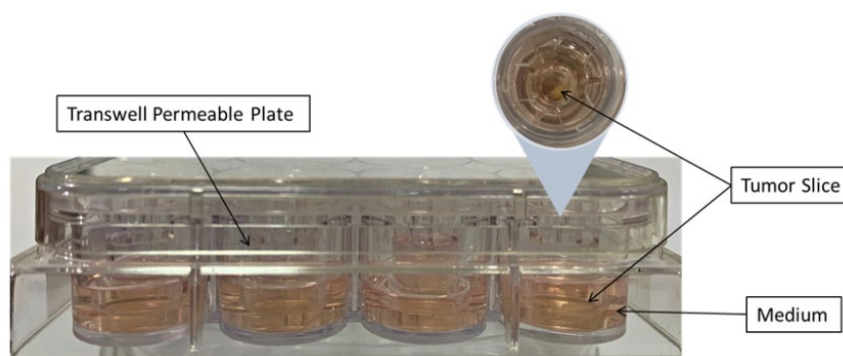


Figure 2.13. Well-plate culture system. Tumor slice cultured in the upper chamber of the transwell permeable plate.

### 2.2.3.3 Hematoxylin-Eosin Staining

H&E staining of the tumors obtained from MDA-MB-231 and SKBR-3 cells grown in CD1 mice was performed. In addition, pathological analyses were done on the first day of tumor removal in order to prove the tumor formation.

#### **2.2.3.4 Tissue Viability Assessment by Confocal Microscopy**

As a way to compare the viabilities of micro-dissected MDA-MB-231 and SKBR-3 tumor slices in the microfluidic chip and well-plate culture systems, micro-dissected tumor slices from the same tumor were stained on the first and fourth day of cultivation. Fluorescein diacetate (FDA) (Sigma-Aldrich, USA) (10 $\mu$ l) and Propidium Iodide (PI) (Sigma-Aldrich, USA) (5 $\mu$ l) were dissolved in 5ml PBS. On the first day, slices were incubated at 24 well-plates with 1ml /well PBS containing FDA and PI and rotated for 1 hour. After the incubation time, the micro-dissected tissues were washed with PBS, and images were taken. Layer-by-layer photos of each micro-dissected tumor were captured by confocal microscopy on the first day immediately after segmentation and after 96h from two ex vivo cultivated methods. Two replicate samples were used to capture 10 sequential images using a 20x lens to test each cultivation method. The contrast of images was improved by using deconvolution software with Huygens essential software (SVI, Hilversum, the Netherlands). Totally six different images were taken from each group (two replicated slices and three shots from different positions of a slice). The intensity sum (px intensity) of fluorescence was calculated by using the MIPAR software<sup>59</sup>.

#### **2.2.3.5 Daily Analysis of the Supernatant**

The metabolic activity was detected daily from the outlet medium samples of the microfluidic device and well-plate system by using an automated biochemistry autoanalyzer (Beckman Coulter DXC800, USA). A supernatant volume of 1 mL/day was used to assess the LDH and Glucose content of the output media from slices in both systems.



## 2.3 Results & Discussion

Tumor slices are cultured in a newly designed microfluidic chip system and compared to traditional culture methods. One of the microfluidic chip's primary purposes is to keep the tumor fragments alive in culture systems for anticancer drug testing on real tumor tissues from patients in the future. The continuous supply of fresh media to the tissue samples and removing metabolic wastes maintain viability during the culture period. Many conventional culture methods implicate various drawbacks, including maintaining viability over a sufficient number of days for various analytical purposes. Furthermore, without adequate feed and oxygen, tumor slices die prematurely, leaving little or no time to test therapeutics for guiding the selection of an optimal treatment regimen.

### 2.3.1 Tumor Tissue Analyses by Hematoxylin-Eosin Staining

Tumors derived from MDA-MB-231 and SKBR-3 breast cancer cell lines in CD1 mice were visualized on a stereomicroscope for the identification of tumor size, morphology, and angiogenesis (Figure 2.14A). Then, further pathological analyses were done by the hematoxylin-eosin staining method. Hematoxylin-eosin staining of tumor sections derived from MDA-MB-231 cells indicated that cells preferentially grew in ducts from ductal papillae, which is the main characteristic of MDA-MB-231 originated tumors (Figure 2.14B).

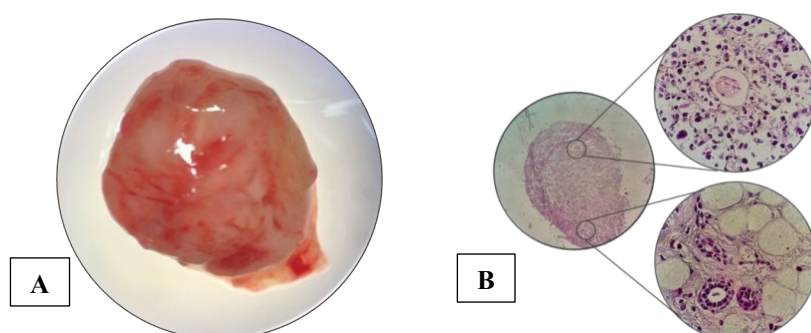


Figure 2.14. A) MDA-MB-231 tumor image under a stereo microscope, B) H&E images of MDA-MB-231 tumor slice sections on the first day.

### 2.3.2 Assessment of Cell Viability of Micro-dissected Tissue Cultures

Following segmentation of the MDA-MB-231 and SKBR-3 tumor tissue, fluorescein diacetate (FDA) and propidium iodide (PI) dyes were used to assess the viability of micro-dissected tissues before and after four days of cultivation. Various methods can be used to measure the survival of cells within tissue slices. Confocal laser scanning microscopy eases access for living cell imaging in 3D tissue. By using confocal microscopy, it is possible to obtain stratified images through the depth of the 3D tissue sample, allowing for information on each focal plane to be obtained. Computer-controlled confocal microscopy creates digital images which are compliant with image and data processing<sup>60</sup>. FDA has been used for the viability assessment of a wide variety of cells and tissue types<sup>61-62</sup>. As the FDA assay does not have any significant toxicity, making this assay suitable for cell and tissue culture analysis. FDA is not a fluorescent molecule, and by the opportunity of bipolar side chains, it penetrates into living cells. FDA remains colorless until esterases convert it to fluorescein inside the metabolically active cells. Under the light of microscopy, the intensity of fluorescence was seen; it gave the proportion of live cells in the layers of tissue<sup>62-63</sup>.

The maximum intensity projection (MIP) and the fluorescence intensity histogram for the green (live) and red (dead) were subtracted from the 3D image (Figure 2.15, B, D, F). The MIP visualized the volume of live and dead cells, and the intensity histogram of MIP demonstrated fluorescent intensity to the number of voxels in each 3D image. MIP images with low green intensity and high red intensity were seen in an image from well-plate system slices (Figure 2.15, F). However, imaging from the microfluidic slice showed that red fluorescence was strongly diminished, whereas green cells remained brightly fluorescent (Figure 2.15, D).

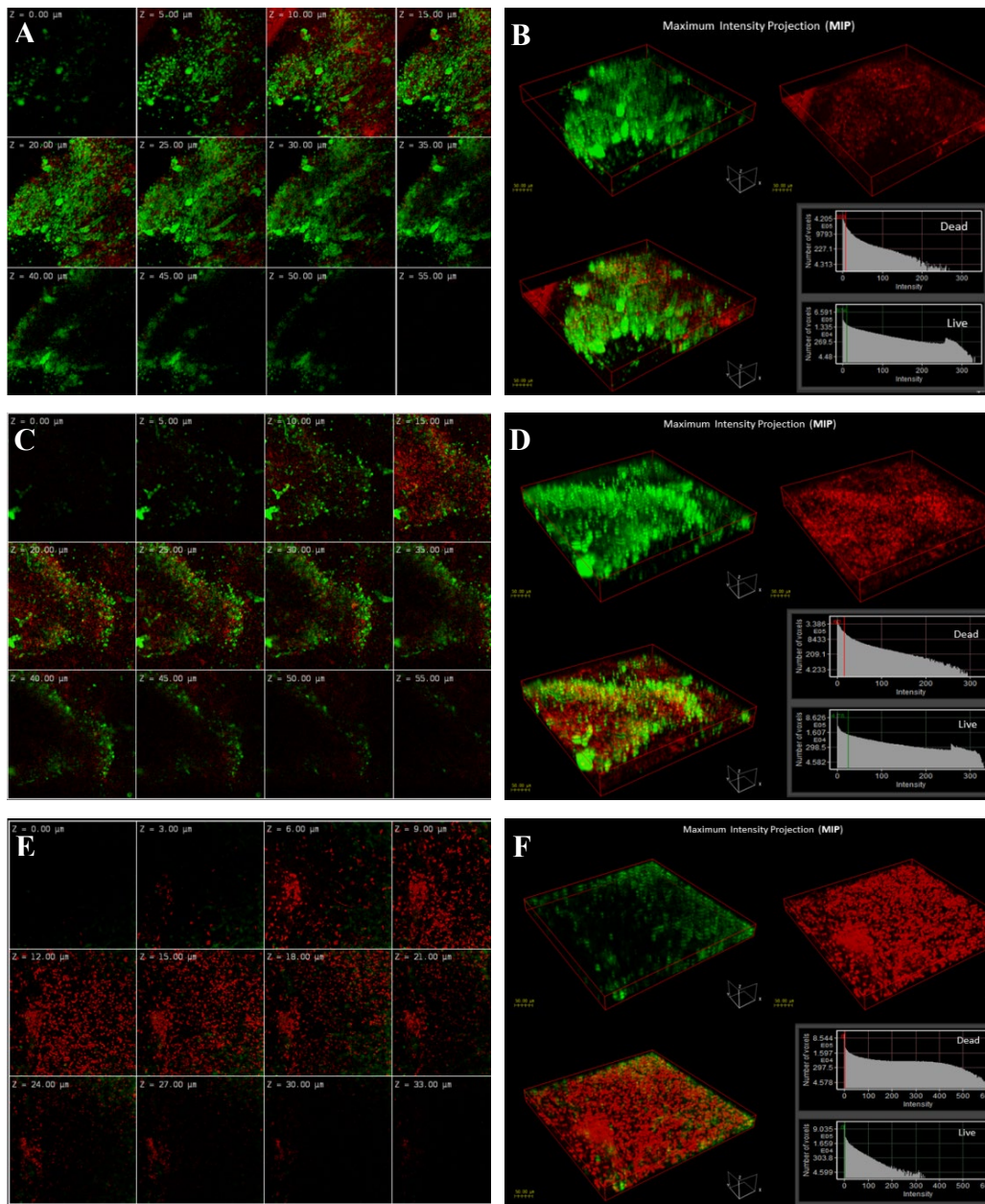


Figure 2.15. Confocal imaging and maximum intensity projection of MDA-MB-231 micro-dissected tissues. Layer by layer images indicated the differences between the amount of live & dead cells in micro-dissected tissues on the first day immediately after the operation (A, B) and after four days of cultivation at the microfluidic chip (C, D) and well-plate system (E, F). Alive and dead maximum intensity projections from a representative MDA-MB-231 slice of confocal image stacks from the first day and after 96h from the microfluidic and well-plate system (by Huygens Essential software) (B, D, F).

Figure 2.16 shows the observed difference between average red and green fluorescence intensity from six images. The sum intensity for each layer of images is calculated separately. The loss of red fluorescence intensity was more pronounced in whole tumor (MDA-MB-231 and SKBR-3) images from the microfluidic chip. In comparison, green fluorescence remained bright, even more than the first-day green intensity.

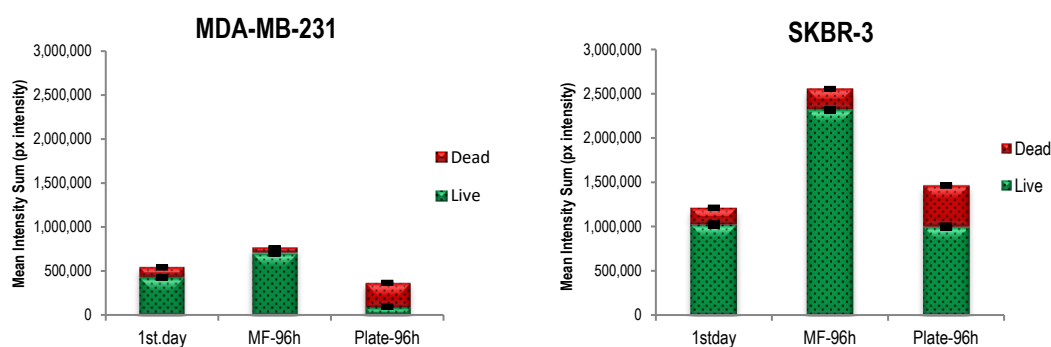


Figure 2.16. The mean sum intensities of MDA-MB-231 (A) and SKBR-3 (B) tumors from three different positions of two slices of micro-dissected tissues (Slice number: n=2, image number: n=6). The sum intensity for live and dead images is calculated by the MIPAR program for each layer-by-layer image. The average of sum intensities shows the difference between the first and fourth days of different cultivation methods.

### 2.3.3 Mass Transfer Analysis of Oxygen and Carbon Dioxide

The addition of dry ice to the incubator periodically provides the required amount of CO<sub>2</sub>, as measured by a CO<sub>2</sub> sensor. By virtue of PDMS gas permeability, it allows CO<sub>2</sub> and oxygen to diffuse into the chamber from the ambient air. Therefore, controlling carbon dioxide gas concentration in a surrounding area could provide the optimal pH for tissue viability.

As a first step, during the setting up, the stability of pH values was measured every day in a non-tissue installed microfluidic chip for 96 hours. The pH value was measured in the supernatant medium of the chip and compared with CO<sub>2</sub> concentration in the incubator (ppm/min) to determine how much dry ice was needed to be added to the incubator during the day. A small butterfly valve

controlled the amount of exiting CO<sub>2</sub> from the reservoir of the dry ice container. By this method, the microfluidic chip outlet medium pH was measured as  $\sim 7.4 \pm 0.05$  after 24h, indicating equilibrium with 5% CO<sub>2</sub> at 37°C<sup>64</sup>. Furthermore, the pH value of the tissue-containing device perfusion experiments was also constant and suitable for tissue viability for four days. The pH value of the outlet medium of the micro-device was measured every 24h, and the results were the same as a non-tissue-containing device, between  $7.4-7.6 \pm 0.05$ . For the well-plate system, the media of tissue was changed every day; the pH value of media was around  $7.6-7.8 \pm 0.05$ . In addition, we used a medium (RPMI1640) containing phenol red, which is a pH indicator. No color change, and as a consequence, no pH change was observed in the outlet medium of tissue containing chips during all experiments, which indicated that the CO<sub>2</sub> level was sufficient over 24h. However, a significant color change could be seen in the medium of control (non-tissue well) and tissue-contained wells during well-plate culture.

The concentration of dissolved oxygen (DO) in the outlet medium of the non-tissue-cultured device was also very high and stable, around 98-100% (9.38-9.43 mg/L) on supernatant every 24h. The concentration of DO in the outlet medium in the presence of tissue was also checked at the end of 96h and found as 100% (9.43 mg/L). The O<sub>2</sub> permeability of PDMS and the oxygen concentration in the inlet medium are enough since the medium is initially saturated with oxygen during the pumping process. Therefore, a constant flow of oxygenated medium through the chambers offers the appropriate amount of oxygen for the micro-tissues during culture time in the microfluidic system<sup>64-65</sup>. Misra et al. (2019) showed that 350  $\mu\text{m}$  thick precision-cut slices represent the maximum width for the diffusion of oxygen and substrates into the deepest cell layers of the tumor slice. Cultured tissue slices were metabolically active for 96h in their well-plate culture system. Also, it is indicated that the oxygen tension did not affect the proliferative activity of the tumor<sup>65</sup>. Monitoring O<sub>2</sub> levels are crucial for assessing tissue cell viability and metabolic activity in microfluidic systems. As a result of recent advances in microfluidics, O<sub>2</sub> sensing has become an essential feature for organ-on-a-chip

devices for various biomedical applications. Therefore, various optical and electrochemical on-chip O<sub>2</sub> sensors were integrated with the organ-on-a-chip devices<sup>14</sup>. The low concentration of O<sub>2</sub> inside many microfluidic chips requires precise and selective quantification for confined settings. Based on COMSOL simulations, the suitability of different tumor slices for oxygen mass transport within microfluidic devices was evaluated, leading to the development of an optimized design for achieving defined in vivo oxygenation within an organ-on-a-chip system<sup>11</sup>.

### **2.3.4 Micro-dissected Tumor Slice Viability Analysis**

Martin G. Christensen et al. show the oxygen transport efficiencies in a precision-cut liver slice fabricated device by LDH assay<sup>11</sup>. The viability of the tumor tissue samples was evaluated by lactate dehydrogenase (LDH) release and glucose consumption analysis. LDH is a cytoplasmic enzyme constitutively expressed in most mammalian cells. Determining the amount of LDH released into the medium is widely used to assess plasma membrane integrity. Excessive release of LDH enzyme into the medium indicates that the cells are dead, while the consumption of glucose from the medium shows that the cells are alive for determining the micro slice viability in the microfluidic chip and well-plate incubation systems, leakage of LDH and glucose consumption amount were measured every 24 hours for 96 hours. In each experiment, the tumor of the same mouse was incubated in the two incubation systems.

#### **2.3.4.1 Lactate dehydrogenase Analysis**

In order to confirm that the tumor micro-slices were viable in the micro-chamber, the viability was examined using LDH release over a 96h period and compared to traditional well-plate systems. All experiments were performed with four tumor slices per mouse for five mice for SKBR-3 and four mice for MDA-MB-231. Due

to the use of one tissue in the well-plate system, the amounts of LDH in the microfluidic system were also calculated for one tissue. A supernatant volume of 1mL was used to assess the LDH content of the slice. First and foremost, the initial peak of LDH releases at the beginning of the experiment (first 24h) was found in all mice trials in the two incubation systems. It is probably due to the damage caused to the surface of the tissue in harvesting, handling, and slicing procedures, which is caused to LDH enzyme leakage in the first hours of incubation. Van Midwoud et al. (2009) and Olubajo et al. (2020) also found a similarly high percentage of LDH release from liver and glioblastoma slices in the first hours<sup>64-32</sup>.

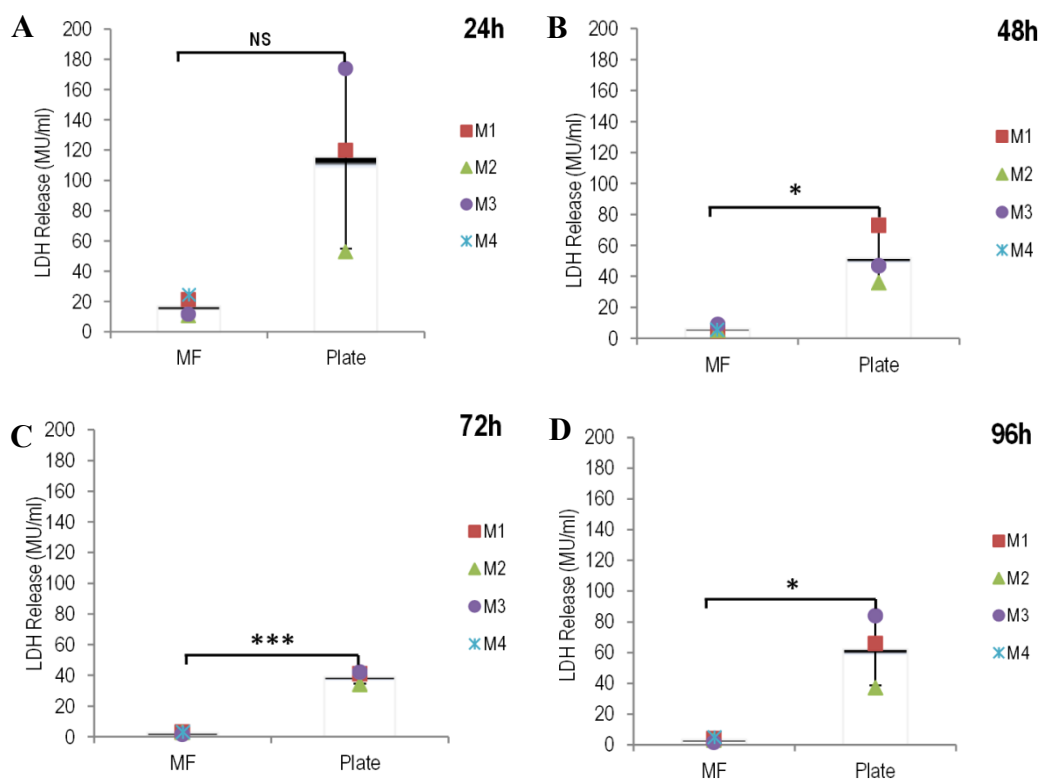


Figure 2.17. Comparison of the amount of LDH released from MDA-MB-231 tissues in the microfluidic and well-plate system over four days (A: 24h, B: 48h, C: 72h, D: 96h). Results are the mean± standard error of the mean (SEM) of four mice, one slice per incubation system per experiment. This difference was statistically significant when tested with a student t-test (\*p<0.05, \*\*p<0.01, \*\*\*p<0.001).

Figure 2.17 demonstrates the level of LDH released from MDA-MB-231 tumor slices decreased by around 50% in the second 24h in both incubation systems (Average: 6.1 Mu/ml for MF system and 52.0 MU/ml for well-plate). After 72h, the rate of decrease remained low in both systems (2.6 Mu/ml for the MF system and 39.0 MU/ml for the well-plate). As shown in figure 2.17, at 96h measurements, the amount of release increased by around 50% at the well-plate system (62.3 MU/ml). However, in microfluidic systems, the LDH leakage remained stable during the last 24h (3.4 MU/ml).

The pattern of LDH release into the effluent from SKBR-3 tumors was distinctly similar to MDA-MB-231 tumors release in both systems. LDH release profiles for SKBR-3 tumors slices in the microfluidic and well-plate systems every 24h during four days were 38.7, 5.4, 3.5, 2.6 MU/ml, and 214.3, 110.7, 44.7, 86.3 MU/ml, respectively. By comparing two systems in both tumors, LDH release results indicated that the tissues in the microfluidic chip system were not damaged by the flow and remained viable during 96h, despite the well-plate culture method (Figure 2.18).

Van Midwoud et al. (2009) showed high viability in the micro-chamber and well-plate system. In both systems, the LDH leakage patterns are similar during 24h. However, the main differences between our system and this published experiment are the thickness of their tissues (100  $\mu\text{m}$ ) and experiment time (24h). By making the thinner slice, the diffusion distance of nutrients and oxygen toward the inner cells of the slice is minimized, so during 24h in the well-plate system, the amount of dead cells is similar to the micro-chamber system. Also, the Van Midwoud group shows that, because PDMS is a relatively hydrophobic polymer, protein LDH was not adsorbing onto the PDMS, and all LDH was released to the supernatant<sup>64</sup>.



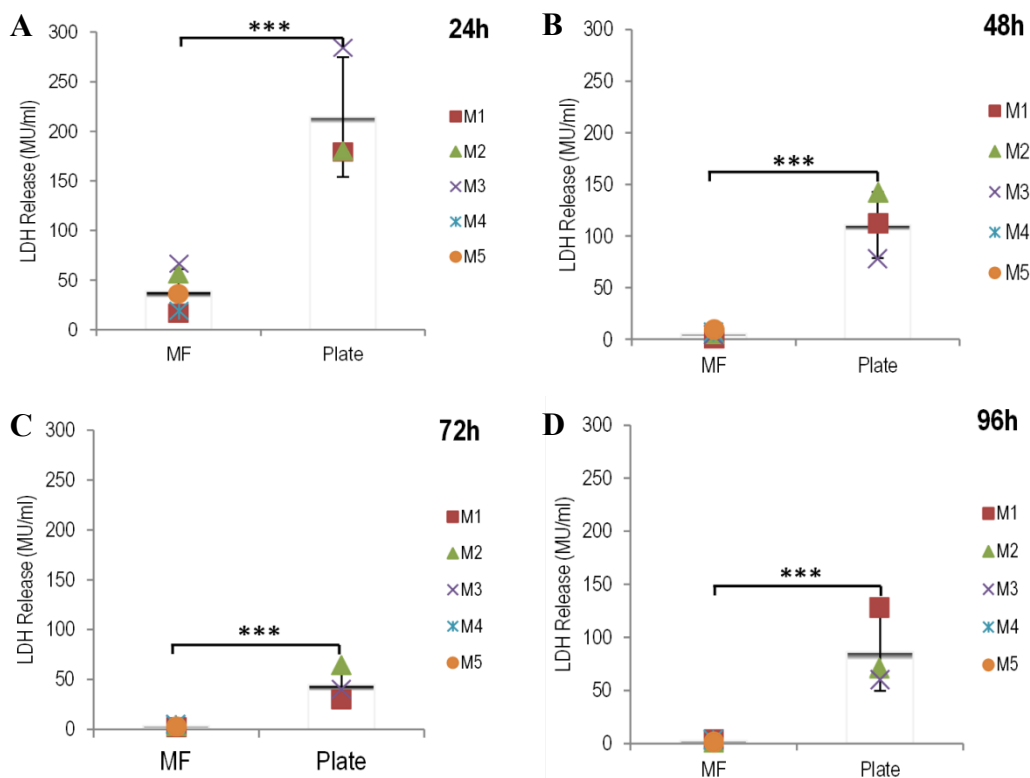


Figure 2.18. LDH release from SKBR-3 tissues at microfluidic and well-plate systems (A: 24h, B: 48h, C: 72h, D: 96h). Results are the mean $\pm$  standard error of the mean (SEM) of five mice, one slice per incubation system per experiment. This difference was statistically significant when tested with a student t-test (\* $p$ <0.05, \*\* $p$ <0.01, \*\*\* $p$ <0.001).

### 2.3.4.2 Metabolic Activity

Glucose levels were measured in the two culture methods at every 24h (Figure 2.19). In contrast to LDH release, the Glucose consumption of the microfluidic chip increases during this period which shows the tissue sections are alive inside the micro-chamber during 96h.

The glucose consumption amount of the well-plate was measured for one slice inside 1ml medium /day, 1ml fresh medium added to each well every day. RPMI-1640 medium contained ~2mg/ml of Glucose, which is sufficient for a slice of tissue culture. As shown in Figure 2.19, the metabolic activity was stable for three

days, while the glucose level decreased by more than four folds and 1.5 folds at the MDA-MB-231 and SKBR-3 tumor slices, respectively at last 24h.

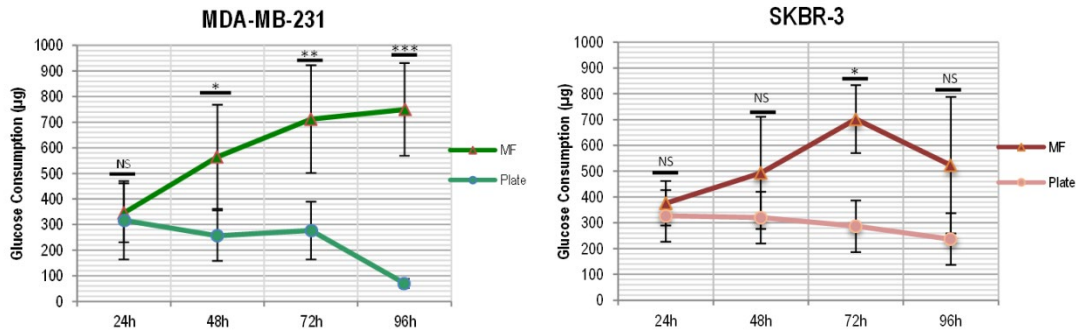


Figure 2.19. Comparison of the metabolic activity of the tumor slices in microfluidic and well-plate systems in terms of glucose consumption for four days. (A) Glucose consumption in MDA-MB-231 tissues at the microfluidic and well-plate systems. (B) Glucose consumption in SKBR-3 tissues at the microfluidic and well-plate systems tissues.

At the microfluidic chip, four slices were cultured on one device by the flow rate of ~20ml/day. 40mg glucose is available at this culture medium for 24h, sufficient for four slices of tissue culture. The quantity of glucose used is determined by subtracting the amount of glucose in a fresh medium from the amount of glucose in the supernatant. The amount of glucose consumption is calculated for one slice in the microfluidic system. Comparing the results of the two culture methods demonstrated that the tumor slice used a remarkably high glucose amount at a microfluidic device during the incubation time. Furthermore, this result shows that the tissue was alive and metabolically active in the microfluidic system even after 96 hours.

## **2.4 Conclusion:**

In conclusion, we successfully developed a new PDMS microfluidic device. Three thin polymer layers with polycarbonate filters at the bottom and top of the microchamber were used. Filters were necessary to ensure an equal distribution of medium flow across the entire chamber; this caused the same pressure over the entire surface of the tissue and prevented the curling up of the slices in the microchamber. When slices are folded or curled up, diffusion distances to inner cells are increased and affect the nutrient and oxygen delivery to inner cells. The characterization reveals a versatile device, which can operate as a suitable platform for tumor slice cultivation with an appropriate amount of oxygen and carbon dioxide. Consequently, our study showed the most intensive metabolic activity observed in tumor slices cultivated in a microfluidic system for up to 96 hours compared with a well-plate system. Using micro-dissected tumor tissue in the microfluidic system will allow studying the therapeutic response in tumor tissue much more closely than in vivo studies. In addition, it may significantly benefit the development of testing of the biopsy samples from patients rapidly for the effectiveness of different chemotherapeutic agents under laboratory conditions in the future.



## CHAPTER 3

### **PALBOCICLIB CONTAINING MAGNETIC PAMAM DENDRIMERS: CONJUGATION AND CHARACTERIZATION STUDIES**

Fabricating nanoscale delivery system composed of MNPs covered with PAMAM dendrimers and using its advantages were fully used to help the chemotherapeutic drug, Palbociclib, effectively reach tumors specifically and stay stable in the circulation longer. We evaluate synthetic approaches for obtaining G5.5 PAL-DcMNPs having carboxyl end groups conjugated with a high drug payload. In order to determine whether conjugate selectivity can be increased for the specific drug type, we report different strategies for loading and conjugation of Palbociclib to different generations (COOH and NH<sub>2</sub> terminal groups) of magnetic PAMAM dendrimers. The best method leading to the highest amount of Palbociclib conjugations was chosen, and the characterization of the PAL-DcMNPs were performed by FT-IR, SEM, TEM, and Zeta ( $\zeta$ ) Potential analysis.

Our knowledge indicates that the proposed approach is novel, and we hope it can provide new insight into the development of Palbociclib targeting delivery.

## **3.1 Experimental Section**

### **3.1.1 Synthesis of Magnetic PAMAM Dendrimers**

Synthesis of magnetic polyamidoamine (PAMAM) dendrimers was previously reported by our group<sup>40</sup>. Different generations of amine and carboxyl end group PAMAM dendrimers were prepared according to the previously described procedure. These synthesized nanoparticles have either positive (with amine end group) or negative (with carboxyl end group) surface charge, suitable size distribution, and targetability properties under magnetic field<sup>40-66</sup>.

### **3.1.2 Loading of Palbociclib on Magnetic PAMAM Nanoparticles (DcMNPs)**

Loading studies on PAMAM dendrimer-coated magnetic nanoparticles to Palbociclib were carried out in Methanol, PBS (pH 7.2), Tris (pH 7.3), and acetate (pH 5.0) buffers. The Palbociclib and DcMNPs complexes were prepared by mixing equal amounts of the drug solution and different amounts of DcMNPs solution followed by gentle rotating (Biosan Multi rotator RS-60) at 37°C for 24, 48, and 72 hours to ensure the complex formation. The nanoparticles loaded with Palbociclib were separated by magnetic separation (Loading Method I and Loading Method II) and Ultracentrifuge methods (Loading Method III). The supernatant was removed and the absorbance was measured at 218 nm with the UV spectrophotometer and HPLC in order to determine the amount of binding of the drug to the nanoparticles.

### 3.1.3 Synthesis of Magnetic PAMAM-Palbociclib Conjugate

The linking of the drug to the dendritic chain was done using a covalent method which consists of several steps. Conjugates were prepared using four different synthetic strategies:

- I. Conjugation Method I: Based on the molecular weights, approximately one drug molecule for each dendrimer end group, 500 $\mu$ g G5.5-PAMAM and 55 $\mu$ g Palbociclib (122.9 $\mu$ mol), were dissolved in DMSO. 15.336  $\mu$ g EDC (80 $\mu$ mol) was added as a coupling agent. The reaction was carried out at room temperature for 72 hours. The solution was further separated and analyzed by HPLC.
- II. Conjugation Method II: 500 $\mu$ g G5.5 DcMNPs, 245 $\mu$ g EDC and 151.15mg Succinic acid were dissolved at 1ml DMSO and stirred for 72h. After incubation, 55 $\mu$ g Palbociclib and 70 $\mu$ g EDC were added to the previous solution and stirred at room temperature for an additional 24h. The solution was further separated and analyzed by HPLC.
- III. Conjugation Method III: 4mg Palbociclib was dissolved at 1ml DMSO. Then 0.88mg Succinic acid (SA) and 0.92mg EDC were added to the solution and mixed for 48 hours at room temperature. The final product was lyophilized for 24h. Obtained carboxylic modified Palbociclib dissolved at 500 $\mu$ l DMSO and then 4mg EDC added as an activated agent and stirred for 2 hours. Finally, 500 $\mu$ g G5.5 magnetic PAMAM dendrimer was added to the solvent and stirred at room temperature for 3 days. The PAMAM G5.5-drug was purified by a magnet. The HPLC method was used to measure the amount of drug after the lyophilization step, and the drug remained in the supernatant after conjugation.
- IV. Conjugation Method IV: 24.40 $\mu$ g Palbociclib (50 $\mu$ mol) and 150 $\mu$ mol EDC were dissolved at 1ml DMSO and stirred for half an hour at room temperature. 100 $\mu$ mol Succinic acid (SA) was slowly added to the solution and stirred for 24h. Excess SA was added in order to obtain a complete

reaction between the drug and SA. Resulting PAL-SA was stirred for 3h at room temperature in the presence of excess 150 $\mu$ mol of EDC. Then 1000  $\mu$ g/ml of PAMAM G5.5 was added to the reaction mixture and stirred at room temperature for 2 days (Figure 3.1). The PAL-PAMAM was purified by magnetic separation and the HPLC method was used to measure the amount of drug in the supernatant<sup>67</sup>. The column used in the HPLC study was selected as Agilent C18 (250 mm x 4.6 mm, 5  $\mu$ m). A solution containing acetonitrile (300:700, 0.1% TFA) was used as the mobile phase. The determined wavelength is 234 nm / 260 nm. The column temperature was set to 40  $^{\circ}$ C. The flow rate is 1.0 ml/min and the sample size is 10  $\mu$ l. HPLC measurements were carried out in METU Central Laboratory.

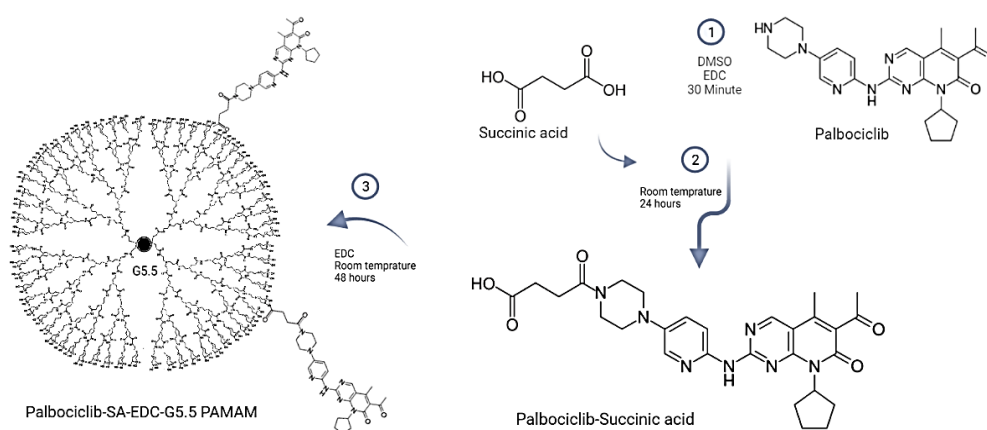


Figure 3.1. Schematic for Palbociclib-Succinic acid- G5.5 PAMAM conjugation.

### 3.1.4 Characterization of Drug Conjugated DcMNPs

The particle shape and size of the synthesis of nanoparticles loaded with Palbociclib were monitored by electron microscopy (TEM and SEM). In addition, the characterization of DcMNPs loaded with Palbociclib were carried out with potential analyzes of FTIR and zeta-potential. The FT-IR analysis, Transmission Electron Microscopy (F.E.I. Tecnai G2 Spirit BioTwin), SEM, and Zeta-Potential (Malvern NanoZS90) measurements were carried out in METU Central Laboratory.



## **3.2 Results & Discussions**

### **3.2.1 Loading and Conjugation of Palbociclib on Magnetic PAMAM Dendrimer**

The loading of antitumor drugs on magnetic nanoparticles protects the drug from degradation, targets it to the tumor site, and maintains the drug release in the tumor cell. Therefore, delivering Palbociclib directly to the tumor site, while keeping high efficacy combined with low systemic exposure, is essential therapeutically. In this study, we used two different strategies, loading and conjugation, to obtain the highest binding concentration of Palbociclib in DcMNPs.

#### **3.2.1.1 Loading of Palbociclib on DcMNPs**

Loading studies of Palbociclib on DcMNPs have been optimized using different buffer solutions (dH<sub>2</sub>O, PBS, Methanol, TRIS-HCL, and Potassium phosphate) and different generations (3, 3.5, 4, 4.5, 5, 5.5, 7, and 7.5) of DcMNPs. In order to find appropriate DcMNPs generation, the various concentrations of the drug and 2.5 mg/ml of different generations of DcMNPs mixtures were prepared. Solutions were incubated on a rotator for 24, 48, and 72 hours at room temperature while protected from light. The nanoparticles loaded with Palbociclib were separated by the magnetic separation method and the absorbance was measured from the supernatant at 218 nm with both a UV spectrophotometer and HPLC methods. By these methods, it was detected that less than 30% of Palbociclib loaded onto different generations of DcMNPs. The data obtained from loading studies showed that Palbociclib was most loaded to DcMNPs in methanol. The nanoparticle generations in which the drug was best loaded were identified as G5 and G5.5. According to the literature, since the terminal carboxyl groups of the G5.5 generation were less toxic than the amine groups in G5, G5.5 nanoparticle

generation was selected, and the subsequent studies were continued with this generation<sup>40</sup>.

To find a proper concentration of G5.5 DcMNPs, which the drug was most loaded in methanol, different concentrations of DcMNPs (1-800 µg/ml) were prepared and all mixed with the same amount (5µg/ml) of Palbociclib. The best result was obtained as 45% with 500µg/ml DcMNPs. For increasing the percentage of loading drug to DcMNPs, the Ultracentrifugal separation method was also used. The same amount of PAMAM-coated MNPs and Palbociclib were mixed for 24h and then applied to 20000, 80000, 100000, and 150000 g ultracentrifugation to increase the precipitation efficiency of the particles. It was observed that 5 µg/ml Palbociclib was bound to 500 µg / ml DcMNPs at 100000 g with the encapsulation efficacy of 51%. Thus, the percentage of loading was increased from 45% to 51% after Ultracentrifugation.

### **3.2.1.2 Conjugation of Palbociclib to DcMNPs**

A critical issue in dendritic drug delivery systems is achieving a high drug payload. It may be possible that some of the dendrimer-drug conjugates show less therapeutic activity compared to free drugs due to relatively low drug payload, decoupling immediately after conjugation, or the lack of drug release from the conjugate. However, the carrying capacity of each polymer typically depends on the total number of reactive groups. Therefore, the main focus of this study was to synthesize DcMNPs conjugates with relatively high Palbociclib loading and increase the conjugations' pharmacological activity inside the cancer cell.

Since the loading of the drug showed a maximum drug payload of approximately 50%, we tried different conjugation methods to increase the Palbociclib payload on the G5.5 DcMNPs. Four different methods were used to prepare the new conjugates. The covalent method for linking the Palbociclib to the PAMAM dendrimer consists of several steps.

In the Conjugation Method I, the drug conjugated directly to PAMAM G5.5 dendrimer in the presence of EDC by coupling to the COOH end group of PAMAM. The resulting dendrimer-EDC conjugate was then linked to Palbociclib. However, the conjugation efficiency of using this method was approximately 15%, so we did not continue with this method.

In Conjugation Method II, we tried to conjugate the Succinic acid to G5.5 DcMNPs in the presence of EDC at DMSO. After 24h incubation, Palbociclib and the excess amount of EDC were added to the previous solution and stirred for an additional 24h. The solution was further separated and analyzed by HPLC. The conjugation efficiency was 23%, which was insufficient for cytotoxicity assays.

In Conjugation Method III, Succinic acid conjugated to Palbociclib by EDC and Pal-SA product was lyophilized for 24h. Obtained carboxylic modified Palbociclib dissolved at DMSO and then EDC added as an activated agent and stirred for 2 hours. Finally, G5.5 magnetic PAMAM dendrimer was added to the solvent and stirred for 3 days. The PAMAM G5.5-drug was purified by a magnet. The HPLC method measured the amount of drug after the lyophilization step and remained drug after conjugation at supernatant. However, in this method, the majority of the drug was lost during lyophilization and the binding efficiency could not be calculated.

In Conjugation Method IV, we developed a new targeting delivery system for Palbociclib. Palbociclib (50 $\mu$ mol) and EDC were dissolved at DMSO. Succinic acid was slowly added to the solution, which links Palbociclib and PAMAM dendrimers. Figure 3.1 illustrates the steps of the synthesis of the PAMAM-drug-PAL conjugate. The HPLC method was used in order to measure the amount of drug in the supernatant. Using this method, we achieved the highest conjugation efficacy as 75% (Table 3.1 and Table 3.2), so we continued characterization and further experiments using this method.

Table 3.3.1. HPLC result for PAL-PAMAM conjugation (Conjugation Method IV).

| HPLC   | Palbociclib | Palbociclib amount at supernatant | PAL - PAMAM conjugation percent |
|--------|-------------|-----------------------------------|---------------------------------|
| Test 1 | 50 $\mu$ M  | 12.34 $\mu$ M                     | 75.3%                           |
| Test 2 | 50 $\mu$ M  | 14.27 $\mu$ M                     | 71.5%                           |

Khandare et al. showed that for the synthesis of biomolecules and their functionalization with other molecules, EDC and other carbodiimides could be used<sup>68</sup>. The ionic bond interaction between Palbociclib and succinic acids causes the preparation of co-amorphous drug systems (Figure 3.1). This system improved the solubility, stability, and dissolution rate of Palbociclib<sup>69</sup>. Furthermore, organic acid conjugated drugs could bind to OH groups of dendrimers<sup>68</sup>.

The toxicity of succinic acid bound Palbociclib was the same as a free drug in breast cancer cell lines (MCF-7 and MDA-MB-453). Meanwhile, the co-amorphous drug did not have toxic side effects on normal breast cancer cells (MCF-10A) and renal epithelial cells (293T)<sup>69</sup>. Conjugation of the drug by a pH-sensitive linker provided the release of the drug after hydrolysis in a tumor acidic environment and after entering the lysosomes<sup>67</sup>. Marcinkowska et al. showed PAMAM-Docetaxel/Paclitaxel conjugates by this method and also showed the toxicity of the drug conjugated nanoparticles in the SKBR-3 and MCF-7 cells. Analyses of cytotoxicity, cellular uptake, and internalization of the conjugates by this group suggest that they represent promising vehicles for HER-2-expressing tumor-selective delivery<sup>67</sup>.

Table 3.3.2. The comparison of different drug loading and conjugation methods in terms of drug payload in DcMNPs

| Magnetic PAMAM (G5.5) | Solution        | Palbociclib ( $\mu$ g/ml) | Drug Payload Method    | Drug Payload (%) |
|-----------------------|-----------------|---------------------------|------------------------|------------------|
| 2.5mg/ml              | Methanol        | 50                        | Loading Method I       | 30               |
| 500 $\mu$ g/ml        | Methanol        | 5                         | Loading Method II      | 45               |
| 500 $\mu$ g/ml        | Methanol        | 5                         | Loading Method III     | 51               |
| 500 $\mu$ g/ml        | DMSO - EDC      | 55                        | Conjugation Method I   | ~15              |
| 500 $\mu$ g/ml        | DMSO - EDC - SA | 55                        | Conjugation Method II  | 23               |
| 500 $\mu$ g/ml        | DMSO - EDC - SA | 4000                      | Conjugation Method III | -                |
| 1000 $\mu$ g/ml       | DMSO - EDC - SA | 24.40                     | Conjugation Method IV  | 75               |

### 3.2.2 Characterization of Palbociclib Conjugated G5.5 PAMAM DcMNPs

FTIR, Zeta ( $\zeta$ ) Potential, TEM, and SEM analyses were performed to characterize Palbociclib conjugated G5.5 PAMAM DcMNPs obtained by Conjugation Method IV.

#### 3.2.2.1 Fourier Transform Infrared Spectroscopy (FTIR)

The FTIR analyses were performed to compare the structures of bare G5.5 PAMAM magnetic nanoparticles, Palbociclib conjugated G5.5 PAMAM magnetic nanoparticles, and free Palbociclib (Figure 3.2).

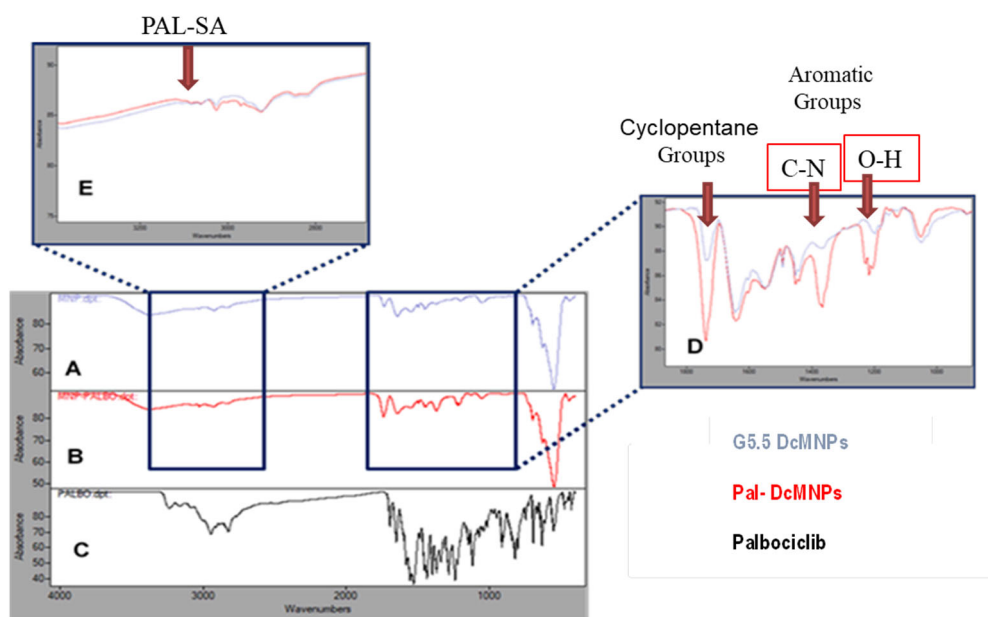


Figure 3.2. FTIR spectra of (A) Bare G5.5 PAMAM DcMNPs, (B) Palbociclib Conjugated DcMNPs, (C) Free Palbociclib, (D) and (E) Comparison of FTIR Analysis of bare G5.5 PAMAM DcMNPs and Palbociclib conjugated DcMNPs peaks in 1000-1800 and 2000-3200, respectively.

A significant difference was observed in the FTIR spectrum of bare G5.5 DcMNPs and Palbociclib conjugated DcMNP between 1180-1250  $\text{cm}^{-1}$  and 1330-1410  $\text{cm}^{-1}$ . The 1180-1250  $\text{cm}^{-1}$  range indicates the C-O bonds, while the aromatic groups, O-H and C-N bonds, were observed between 1330-1410  $\text{cm}^{-1}$ .

The peak vibrations between 1700-1820 show the groups of cyclohexane and cyclopentane. Cyclopentane groups were observed in the Palbociclib conjugated DcMNPs (Figure 3.2, D). For free Palbociclib, the vibrations of N-H and C-H bonds were observed between 2750-3020  $\text{cm}^{-1}$ , whereas in Palbociclib conjugated DcMNPs, these bonds were seen between 2800-3080  $\text{cm}^{-1}$ . Also, PAL-SA had a peak between these ranges at Pal-DcMNPs conjugation (Figure 3.2, E)<sup>69</sup>. Thus these results confirm that Palbociclib was successfully conjugated onto the G5.5 PAMAM DcMNPs.

### 3.2.2.2 Zeta ( $\zeta$ ) Potential

The zeta potential values of drug conjugated magnetic nanoparticles were measured in deionized water (pH 7.5) with Zetasizer Nano. The data obtained from Zeta Potential Analysis showed that bare G5.5 generation was negatively charged (-11.6 mV) at neutral pH (Figure 3.3, A). This indicates that terminal carboxyl groups are present in the G5.5 generation. Furthermore, the zeta potential of Palbociclib conjugated G5.5 DcMNPs was determined as +38.2 mV (Figure 3.3, B). The conjugation of Palbociclib on G5.5 DcMNPs could explain this significant increase in zeta potential from -11.6 mV to +38.2 mV and neutralization of the negative charge on the nanoparticle surface.

The zeta potential indicates the degree of repulsion between adjacent, similarly charged particles in the dispersion. For particles that are small enough, a high zeta potential will confer stability, i.e., the solution or dispersion will resist aggregation. Conversely, when the zeta potential is low, attraction exceeds repulsion and the dispersion will break and flocculate. So, colloids with high zeta potential (negative

or positive) are electrically stabilized, while colloids with low zeta potentials tend to coagulate or flocculate<sup>70</sup>.

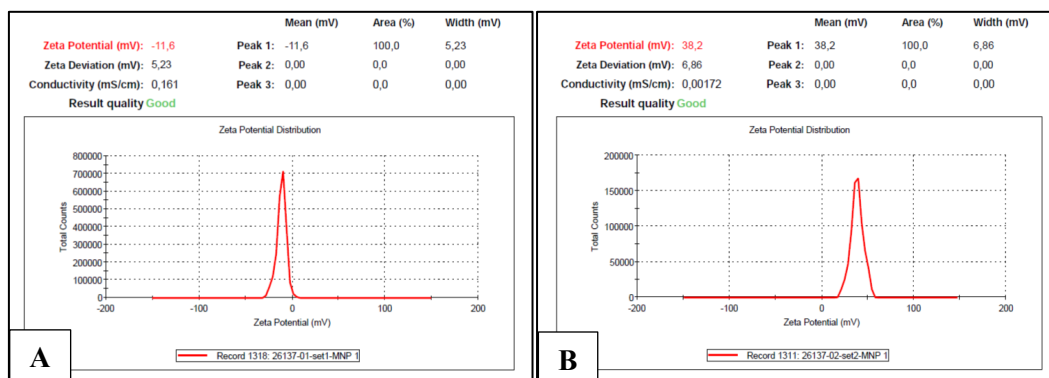


Figure 3.3. Zeta potential measurements of bare G5.5 DcMNPs (A) and Palbociclib conjugated G5.5 DcMNPs (B).

### 3.2.2.3 Transmission Electron Microscopy (TEM)

The particle shape and size of the G5.5 DcMNPs conjugated with Palbociclib were observed by scanning electron microscopy (TEM) analysis. According to TEM analysis, the average particle size of the bare G5.5 generation is around 11-13 nm<sup>40</sup> and drug-conjugated nanoparticle dimensions were determined to be 12-14nm (Figure 3.4).

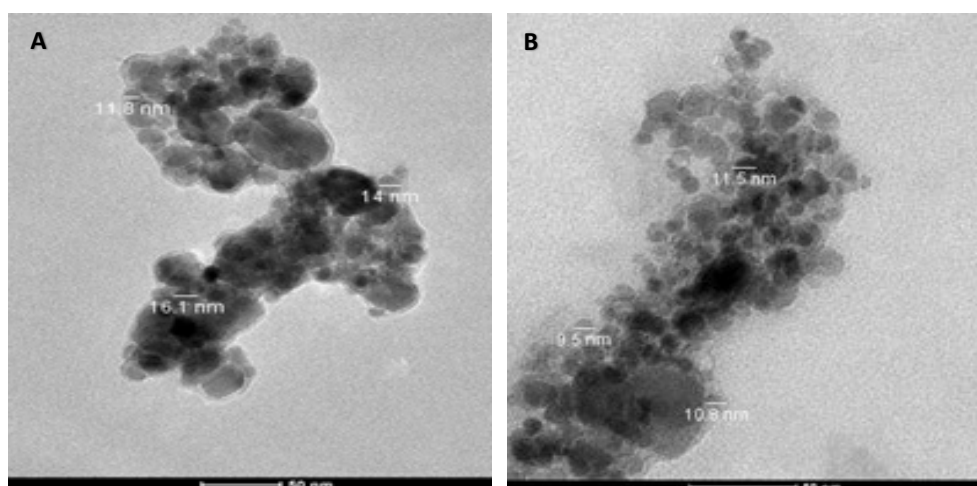


Figure 3.4. TEM images of bare G5.5 PAMAM DcMNPs (A) and Palbociclib conjugated G5.5 PAMAM DcMNPs (B).

### 3.2.2.4 Scanning Electron Microscopy (SEM)

The particle shapes and sizes of drug-conjugated and unconjugated nanoparticles were observed by scanning electron microscopy (SEM). SEM images of bare G5.5 PAMAM DcMNPs and Palbociclib conjugated G5.5 DcMNPs indicate the surface properties and size distribution of nanoparticles. According to the results, it was determined that G5.5 PAMAM MNPs showed a homogeneous distribution on the surface and the particle size was approximately 20 nm. The size of the nanoparticles conjugated with the drug was found to be 45 nm (Figure 3.5).

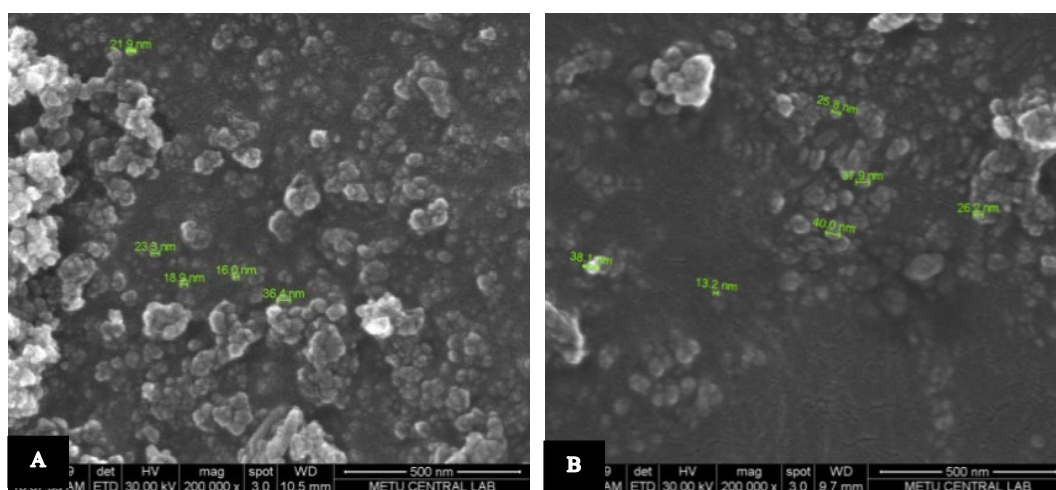


Figure 3.5. SEM images of (A) bare G5.5 DcMNPs and (B) Palbociclib conjugated G5.5 DcMNPs.



### **3.3 Conclusion:**

Drug targeting and controlled drug release systems in cancer treatment have many advantages over conventional chemotherapy in terms of limiting the systemic toxicity and side effects and also overcoming drug resistance. PAMAM dendrimer-coated magnetic nanoparticles (DcMNPs) maintain a suitable drug delivery system due to their surface functional groups, small sizes, and targeting ability under the magnetic field.

The present study presents many loading and conjugation methods that indicate different amounts of Palbociclib with various generations of PAMAM dendrimers. According to the HPLC and characterization results, the most efficient Palbociclib conjugation to magnetic PAMAM dendrimers was approximately 75 percent. The synthesized PAL-DcMNPs have a high potential to be used as a tumor-targeting and pH-responsive drug delivery system due to pH-sensitive linkers. Therefore, it can be an efficient system to reduce the side effects of drugs and also eliminate drug resistance in cancer cells.



## CHAPTER 4

### **COMPARISON OF THE THERAPEUTIC EFFECTS OF PALBOCICLIB AND PALBOCICLIB CONJUGATED MAGNETIC NANOPARTICLES ON 2D, 3D, AND EX-VIVO BREAST CANCER MODELS**

Cytotoxicity of drug and cell viability testing is essential for drug effect analyses, especially in cancer studies. Conventional analysis methods utilize a large population of cells and approximate the results. Nowadays, several methods have been reported for screening small samples of cells to enable high throughput and reliability with reduced cost. In addition, drug targeting and controlled drug release systems in cancer treatment have many advantages over conventional chemotherapy in terms of limiting the systemic toxicity and side effects and overcoming drug resistance. Drug-loaded nanoparticles' efficacy depends on the cellular uptake and the release of the drug from the internalized nanoparticles.

Palbociclib is a type of targeted drug which is effective in the treatment of different types of tumors, especially against advanced stage or metastatic, hormone receptor-positive (ER+, PR+), HER2 negative breast cancer.

This study aimed to show the anti-cancer activity of Palbociclib and Palbociclib conjugated magnetic PAMAM dendrimers (DcMNPs) on 2D, 3D, and Ex-vivo breast cancer cultures.

## **4.1 Experimental Section**

### **4.1.1 Cell Culture (2D culture)**

MCF7, SKBR3, and MDA-MB-231 cells were maintained in RPMI 1640 medium supplemented with heat-inactivated fetal bovine serum (FBS) (10% (v/v)) and gentamicin (1% (v/v)) in tissue culture flasks. Cells were incubated in a Heraeus incubator (Hanau, Germany) at 37°C supplemented with 5% CO<sub>2</sub>. The cells were subcultured; when they reached 80% confluency. Subculturing monolayer cells involves removing the medium and washing them in 5ml PBS. Afterward, 1-2 ml of trypsin-EDTA solution (Biological Industries, Israel) was added for 5-7 minutes at 37°C. After detaching the cells, a full medium was added and homogenized by pipetting. Finally, the cells were centrifuged (5 min at 1500 rpm), pellet resuspended at medium and cultured at the desired concentration at flasks.

Cell counting was done after the trypsinizing step, with the ratio of 9:1, by 0.5% trypan blue solution (Biological Industries, Israel) and the hemocytometer (Thoma, ISOLAB).

#### **4.1.1.1 Cellular Uptake of FITC Modified DcMNPs in 2D culture**

Generation five carboxyl end group (G5.5) DcMNPs were conjugated with Fluorescein isothiocyanate (FITC) in Ethyl Dimethylaminopropyl Carbodiimide (EDC) and N-Hydroxysuccinimide (NHS) solutions to observe cellular uptake into MCF-7, MDA-MB-231, and SKBR-3 breast cancer cells. The conjugation process was carried out with the surface activation method of EDC/NHS solutions<sup>71</sup>. In this method, 100µl FITC (1mg fluorescein was dissolved in 1ml DMSO) followed by the addition of 20 mg EDC and 4.6 mg NHS, which were dissolved in 2 ml of PBS (pH 5.8) and remained at 4°C for 2h<sup>67</sup>. Then, G5.5 DcMNPs (5mg/ml) was added to the solution and rotated (Biosan Multi RS-60 Rotator) at 100 rpm with 25 seconds vibration intervals overnight in the light-protected tubes at 4°C. After

incubation time, particles were separated via magnetic decantation and washed several times with PBS until the supernatant turned colorless. The obtained FITC-DcMNPs were resuspended in medium to a final concentration of 250 $\mu$ g/ml.

#### **4.1.1.1.1 Confocal Microscopy Analysis**

MCF-7, MDA-MB-231, and SKBR-3 cells, plated at a  $5 \times 10^5$  cells/ml density in 6-well plates, were used for uptake studies. After 24h of culture, when they formed confluent monolayers, each cell monolayer was rinsed thrice and re-incubated with FITC-DcMNPs solution (250 $\mu$ g/ml) for 24 h at 37°C. The experiment was terminated by washing the cell monolayer three times with ice-cold PBS. The resultant cells conjugated with FITC-DcMNPs were visualized by confocal microscopy (Leica Microsystems DM 2500).

#### **4.1.1.1.2 Flow Cytometry Analysis**

To provide sufficient cells for Flow Cytometry analysis,  $3.5 \times 10^5$  MCF-7, MDA-MB-231, and SKBR-3 cells were cultured in 2ml medium in each well of 6-well plates 24 h in a humidified environment at 37°C and 5% CO<sub>2</sub> until a 70–80% confluence was reached. Then, the medium was removed entirely and replaced with a fresh medium with 250 $\mu$ g/ml G5.5 FITC-DcMNPs<sup>72</sup>. The exposure was varied for 1, 2, 4, 6, 8, and 24 h with a constant amount of DcMNPs. After the exposure time, each cell line was prepared for Flow Cytometry analysis separately. Only viable cells were collected for analysis. Cells were washed with PBS and detached with trypsin. After centrifuging, cells were washed and resuspended at PBS. At least 20,000 events per sample were analyzed. Side scattering (SSC) and forward scattering (FSC) were measured by flow cytometry (BD Biosciences, USA).

#### **4.1.1.2 Anticancer Drug Sensitivity Testing in 2D Cell Cultures**

##### **4.1.1.2.1 Cell Viability Assay in 2D Cell Cultures**

MCF-7, SKBR-3, and MDA-MB-231 cells ( $1 \times 10^4$  cells/well) were cultured at 50  $\mu$ l medium in opaque-walled white multiwell plates for a day. The cells were treated with different concentrations (2.5, 5, 15, 25, 30, and 50  $\mu$ M) of Palbociclib (Sigma-Aldrich, USA) and Palbociclib conjugated DcMNPs for 96h. After incubation time, the plate and its contents were equilibrated to room temperature (22–25°C) for approximately 30 minutes. An equal volume of CellTiter-Glo® (Promega, G9681) reagent and cell culture medium was added to each well. The contents were mixed vigorously for 5 minutes to induce cell lysis. The plate was incubated at room temperature for an additional 25 minutes to stabilize the luminescent signal. Luminescence was recorded by the SpectraMax iD3 microplate reader.

##### **4.1.1.2.2 Lactate Dehydrogenase Analysis in 2D Culture**

The MCF-7, SKBR-3, and MDA-MB-231 cells were seeded in 96-well plates ( $1 \times 10^4$  cells/well) in 50  $\mu$ L of media and then treated with different concentrations (2.5, 5, 15, 25, 30, and 50  $\mu$ M) of Palbociclib, PAL-DcMNPs, and bare DcMNPs. The PAL-MNPs were washed twice by PBS to remove the excess amount of drug and DMSO after precipitation by a magnet and resuspended at desired concentration with 5% RPMI 1640 medium. The treated cells were then incubated for 24, 48, 72, and 96 hours. Then, non-treated (control) and treated cells (100  $\mu$ l) were transferred to separate eppendorf tubes and centrifuged at 1000rpm for 5 min to remove cell debris. The total amount of released enzyme was determined using a Lactate Dehydrogenase (LDH) Colorimetric Assay kit. Next, 5  $\mu$ l of all media was added to 45  $\mu$ l assay buffer, and 50  $\mu$ l of reaction mix was added. The absorbance of NADH Standard, positive controls, and samples were measured immediately at OD 450 nm (T1) on a microplate-reader (SpectraMax iD3 microplate reader) in a

kinetic mode every 2 minutes for 60 minutes (T2) at 37°C protected from light. The LDH activity in the test samples was calculated by using Equation 1.

$$\text{Equation 4.1. } LDH \text{ Activity} = \left( \frac{\beta}{\Delta T \times V} \right) \times D = nmol/min/mL = mU/mL$$

Where:  $\beta$  = Amount of NADH in sample well calculated from standard curve (nmol),  $\Delta T$  = Reaction time (minutes),  $V$  = Original sample volume added into the reaction well (mL) and  $D$  = Sample dilution factor.

#### **4.1.1.3 RT-PCR Tests**

##### **4.1.1.3.1 RNA Isolation and cDNA Synthesis**

MDA-MB-231, SKBR3, and MCF7 cells grown in a 6-well plate ( $1 \times 10^6$  cells/well) at 37°C for 24 h were treated with 15  $\mu$ M Palbociclib, DcMNPs, and Pal-DcMNPs for 96h. Untreated cells were used as a control group. After incubation for 96 h, total RNA was extracted using a high pure RNA isolation kit (Roche, Germany) according to the manufacturer's instructions. Then the concentration, purity, and integrity of isolated RNA were evaluated with the NanoDrop spectrophotometer UV/Vis (NanoDrop 2000). Finally, 1mg of total RNA was reverse transcribed into cDNA by the high-capacity cDNA reverse transcription kit (Thermofisher, Katalog No: 4368814).

##### **4.1.1.3.2 Real-Time Polymerase Chain Reaction (RT-PCR)**

Expressions of some essential apoptotic genes such as Bax, Bcl-2, CDH1, MDR1, and mTOR were examined by RT-PCR analysis. The SYBR Green Master Mix (Roche Diagnostics, Switzerland) was used to perform RT-PCR according to the manufacturer's instructions on a LightCycler-® 480 instrument (Roche Diagnostics, Switzerland). The reaction mixture contained 10  $\mu$ L 2x SYBR Green Master Mix, 5  $\mu$ L template cDNA, 1  $\mu$ L of sense and antisense primers, and 1  $\mu$ L

nuclease-free water. Each sample was prepared in triplicates. No template control containing nuclease-free water instead of template cDNA was used to detect the background signal. After an initial pre-incubation step of 10 min at 95°C, 45 cycles of amplification for all primer pairs were carried out. Each cycle included a denaturation step, 10 sec at 95 °C; an annealing step, 20 sec at 60-65 °C (depending on primer); and an elongation step, 25 sec at 72 °C.

Fold changes of Bax, Bcl-2, Puma, CDH1, MDR1, and mTOR genes were normalized to the internal control gene GAPDH and calculated for each sample relative to a no-treatment control. Relative fold-changes in mRNA levels compared to controls were measured using the  $2^{-\Delta\Delta Ct}$  calculations ( $\Delta\Delta Ct = \Delta Ct^{treated} - \Delta Ct^{control}$ ).

#### 4.1.2 Three-dimensional (3D) Hanging Drop Culture Method

MCF-7, SKBR-3, and MDA-MB-231 breast cancer cell lines were reproduced as three-dimensional spheroids by using the hanging drop method. To apply the hanging-drop culture method, the medium was removed from the cells, which reached a sufficient cell occupancy rate, washing with PBS, and trypsin was applied for 5 min. Then, the detached cells were homogenized with a medium, transferred to an eppendorf, centrifuged, and rewashed by a medium. The Cells were counted by the hemocytometer, and concentration was adjusted to  $1 \times 10^4$  cells / 50 $\mu$ l.



Figure 4.1. Spheroid images in the hanging drop method.



Inverted Petri dishes lids were used to culture the cells in drops. PBS was added to the bottom of the Petri dish to prevent evaporation of the medium in drops. Cells were incubated in an oven containing 5% CO<sub>2</sub> at 37 °C for 4 days. 10 µl of drops medium were replaced after the second day. After cell colonies formed a spherical shape (Figure 4.1), spheroids were treated with a free drug, empty nanoparticles and drug-loaded nanoparticles.

#### **4.1.2.1 Assessment of 3D Cells Viability with FDA and PI Dyes by Confocal Microscopy**

In order to show the viability of the spheroids during incubation time, 3-dimensional cells (MCF-7, SKBR-3, and MDA-MB-231) were incubated in the medium for 8 days. Spheroids were then stained by using live/dead cell dyes (Fluorescein diacetate (FDA) and Propidium Iodide (PI), Sigma-Aldrich (USA)) and monitored by confocal microscope to observe layer-by-layer cell viability.

#### **4.1.2.2 Internalization Analysis of FITC-DcMNPs to Spheroids by Confocal Microscopy**

Conjugations of G5.5 magnetic PAMAM dendrimers with FITC were described in Chapter 4, section 4.1.1.1.

For 3D culture uptake studies, MCF-7, MDA-MB-231, and SKBR-3 cells were cultured at a density of  $1 \times 10^4$  cells/ 50µl in droplets. On the fourth day, FITC-DcMNPs solution was applied to the spheroids at 250 µg / ml for 24 hours at 37°C. In order to demonstrate the targetability of G5.5 DcMNPs, magnets (3×3 mm diameter) were applied to some spheroids for 4 days. The experiment was terminated by washing the spheroids three times with ice-cold PBS and visualizing them by confocal microscopy (Leica Microsystems DM 2500).

### **4.1.2.3 Anticancer Drug Sensitivity Testing in 3D Cell Cultures**

#### **4.1.2.3.1 Confocal Microscopy**

In order to observe the viability of the spheroids, 3D cells (MCF-7, SKBR-3, and MDA-MB-231) were incubated with different doses (2.5, 15, 30, and 50 $\mu$ M) of Palbociclib and PAL-DcMNPs for 96 hours. Spheroids were then stained using live/dead cell dyes (FDA and PI) and monitored by confocal microscopy.

#### **4.1.2.3.2 Cell Viability Assay**

The cell viability of spheroids was measured after spheroids were treated for 96h by Palociclib and PAL-DcMNPs at 2.5, 5, 15, 25, 30, and 50  $\mu$ M concentrations. The CellTiter Glu Assay kit is used by the manufacturer's instructions which are described in Chapter 4, section 4.1.1.2.1.

#### **4.1.2.3.3 LDH Assay**

On the fourth day of spheroid cultivation, 3D cells were treated with different concentrations (2.5, 5, 15, 25, 30, and 50  $\mu$ M) of Palbociclib and PAL-DcMNPs. For four days, LDH measurements were done by the LDH Assay Kit every 24 hours. The same procedure, described in Chapter 4, section 4.1.1.2.2, was used for the LDH colorimetric assay.

### **4.1.2.4 RT-PCR Tests**

#### **4.1.2.4.1 RNA Isolation and cDNA Synthesis**

MDA-MB-231, SKBR3, and MCF7 cells were grown by the hanging drop method ( $1 \times 10^4$  cells/drop) at 37°C for four days. After incubation days, the drops were

treated with 15 $\mu$ M Palbociclib, bare DcMNP, and Pal-DcMNPs (15 $\mu$ M) for 96h. Untreated cells were used as a control group. After incubation for 96 h, the spheroids were collected, centrifuged, and trypsinized for 7 minutes. Next, spheroids were distributed by pipetting, and a fresh medium was added. The resuspended cells were then washed with PBS, and total RNA was extracted using a high pure RNA isolation kit (Roche, Germany) according to the manufacturer's instructions. Then the concentration, purity, and integrity of isolated RNA were evaluated with the NanoDrop spectrophotometer UV/Vis (NanoDrop 2000). Finally, 1mg of total RNA was reverse transcribed into cDNA by the high-capacity cDNA reverse transcription kit (Thermofisher, Katalog No: 4368814).

#### **4.1.2.4.2 Real-Time Polymerase Chain Reaction (RT-PCR)**

Expressions of some essential apoptotic genes such as Bax, Bcl-2, IL-6, IL-8, and BRCD1 were examined by RT-PCR analysis. The SYBR Green Master Mix (Roche Diagnostics, Switzerland) was used to perform RT-PCR according to the manufacturer's instructions on a LightCycler-® 480 instrument (Roche Diagnostics, Switzerland). The reaction mixture contained 10 $\mu$ L 2x SYBR Green Master Mix, 5 $\mu$ L template cDNA, 1 $\mu$ L of sense and antisense primers, and 1 $\mu$ L nuclease-free water. Each sample was prepared in triplicates. No template control containing nuclease-free water instead of template cDNA was used to detect the background signal. After an initial pre-incubation step of 10 min at 95 $^{\circ}$ C, 45 cycles of amplification for all primer pairs were carried out. Each cycle included a denaturation step, 10 sec at 95  $^{\circ}$ C; an annealing step, 20 sec at 60-65  $^{\circ}$ C (depending on primer); and an elongation step, 25 sec at 72  $^{\circ}$ C.

Fold changes of Bax, Bcl-2, IL-6, IL-8, and BRCD1 genes were normalized to the internal control gene GAPDH and calculated for each sample relative to a no-treatment control. Relative fold-changes in mRNA levels compared to controls were measured using the  $2^{-\Delta\Delta Ct}$  calculations ( $\Delta\Delta Ct = \Delta Ct^{\text{treated}} - \Delta Ct^{\text{control}}$ ).

### 4.1.3 Ex-vivo Culture

In the ex-vivo culture studies, tumors were developed in CD-1 nude mice with SKBR-3 and MDA-MB-231 cells by subcutaneous injection. In each experiment, when the tumor reached around 1×1 cm, the mouse was anesthetized, and the tumor was removed (explained in Chapter 2- section 2.2.2). After the operation, the removed tumor was immediately placed in a 50ml cold Hank's buffer and transferred in a cold chain. The tumor was dissected within 60 min into 3mm×350 μm pieces and placed into the microfluidic systems.

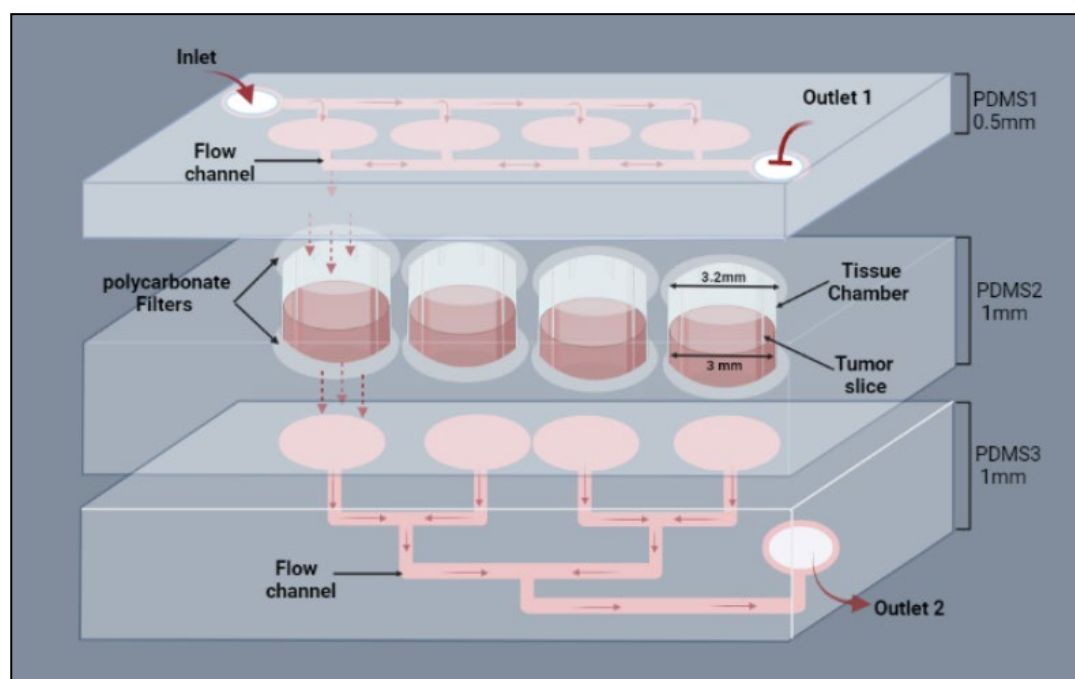


Figure 4.2. Schematic view of the microfluidic system.

In the microfluidic system, four micro-dissected tumor slices were placed in the chambers of the chip between two layers of polycarbonate filters and sealed with the perforated PMMA layers (Figure 4.2). In addition, four 3×3mm magnets were embedded in the down layer of PMMA. These PMMAs were used for targeting drug conjugated magnetic PAMAM dendrimers to micro-dissected slices within the

tissue chambers. Five tumor-included chips were connected to five containers containing the appropriate media for the control group, Palbociclib (15 $\mu$ M), Doxorubicin (1 $\mu$ M), PAL-DcMNPs (15  $\mu$ M), and DOX-DcMNPs (1 $\mu$ M).

Doxorubicin and Doxorubicin-loaded DcMNPs (Dox-DcMNPs) were used as control groups and compared with Palbociclib and Palbociclib-loaded DcMNPs during LDH and metabolic activity experiments.

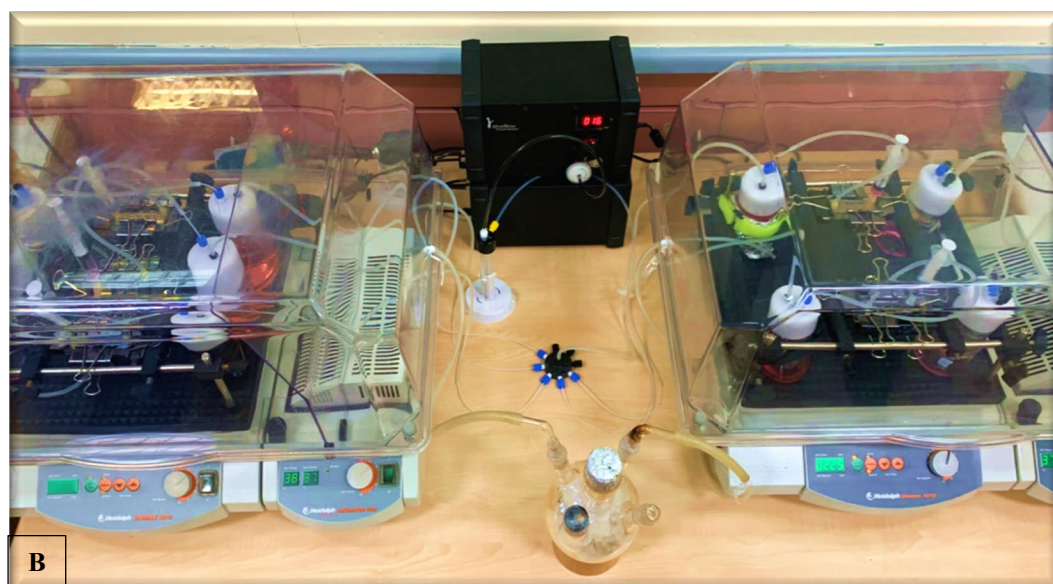
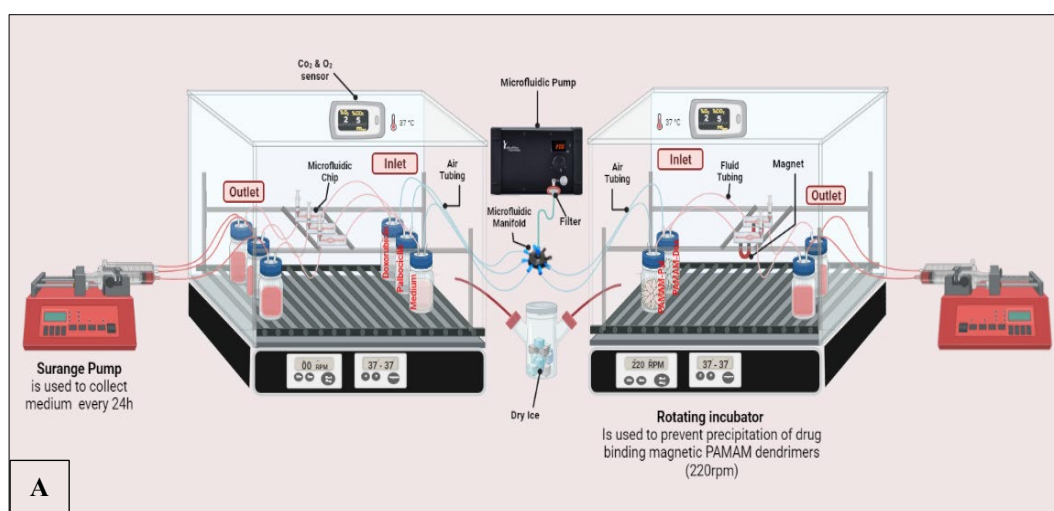


Figure 4.3. A) Schematic, B) real representation of microfluidic chips' incubation systems.

The chips were attached to a calibrated pressure pump by a 9-port microfluidic multi-distribution apparatus. The chips were placed within two in-house incubators with CO<sub>2</sub> and O<sub>2</sub> sensors installed at 37°C. As mentioned in Chapter 2, the notable point is that dry ice provides the required CO<sub>2</sub> for systems. In addition, one incubator was set up to 220 rpm rotating degrees to prevent precipitation of Palbociclib and Doxorubicin-loaded DcMNPs inside containers.

The pressure pump was set to ~19 mbar, so the medium was infused continuously into the chip at a rate of 14 µl/min for 96 h. Fresh media were provided to the tissue samples for 96 h uninterruptedly, and the media coming out of the system were collected every 24 h (by syringe pump connected to outlet containers). Infusions were stopped after 96 h, and micro-dissected tumor samples were removed from the device for post-chip analyses.

#### **4.1.3.1 Internalization of FITC-DcMNPs in Micro-dissected Tissues**

To assess the internalization of bare nanoparticles, the micro-dissected slices were prepared from the SKBR-3 tumor and cultured on two microfluidic chips. One magnet contained a PMMA slide (four 3×3mm magnets) installed under the chip, just below the tissue chambers, for targeting magnetic nanoparticles to tumor slices. The second chip did not contain a magnet for comparison purposes. The micro-dissected pieces were fed by the FITC-DcMNPs (1.7 mg) containing medium (20 ml) for 24 hours. Then slices were picked up and washed with PBS to remove excess nanoparticles. Finally, tissues were observed under the confocal microscope.

#### **4.1.3.2 Anticancer Drug Sensitivity Testing in Ex-Vivo Cultures**

##### **4.1.3.2.1 Tissue Viability Assessment with FDA and PI Dyes by Confocal Microscopy**

To compare the viabilities of micro-dissected MDA-MB-231 and SKBR-3 tumor slices in the microfluidic chip before and after 96 h treatment with Palbociclib and PAL-DcMNPs, control and drug-treated micro-dissected tumor slices were stained by the FDA and PI dyes after incubation time. On the fourth day, slices were incubated at well-plates with 1ml /well PBS containing FDA and PI and rotated for 1 hour. Then tissues were washed with PBS and images were taken. Layer-by-layer photos of each micro-dissected tumor were captured by confocal microscopy. Two replicate samples were used to capture 10 sequential images using a 20x lens for comparison control, Palbociclib, and PAL-DcMNPs treated slices. The contrast of images was improved by using deconvolution software with Huygens essential software (SVI, Hilversum, the Netherlands). Totally six different images were taken from each group (two replicated slices and three shots from different positions of a slice). The intensity sum (px intensity) of fluorescence was calculated by using the MIPAR software<sup>59</sup>.

##### **4.1.3.2.2 LDH Assay**

The lactate dehydrogenase (LDH) was detected daily from the outlet fractions of the microfluidic devices by using an automated biochemistry autoanalyzer (Beckman Coulter DXC800, USA).

##### **4.1.3.2.3 Metabolic Activity**

Glucose levels were measured from the outlet medium of chips by using an automated biochemistry autoanalyzer (Beckman Coulter DXC800,USA) every 24h.

### **4.1.3.3 RT-PCR Tests**

#### **4.1.3.3.1 RNA Isolation and cDNA Synthesis**

In order to isolate RNA from control and drug-treated micro-dissected slices, tissue slices which were triplicates of the same tumor tissue, were pooled together and homogenized using the Ultra Turrax® homogenizer device. Then, RNA isolation was performed by the Trizol method. Spectrophotometric measurements by the Nanodrop device determined the amount and purity of the isolated RNAs. Finally, 1mg of total RNA was reverse transcribed into cDNA using the Transcriptor High Fidelity cDNA Synthesis Kit (Roche).

#### **4.1.3.3.2 Real-Time Polymerase Chain Reaction (RT-PCR)**

The PCR control of the cDNAs was performed by the GAPDH gene amplification. RT-PCR studies for target genes were performed with cDNAs that showed positive results for GAPDH expression.

Expressions of some essential apoptotic genes such as Bcl-2, MDR1, IL6, BRCA1, P53, and IL8 were examined by RT-PCR analysis. The SYBR Green Master Mix was used to perform RT-PCR according to the manufacturer's instructions on a LightCycler® 480 instrument. The reaction mixture contained 10µL 2x SYBR Green Master Mix, 5µL template cDNA, 1µL of sense and antisense primers, and 1µL nuclease-free water. Each sample was prepared in triplicates. No template control containing nuclease-free water instead of template cDNA was used to detect the background signal. The PCR setup was previously explained in section 4.1.1.3.2. Fold changes of Bcl-2, MDR1, IL6, BRCA1, P53, and IL8 genes were normalized to the internal control gene GAPDH and calculated for each sample relative to a no-treatment control. Relative fold-changes in mRNA levels compared to controls were measured using the  $2^{-\Delta\Delta Ct}$  calculations ( $\Delta\Delta Ct = \Delta Ct^{\text{treated}} - \Delta Ct^{\text{control}}$ ).



## 4.2 Results and Discussions

### 4.2.1 2D Culture Results

#### 4.2.1.1 Cellular Uptake of FITC Modified DcMNPs by Confocal Microscopy

The efficacy of drug-loaded nanoparticles depends on the cellular uptake and the released dose of the drug from the internalized nanoparticles within the cells. In order to determine cellular internalization, fluorescent dye (FITC) conjugated DcMNPs were prepared. A fluorescent dye acts as a probe for DcMNPs and offers a sensitive method to assess intracellular uptake. A similar labeling method was used earlier by Arya et al. to investigate the uptake of chitosan nanoparticles in the human pancreatic cancer cell and embryonic kidney cell lines<sup>71</sup>.

The cellular uptake of FITC conjugated G5.5 DcMNPs were visualized in MCF-7, MDA-MB-231, and SKBR-3 breast cancer cell lines by confocal microscopy; (Figure 4.4 and 4.5). The reflection of bright green dots inside and around the nucleus indicates the nanoparticles' intracellular localization, expressing the efficient cellular uptake of the particles. In contrast, the bright-field images show no visible particles on the outside or the surface of the cells.

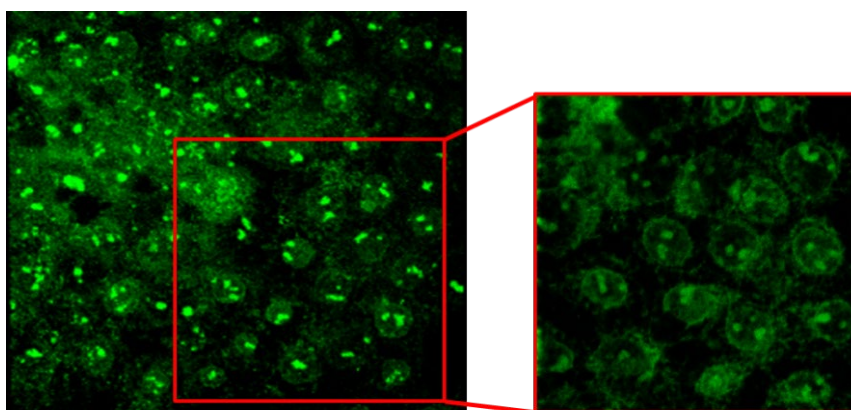


Figure 4.4. Cellular uptake of FITC-DcMNPs by MCF-7 cells by confocal microscopy. (40 X1 and 40 X2 zooms)

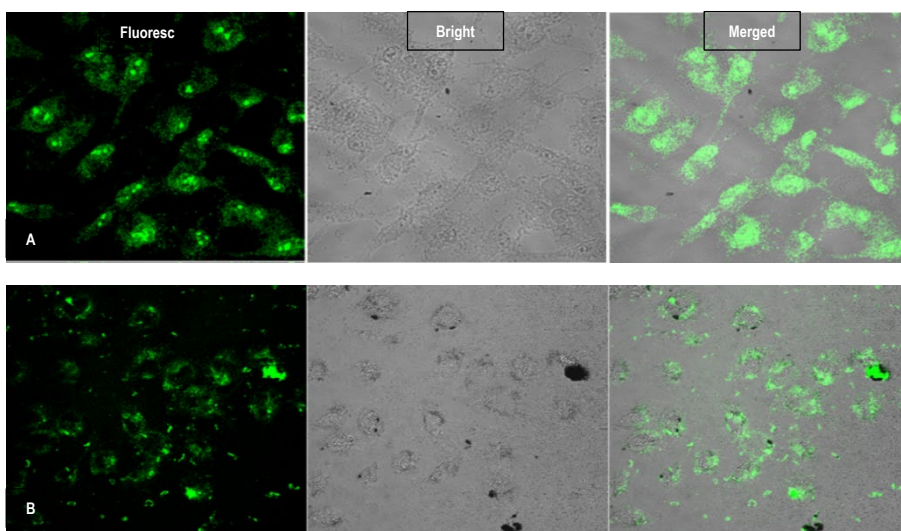


Figure 4.5. Cellular uptake of fluorescent DcMNPs by A) MDA-MB-231, B) SKBR-3 cells

#### 4.2.1.2 Detection of FITC Labeled Magnetic Nanoparticle Internalization in Breast Cancer Cells by Flow Cytometry

Flow Cytometry analysis is a fast and reliable method to study the uptake of modified nanoparticles by cancer cells<sup>72</sup>. The magnetic nanoparticle-exposed and unexposed cells running in flow Cytometry can be distinguished regarding their light scattering and fluorescence signals. The side scattering correlates with the internal granularity of the cells and provides information about the cellular effects after nanoparticle internalization<sup>72</sup>.

As shown in Figure 4.6, significant changes in the side scattering signals (SSC) were displayed in DcMNPs treated cells compared to the control cells. The cytotoxic effects of empty DcMNPs up to 250  $\mu\text{g}/\text{ml}$  concentration were evaluated previously by our group<sup>40</sup>. Bare nanoparticles showed no significant cytotoxicity on MCF-7, SKBR-3, and MDA-MB-231 cells. Treatment with constant FITC-DcMNPs concentrations (250 $\mu\text{g}/\text{ml}$ ) for all cell types showed an increasing time dependence on SSC signals. The exposure was carried for 1, 2, 4, 6, 8, and 24 h

with a constant amount of DcMNPs. All cell lines show the highest uptake efficiency within 24 hours of incubation regarding uptake kinetics.

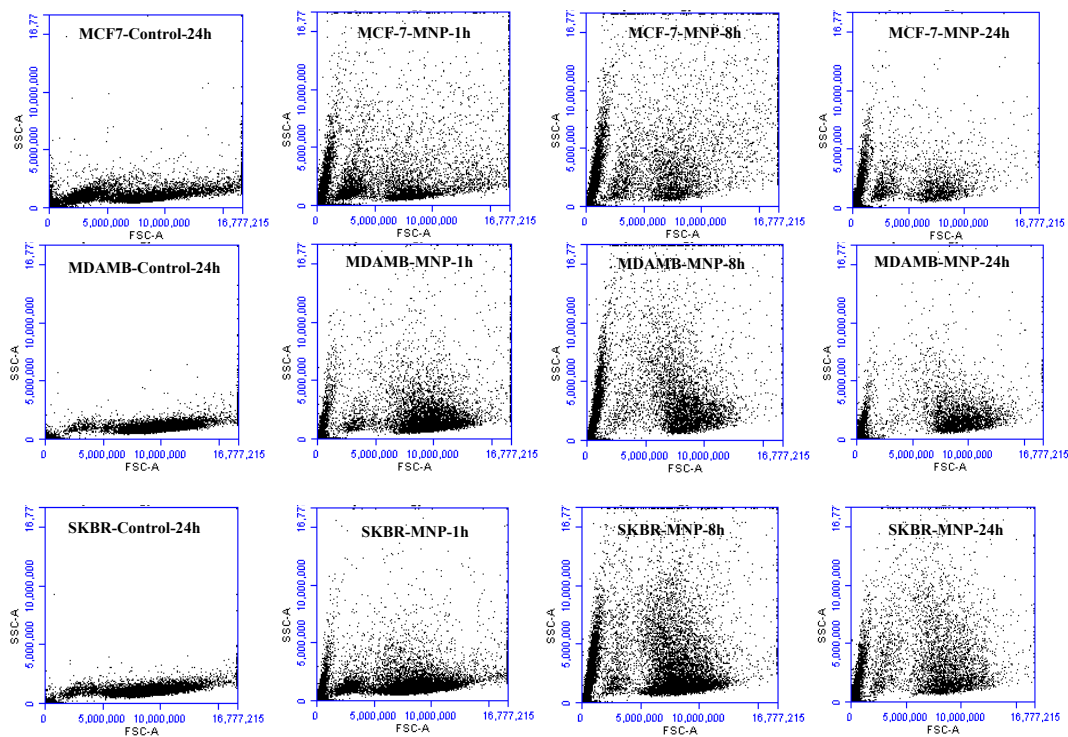


Figure 4.6. Density plot of SSC and FSC signals of MCF-7, MDA-MB-231, and SKBR-3 cells. Cells were incubated with 250 $\mu$ g/ml DcMNPs for 24 hours.

During the first eight hours of incubation, all cell lines show an extremely high uptake rate. Between one and eight hours of incubation, the signal intensity was increased, and between eight and 24 hours, the signal intensity decreased slightly at MCF-7 and MDA-MB-231 cell lines (figure 4.7). A redistribution of the nanoparticles during cell division might explain the decrease in scattering after 24 hours. Jochum et al.; showed the same uptake kinetic for FITC-TiO<sub>2</sub> nanoparticles at A549 and NIH/3T3 cell lines<sup>72</sup>.

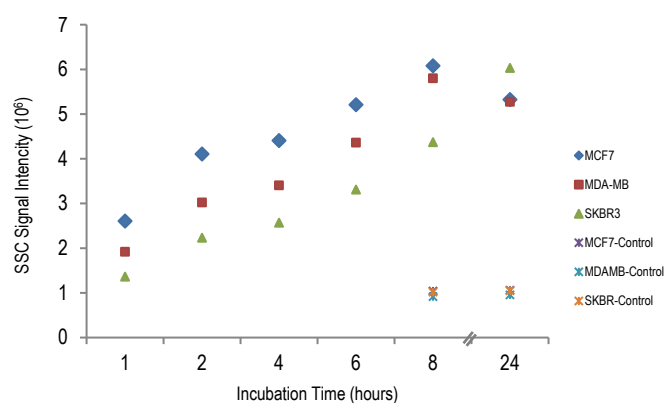


Figure 4.7. Mean SSC signal kinetics of FITS-MNP at MCF-7, MDA-MB-231, and SKBR-3 cells.

The decrease of scattering intensity under 2,500,000 signals in all cell lines demonstrated the time-dependent internalization of nanoparticles. MCF-7 and MDA-MB-231 cell lines show higher uptake than SKBR-3 between 1 to 8 hours of incubation (Figure 4.8). However, after 24h, the internalization amount is the same at all cell lines.

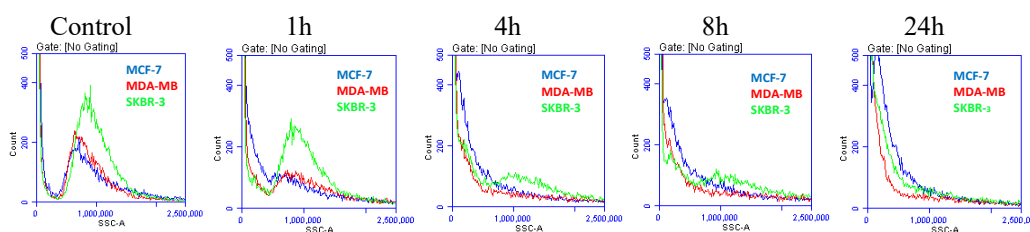


Figure 4.8. Intensity analysis at different incubation times for MCF-7, MDA-MB-231, and SKBR-3 cell lines

#### 4.2.1.3 LDH Cytotoxicity Assay

Lactate dehydrogenase (LDH) release assay was used for cytotoxicity analysis. Measurements were made at 24, 48, 72, and 96 hours of incubation. The release of LDH into the medium demonstrated cell death<sup>73</sup>. It is possible to distinguish between cell death and growth inhibition using an LDH cytotoxicity assay based on

modified LDH<sup>74</sup>. When a cell loses membrane integrity, it releases LDH, which is then used as a catalyst to promote a two-step reaction. The first step is the oxidation-reduction reaction between NAD<sup>+</sup> and lactate. This is followed by the reduction of a tetrazolium salt (INT) to a colored formazan. The colored formazan product can be detected colorimetrically through the absorbance maximum at 450-520 nm.

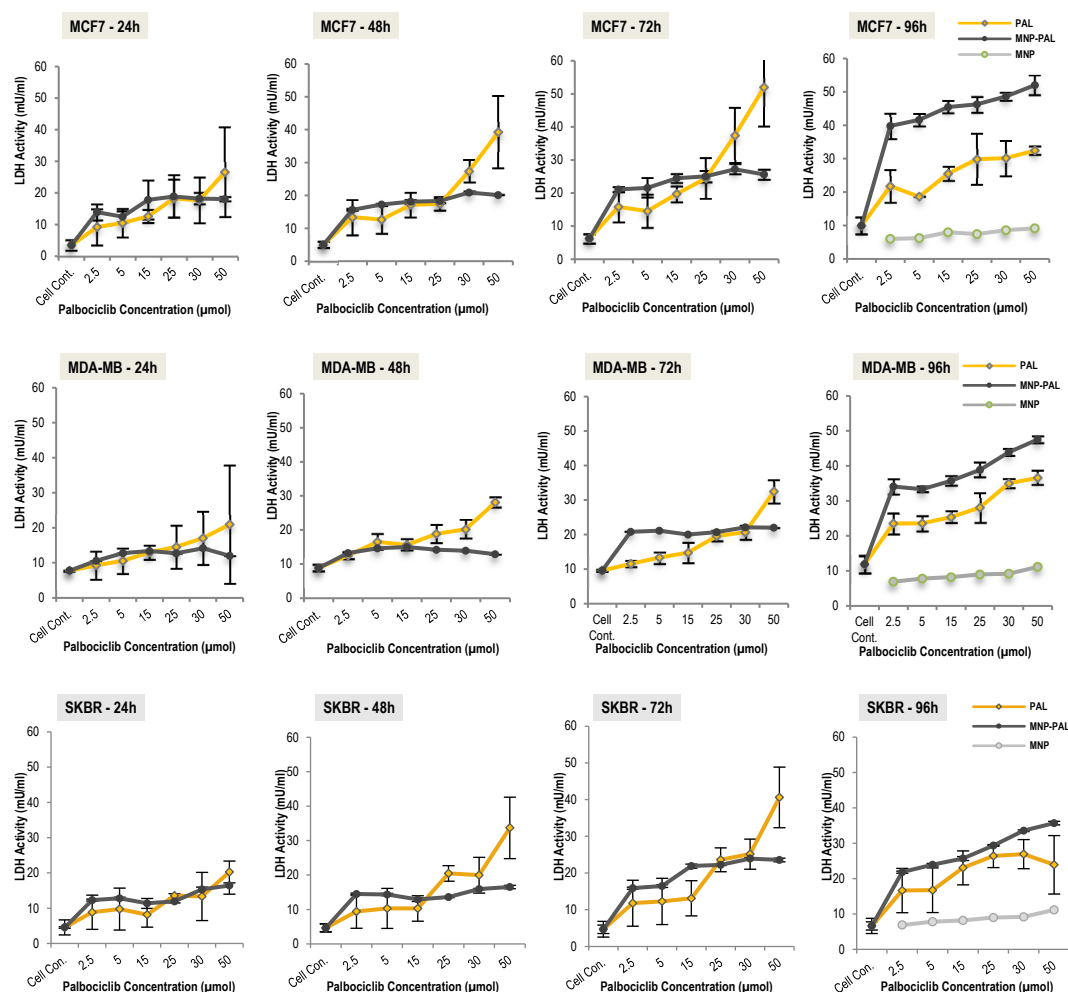


Figure 4.9. LDH activity of (A) MCF-7, (B) MDA-MB-231, (C) SKBR-3

The G5.5 PAMAM dendrimer was conjugated to Palbociclib by the pH-dependent linker. This drug conjugation method is stable in extracellular media<sup>67</sup>. The

carboxyl-terminal dendrimer is transported to the cell by an absorptive endocytosis mechanism<sup>68</sup>. The drug is released in the acidic environment of the lysosome.

The responses of all cell lines to the increasing concentration of Palbociclib and PAL-DcMNPs are shown in Figure 4.9. The results showed the rising release of LDH due to the treatment of PAL-DcMNPs after 96 hours. However, no significant LDH release was seen due to treatment with an increasing concentration of bare DcMNPs (the same amount as PAL-DcMNPs) at 96h.

#### **4.2.1.4 Cell Viability Assay**

The determination of ATP production is a method to analyze cellular viability in anticancer studies. In this study, the CellTiter-Glo® Cell Viability Assay is used to determine the number of viable cells in cell culture after 96 treatments with Palbociclib and PAL-DcMNPs. The metabolic activity of the cell was measured by the production of ATP, and it is based on the conversion of luciferase into oxyluciferin in an ATP-dependent reaction that generates light. Thus, the level of ATP correlates with the amount of light emission. Cell viability can then be correlated to an increase in the overall amount of ATP produced in a population of exponentially growing cells. This assay is particularly useful because it is sensitive enough to reproducibly detect ATP production from a single mammalian cell. An additional benefit is the extended dynamic range of this assay, as a concentration of ATP and cellular viability are directly proportional to cell numbers between one and one hundred million cells.

The cytotoxicity of Palbociclib and PAL-DcMNPs was dose-dependent (Figure 4.10). At the higher concentrations (30-50 $\mu$ M), free Palbociclib has a more cytotoxic effect on MCF-7, MDA-MB-231, and SKBR-3 breast cancer cell lines. However, with Palbociclib conjugated DcMNPs treatment, it has been observed that drug doses that inhibit 50% of the cell viability can be achieved with even lower drug concentrations with respect to free Palbociclib for all of the breast

cancer cell lines. These results show that conjugation of Palbociclib with DcMNPs improved the cytotoxic effect in lower drug concentrations. The observed effects were more evident for MCF-7 cells than for MDA-MB-231 and SKBR3 cells. In addition, the association between cell viability data and LDH release was also observed at a lower dosage of PAL-DcMNPs. The values of LDH are relatively high, considering that viability decreased to 30% at 2.5 $\mu$ M treatment of PAL-DcMNPs at MCF-7 cells.

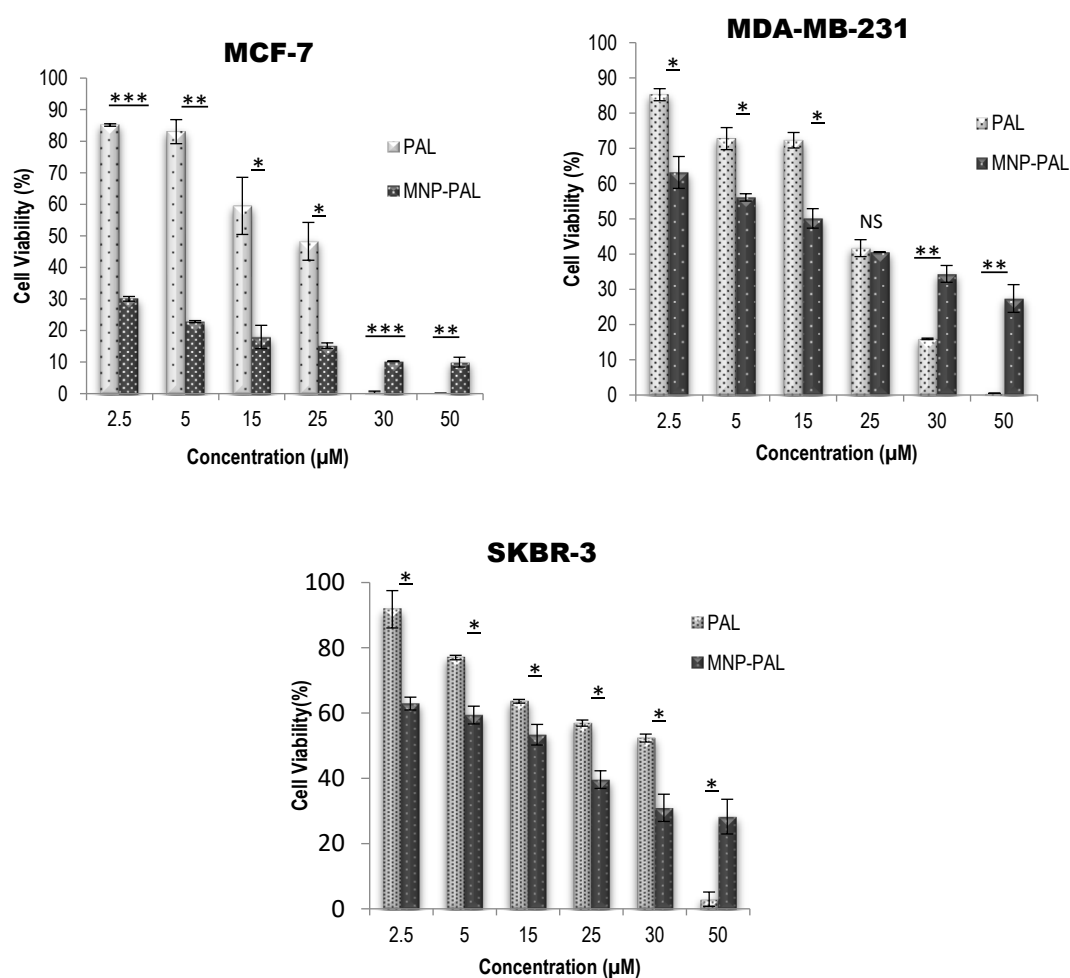


Figure 4.10. CellTiter-Glo<sup>®</sup> Cell Viability Assay (A) MCF-7, (B) MDA-MB-231, and (C) SKBR-3 cell lines. Results are the mean  $\pm$ SEM (n=2). This difference was statistically significant when tested with a student t-test (\*p<0.05, \*\*p<0.01, \*\*\*p<0.001).

#### **4.2.1.5 RT-PCR Results**

##### **4.2.1.5.1 Quantification of the Expression Level of Bax, Bcl-2, CDH1, MDR1, mTOR Genes in Untreated and Treated Breast Cancer Cells**

To elucidate the difference in apoptotic status between untreated and treated breast cancer cells, the expression pattern of the genes related to apoptosis (Bax, Bcl-2), migration (CDH1), drug resistance (MDR1), and cell proliferation (mTOR) in MDA-MB-231, SKBR3, and MCF7 cell lines were examined by qRT-PCR before and after treatment of the cells with 15 $\mu$ M Palbociclib, bare G5.5 PAMAM DcMNPs, and PAL-DcMNPs for 96h.

Apoptosis is the orderly and tightly regulated cellular programmed cell death involving signal transduction pathways that induce cells to self-destruct during embryonic development or in response to environmental hazards or anticancer therapeutics. The molecular mechanism for drug-induced apoptosis is associated with mitochondrial dysfunction that is characterized by a release of cytochrome c from mitochondria. The mitochondrial release of cytochrome c through the anion channel is regulated by Bcl-2 and Bcl-xL, indicating that Bcl-2 plays a critical role in anticancer drug-induced apoptosis. Bcl-2 also interacts with the pro-apoptotic proteins Bax and Bak to block their pro-apoptotic activity, which is activated by apoptotic signals of anticancer drugs<sup>75</sup>. In an evaluation of expression analysis of Bcl-2 and Bax, the ratio of pro-apoptotic Bax to anti-apoptotic Bcl-2 expression was considered as an apoptotic parameter<sup>76-77-78</sup>. According to Figure 4.11, Bax/Bcl-2 ratio increased, followed by PAL-DcMNPs stimulation at the mRNA level in all three cell lines, MDA-MB-231, SKBR3, and MCF7. The increased ratio might be correlated to decreased cell viability of these cell lines after treatment with PAL-DcMNPs. These results could validate our data obtained from the cell viability analysis, which showed that treating with PAL-DcMNPs causes cell death in the breast cancer cell lines.



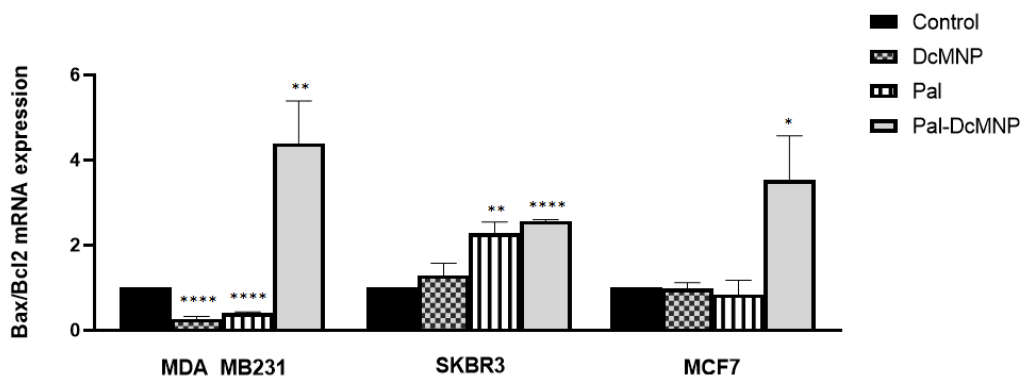


Figure 4.11. Bax/Bcl-2 gene expression ratios in untreated and treated MDA-MB-231, SKBR3, and MCF7 cell lines with 15 $\mu$ M Palbociclib, bare G5.5 PAMAM DcMNPs, and PAL-DcMNPs for 96h, when  $p < 0.05$ .

In order to examine the migratory potential of the breast cancer cells before and after treatment, the expression pattern of the CDH1 gene was investigated. CDH1 (E-cadherin) is a calcium-dependent transmembrane protein that facilitates the assembly of the specialized intercellular junctions necessary for the adherence of epithelial cells<sup>79-80</sup>. According to various in vitro experiments, CDH1 expression is downregulated in colon cancer cell lines which leads to cell migration and invasion<sup>81</sup>. Other studies have indicated that loss of CDH1 expression is related to the metastasis of lymph node<sup>82-83-84</sup> distant metastasis and increased mortality<sup>85-86</sup>.

Since the main regulator of the canonical Wnt signaling, the  $\beta$ -catenin molecule, binds to the cytoplasmic tail of E-cadherin, loss of E-cadherin expression follows by the release of  $\beta$ -catenin into the cytoplasm. Then, the translocation of  $\beta$ -catenin from the cytoplasm into the nucleus leads to triggering the expression of EMT-inducing transcription factors. Together with other mechanisms, E-cadherin loss can lead cancer cells to the mesenchymal state and undergo metastasis. According to the results of the study carried out by Fujita et al., the abundance of CDH1 was distinctly lower in cancer (MCF7 and MDA-MB-231) than in normal breast epithelial cells (MCF10A)<sup>87</sup>. In another study, treatment of luminal-type breast

cancer cell line, T47D, with Palbociclib did not affect the induction of the EMT transcription factors, and it slightly induced CDH1<sup>88</sup>. In this study, qRT-PCR analysis was performed to analyze the expression of CDH1 in the MDA-MB-231, SKBR3, and MCF7 cell lines before and after treatment with Palbociclib, bare G5.5 PAMAM DcMNPs, and Pal-DcMNPs. The results revealed that the CDH1 gene was significantly upregulated in all the treatment groups in comparison to the untreated control group (Figure 4.12). However, the rise of CDH1 expression was higher in the case of PAL-DcMNPs treated cell lines. Combined with the findings of previous studies, it can be said that CDH1 may participate in the PAL-DcMNPs-mediated inhibition of cell proliferation and metastasis.

In literature, there are some data indicating the involvement of Cdh1 in apoptotic cell death, which is initially reported in B-lymphoma. Also, overexpression of Cdh1 can dramatically cause cell susceptibility to natural killer cell (NK) cytotoxicity<sup>89</sup>. Regarding these results, there could be a possible association between CDH1 overexpression and decreased cell viability in MDA-MB-231, SKBR3, and MCF7 cell lines after treatment with PAL-DcMNPs in our study.

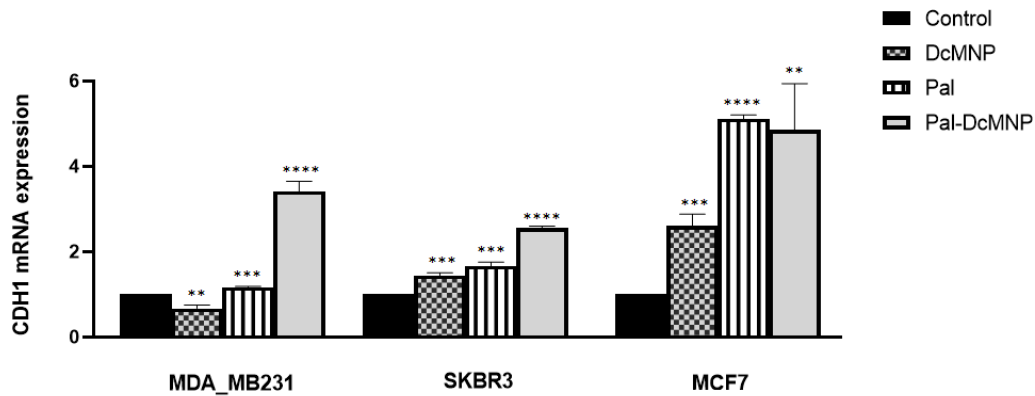


Figure 4.12. Expression levels of CDH1 gene in untreated and treated MDA-MB-231, SKBR3, and MCF7 cell lines with 15uM Palbociclib, bare G5.5 PAMAM DcMNPs, and PAL-DcMNPs for 96h, when  $p < 0.05$ .

P-glycoprotein 1 (multidrug resistance protein 1, MDR1) is considered as an important cell membrane protein, which pumps out many foreign substances from the cells. Consequently, overexpression of P-gp is related to the main mechanism leading to decreasing intracellular drug accumulation and developing of multidrug resistance in human multidrug-resistant (MDR) cancers. According to the US prescribing information of Palbociclib, the in vitro studies showed that at clinically relevant concentrations has low potential to inhibit the activities of the drug transporters P-glycoprotein (P-gp), breast cancer resistance protein (BCRP).

In the light of this information, in this study, we compared the levels of MDR1 mRNA expression in breast cancer cells before and after treatment to assess multidrug resistance expression. According to the results of the mRNA expression of MDR1 in the cell lines before and after treatment (Figure 4.13), we found that after treatment with Palbociclib conjugated DcMNPs, MDR1 gene expression levels did not significantly change in MDA-MB-231 and MCF7 cell lines. However, in SKBR3 cells, a statistically significant decrease was observed in Palbociclib-conjugated DcMNPs cells compared to untreated cells ( $p < 0.05$ ), and it was not altered when treated with Palbociclib and DcMNPs alone, suggesting that this chemotherapeutic drug can decrease the mRNA expression of the MDR1 gene when conjugated with DcMNPs. Our results in MCF7 cells are in consistent with the study performed by Chen et al. (Everolimus Reverses Palbociclib Resistance in ER+ Human Breast Cancer Cells by Inhibiting Phosphatidylinositol 3-Kinase (PI3K)/Akt/Mammalian Target of Rapamycin (mTOR) Pathway), which indicated that there is no significant change in MDR1 gene expression either in mRNA or in protein level in Palbociclib-treated MCF7 cell line.

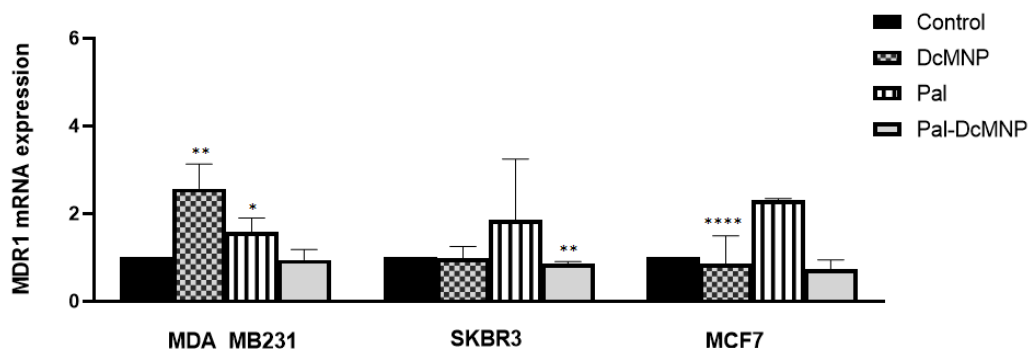


Figure 4.13. Expression levels of MDR1 gene in untreated and treated MDA-MB-231, SKBR3, and MCF7 cell lines with 15 $\mu$ M Palbociclib, bare G5.5 PAMAM DcMNP, and Pal-DcMNPs for 96h, when  $p < 0.05$ .

It is well known that mTOR is one of the Phosphoinositide 3-kinase (PI3K) downstream molecules which regulate cell proliferation, apoptosis, and autophagy<sup>90</sup>. According to the studies, an increase in tumor progression and often a decrease in patient survival is indicated, followed by mTOR signaling activation<sup>91</sup>. The activity of mTOR is frequently upregulated in human cancer<sup>92</sup>. In a study, noncanonical downregulation of mTOR by Palbociclib treatment was indicated in patient-derived SF7761 and SF8628 glioma cell lines, and it was shown that combined use of CDK4/6 and mTOR inhibitors induce synergistic growth arrest<sup>93</sup>. Another study recently reported that Palbociclib treatment increases the activation of AKT/mTOR signaling<sup>94-95</sup>. In our research, it can be seen an upregulation in the expression of mTOR in MDA-MB-231, SKBR3, and MCF7 cell lines treated with free Palbociclib. These results are in consistent with the data obtained from the study performed by Cretella et al., in which Palbociclib induced a dose-dependent up-regulation of the phosphorylation levels of mTOR protein and its activation in MDA-MB-231 and HCC38 cells<sup>96</sup>. Our results indicated upregulation of mTOR after treatment with Palbociclib conjugated DcMNPs in the MCF-7 cell line. However, downregulation of mTOR in the MDA-MB-231 cell line by Palbociclib conjugated DcMNPs treatment was indicated in our data obtained from the qRT-

PCR assay. In the SKBR-3 cell line, no change has been seen after treatment by PAL-DcMNPs.

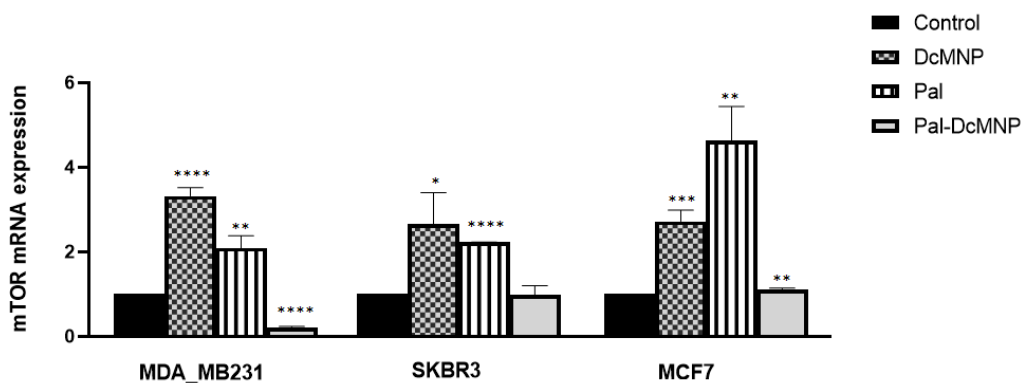


Figure 4.14. Expression levels of mTOR gene in untreated and treated MDA-MB-231, SKBR3, and MCF7 cell lines with 15 $\mu$ M Palbociclib, bare G5.5 PAMAM DcMNPs, and PAL-DcMNPs for 96h, when  $p < 0.05$ .

#### 4.2.2 3D Hanging Droplet Results

To confirm the viability of spheroids during culture time (8 days), we performed live and dead cell counting and Propidium Iodide (PI) uptaking methods.

Cells were trypsinized during culturing days, and live and dead cells were counted after Trypan-Blue staining. We compared the number of live cells in 2D and 3D culture methods. Afterward, the control and 96h Palbociclib treated 2D and 3D MCF-7 cell death were measured by PI uptaking with a fluorescent microplate reader. PI is membrane-impermeant and generally excluded from viable cells. However, during late-stage apoptosis and necrosis, the membrane increases permeability allowing PI to enter the cell and label DNA.

After eight days of cultivation, the results of live and dead cell counting and PI uptaking show a negligible cell death rate in the control 3D culture. The cell death

results in the 3D control group were well-nigh to 2D culture in live and dead cell counting and PI uptaking measurement methods (APPENDIX A).

#### **4.2.2.1 Assessment of Cell Viability of 3D Cultures by Confocal Microscopy**

Morphological structures of MCF-7, SKBR-3, and MDA-MB-231 cell spheres grown in 3D cell culture media were observed to differ. MCF-7 cells are more uniform and tightly connected to each other to form 3D spheres, while MDA-MB-231 cells are more easily dispersible. SKBR-3 cells were cultivated by the same number of MCF-7 and MDA-MB-231 cells, but they formed smaller cell spheres.

In spheroids, the outer layers are proliferating cells with enough oxygen, nutrient, and metabolite gradients, whereas a layer of quiescent viable cells surrounds necrotic core cells. In order to observe the viability of spheroids in the inner and outer layers, FDA and PI stained spheroids were monitored by Confocal microscopy. As mentioned before (Chapter 2, section 2.3.2), the FDA is colorless and membrane-permeable until it is converted to fluorescein by esterases inside the live cells.

Layer-by-layer scrutiny under confocal microscopy showed the viability of the 3D cells (control group) and confirmed the core cells were not necrotic. Furthermore, the number of dead cells stained with PI in the center of the 3D cells appears to be very low (Figure 4.15).

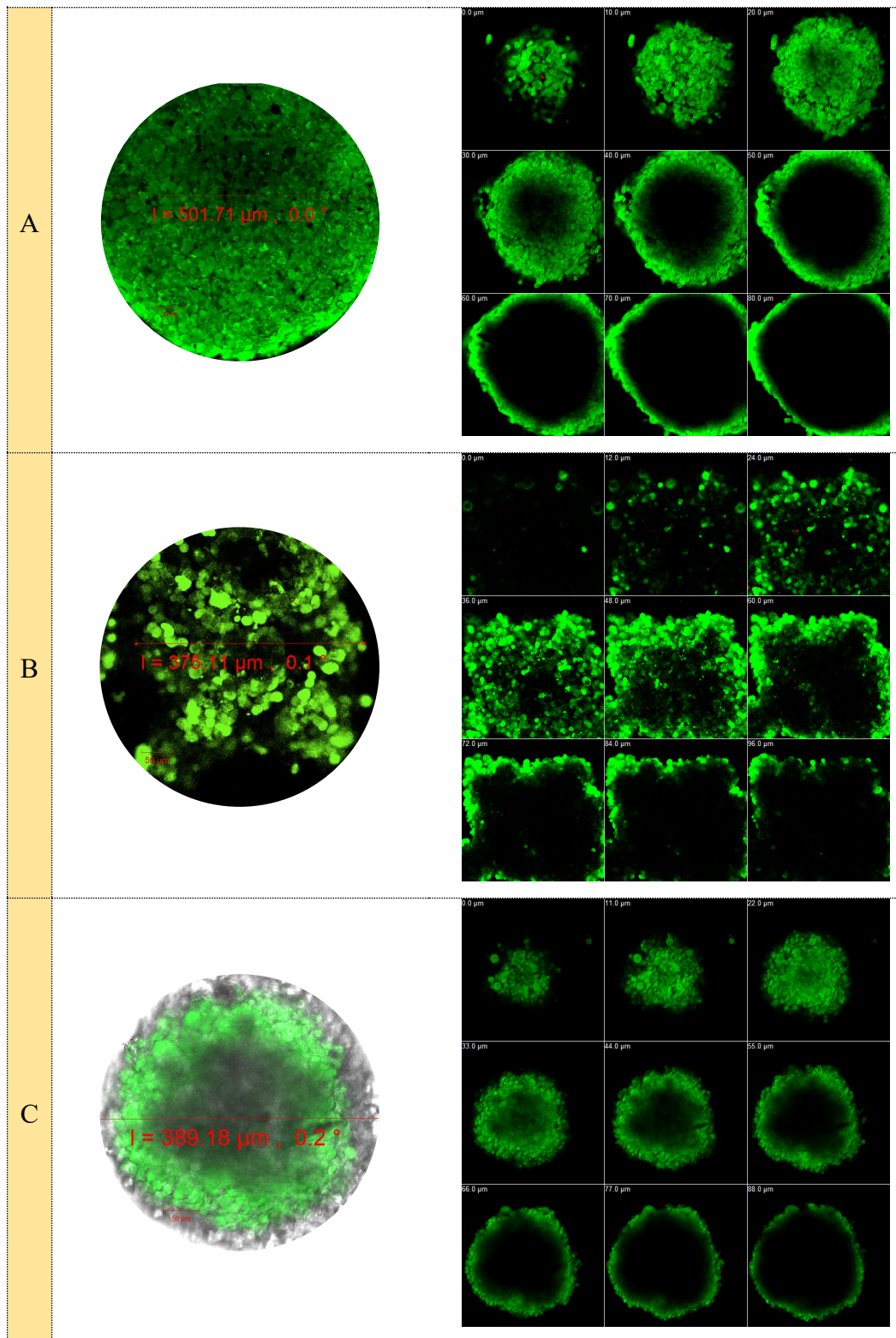


Figure 4.15. The Size and Viability image at different depths of 3D A) MCF-7, B) SKBR-3, and C) MDA-MB-231 by confocal microscopy.

#### 4.2.2.2 Internalization of FITC-DcMNPs on 3D Spheroids

FITC-DcMNPs were prepared by reacting FITC with G5.5 DcMNPs in an EDC/NHS solution. The particles were exposed to 3D MCF-7, MDA-MB-231, and SKBR-3 cells for 24 hours. Due to displaying the targetability of magnetic nanoparticles inside layers of the spheroids, small magnets (3×3mm) were installed on some spheroid of each group (above each drop, outside of the Petri dish).

In all 3D breast cancer cell lines, where imaging analysis was performed, it was found that particle distribution was more homogeneous in spheroids with magnet application and that magnetic nanoparticles could enter into the inner layers of spheroids. However, in spheroids without magnet application, it was observed that the particles had less penetration into the core of spheroids, and their distribution was not homogeneous. Previously (in chapter3), we illustrated the small size of our synthesized DcMNPs, which are suitable for targeting inside the condensed and tough spheroids and tissues. As it is shown in Figures 4.16, 4.17, and 4.18, more green dots were seen inside the spheroids, which are targeted by the magnets.

In the comparative research by Albanese et al., it took 10 minutes for the 40 nm and 70 nm fluorescently labeled PEGylated gold nanoparticles to reach the MDA-MB-435 melanoma cell spheroid's interstitial spaces, and their entry rates were 0.00400 and 0.00396 min<sup>-1</sup>, respectively. In addition, they showed that there was rapid nanoparticle efflux from the MDA-MB-435 spheroid, which indicates that nanoparticle PEGylation inhibits binding to ECM proteins and cells. However, the larger nanoparticles (110 and 150 nm) were kept out from interstitial spaces<sup>97</sup>.



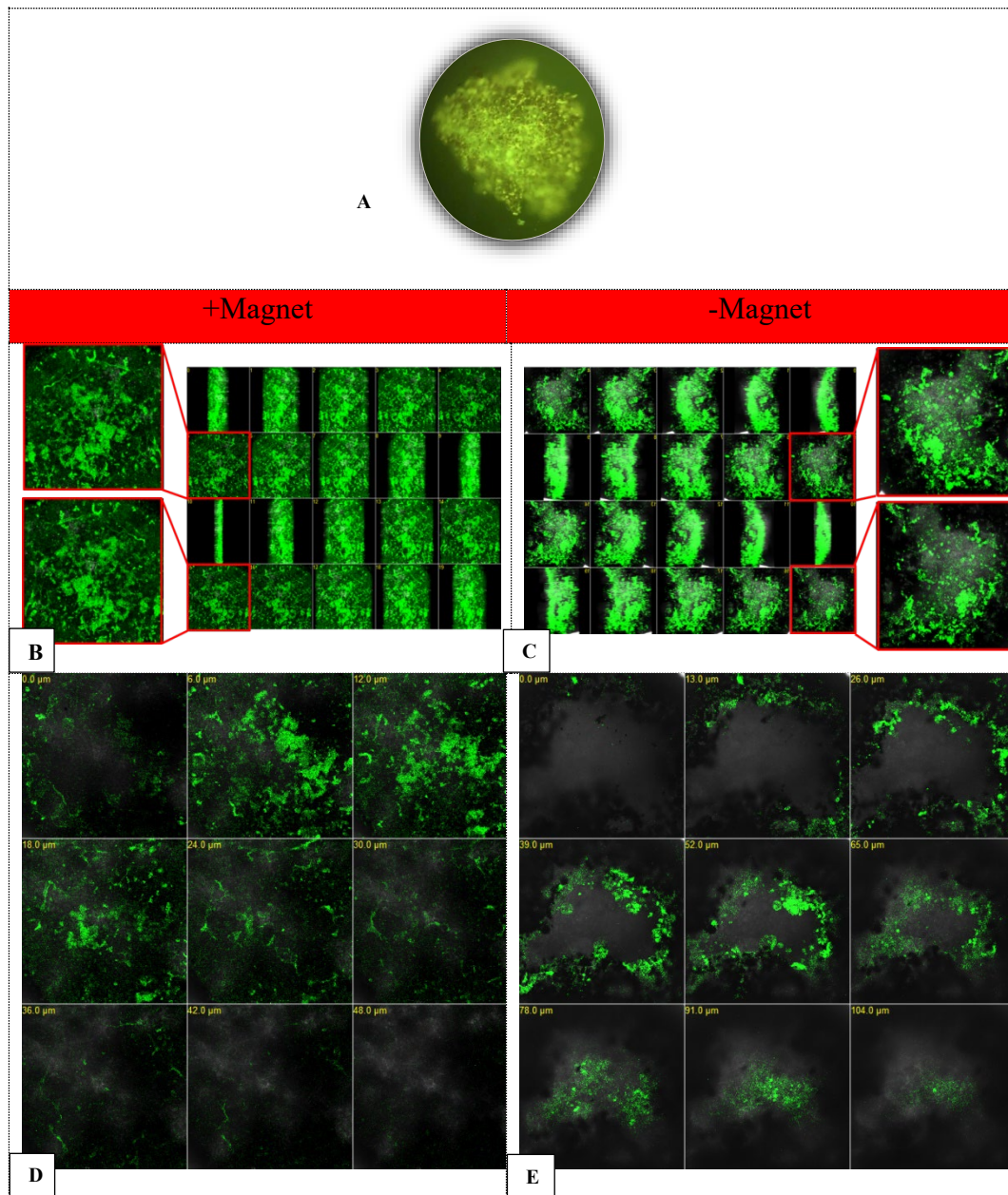


Figure 4.16. Confocal images of internalization of fluorescently labeled DcMNPs into 3D-MCF-7 spheroids after 96 hours. A) Full image of Magnet-applied spheroid, B) X, Y, Z-axis (3D) images of magnet-applied nanoparticle internalization (this image was taken in X and Z directions), C) 3D images of FITC- DcMNPs internalization (without magnet) in X and Z directions., D and E) layer by layer confocal microscopy image of magnet-applied (D) and magnetless MCF-7 spheres after 96h.

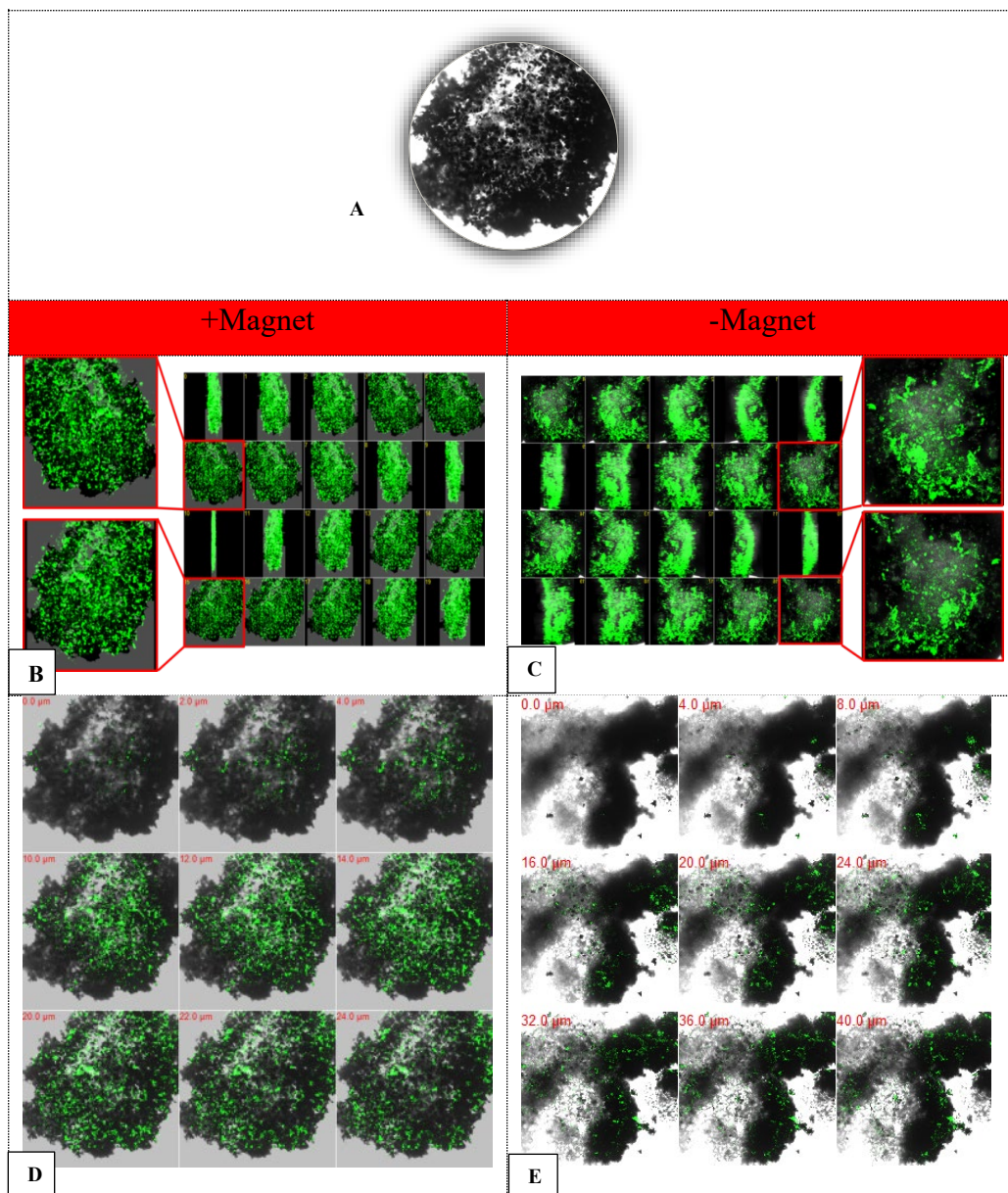


Figure 4.17. Confocal images of internalization of fluorescently labeled DcMNPs into 3D-MDA-MB-231 spheroids after 96 hours. A) Full image of Magnet-applied spheroid, B) X, Y, Z-axis (3D) images of magnet-applied nanoparticle internalization (this image was taken in X and Z directions), C) 3D images of FITC- DcMNPs internalization (without magnet) in X and Z directions., D and E) layer by layer confocal microscopy image of magnet-applied (D) and magnetless MCF-7 spheres after 96h.



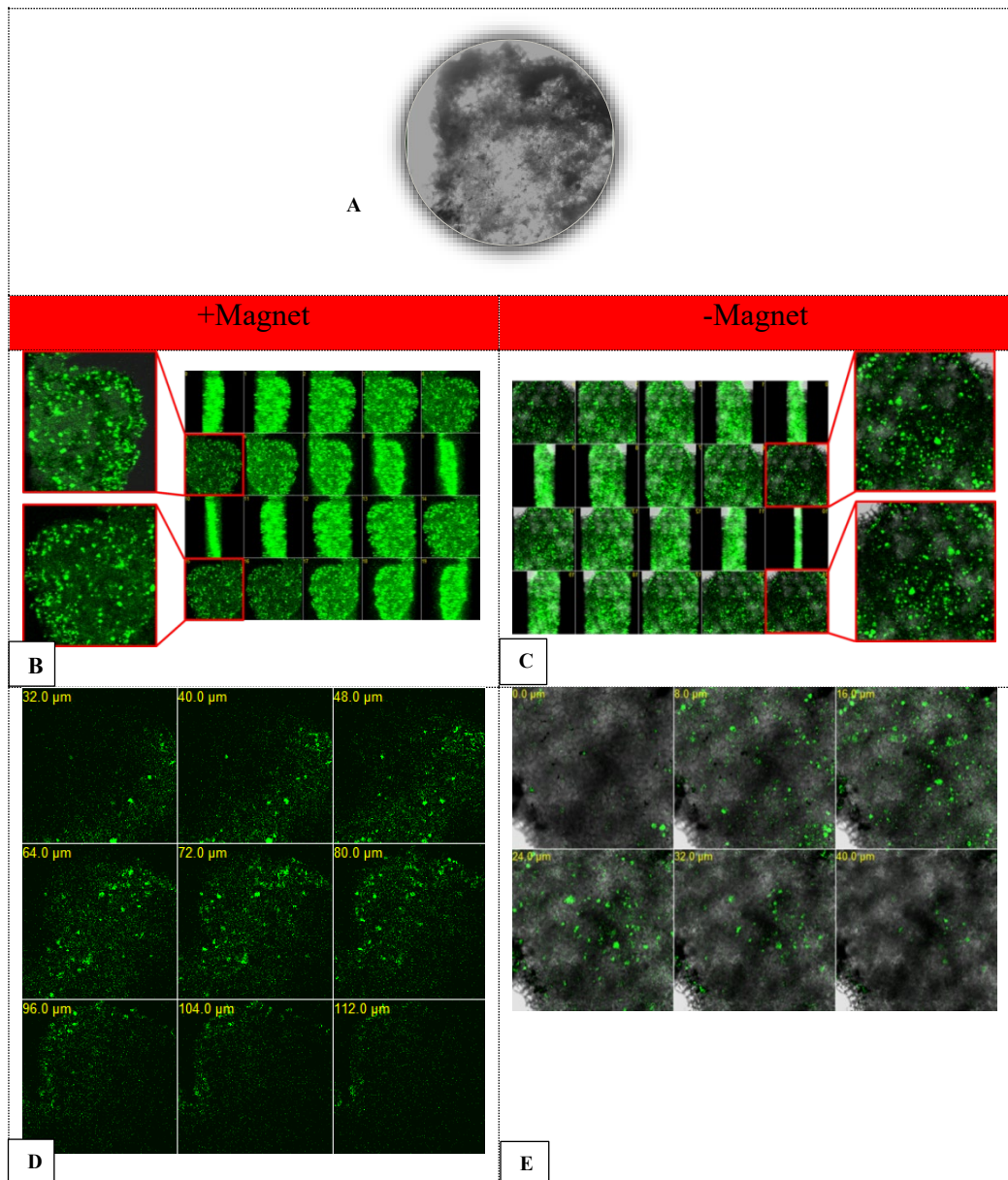


Figure 4.18. Confocal images of internalization of fluorescently labeled DcMNPs into 3D-SKBR-3 spheroids after 96 hours. A) Full image of Magnet-applied spheroid, B) X, Y, Z-axis (3D) images of magnet-applied nanoparticle internalization (this image was taken in X and Z directions), C) 3D images of FITC- DcMNPs internalization (without magnet) in X and Z directions., D and E) layer by layer confocal microscopy image of magnet-applied (D) and magnetless MCF-7 spheres after 96h.

### **4.2.2.3 Anticancer Drug Sensitivity Testing in 3D Cell Cultures**

#### **4.2.2.3.1 Assessment of Viability of Spheroids after Drugs Treatment by Confocal Microscopy**

In order to show the cytotoxicity of the drug treatment, 3D cells (MCF-7, SKBR-3, and MDA-MB-231) were incubated with different doses of Palbociclib and PAL-DcMNPs (2.5, 15, 30, and 50 $\mu$ M) for 96 hours. Spheroids were then stained using live/dead cell dyes (FDA and PI) and monitored by a confocal microscope to observe cell viability on the inner layers of spheroids.

According to the microscopic data, MCF-7 cells started to die in the sphere due to a lower dosage of Palbociclib application. However, at a higher dosage of Palbociclib (50 $\mu$ M), the spheroid disintegrated on the third day of treatment. Treatment with PAL-DcMNPs seems more efficient on 3D MCF-7 cells. As regards Figure 4.19, even lower dosages of PAL-DcMNPs treatments are more effective than Palbociclib treatment at MCF-7 spheroids. In MDA-MB-231 cells, it was determined that the structure of the cell spheres started to deteriorate due to Palbociclib administration, and the spheroids tend to disintegrate. On the other hand, by PAL-DcMNPs treatment, as the structure of 3D MDA-MB-231 was so weak, spheroids disintegrated even at a lower dosage of treatment. For this reason, it was not possible for us to take a confocal microscope image (Figure 4.20).

In 3D SKBR3, outside cells of spheroids began to die, and the sphere structure began to shrink. Similar to MCF-7 spheroids, the PAL-DcMNPs treatments were more operative in SKBR-3 spheroids than Palbociclib treatments (Figure 4.18). Glossy red dots show the uptaking of PI by membrane-permeable dead cells at the outer and inner layers of spheroids.

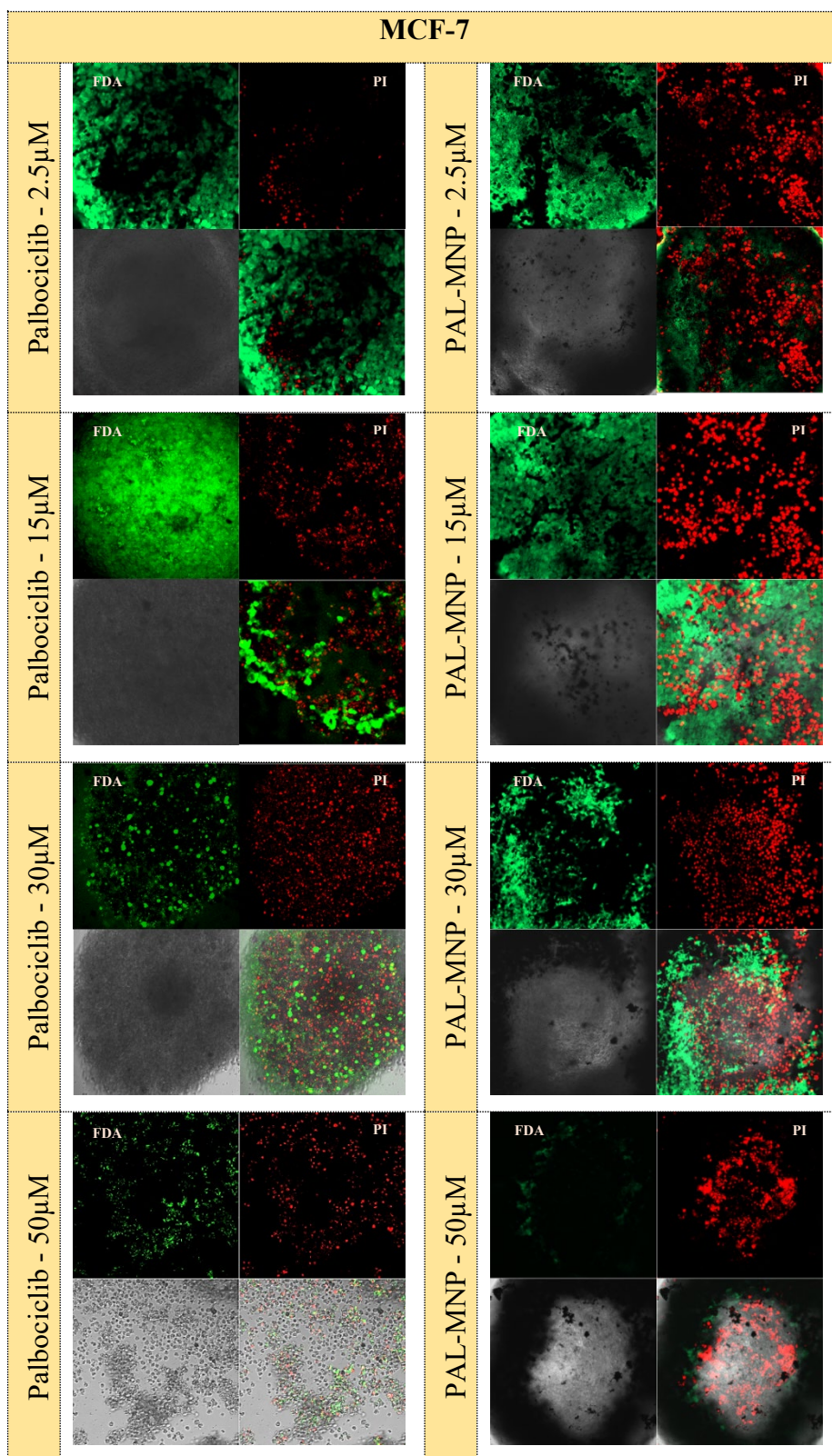


Figure 4.19. Confocal images of Palbociclib and PAL-DcMNPs treated 3D MCF-7 cells stained with FDA and PI.



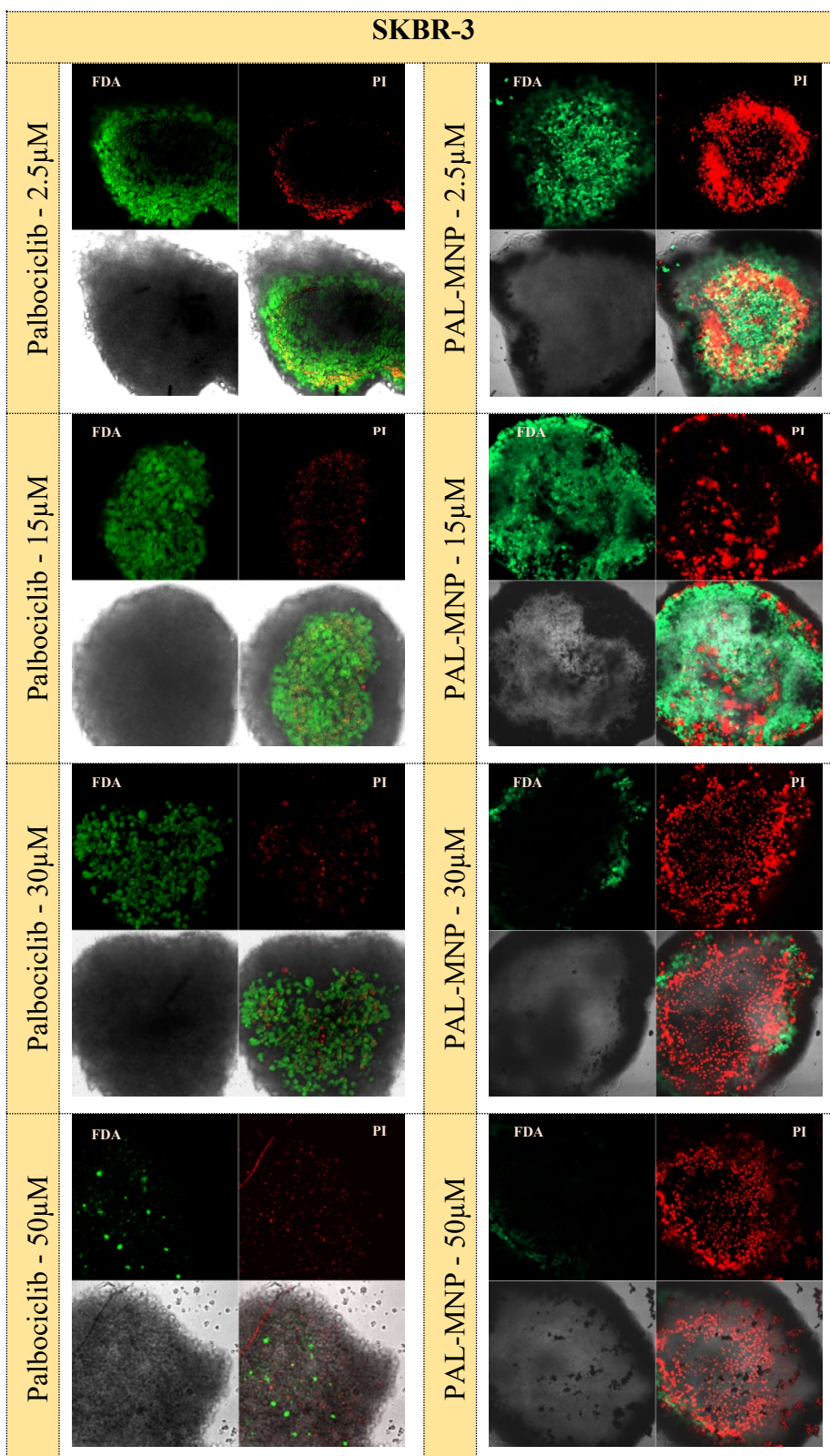


Figure 4.20. Confocal images of Palbociclib and PAL-DcMNPs treated 3D SKBR-3 cells stained with FDA and PI.

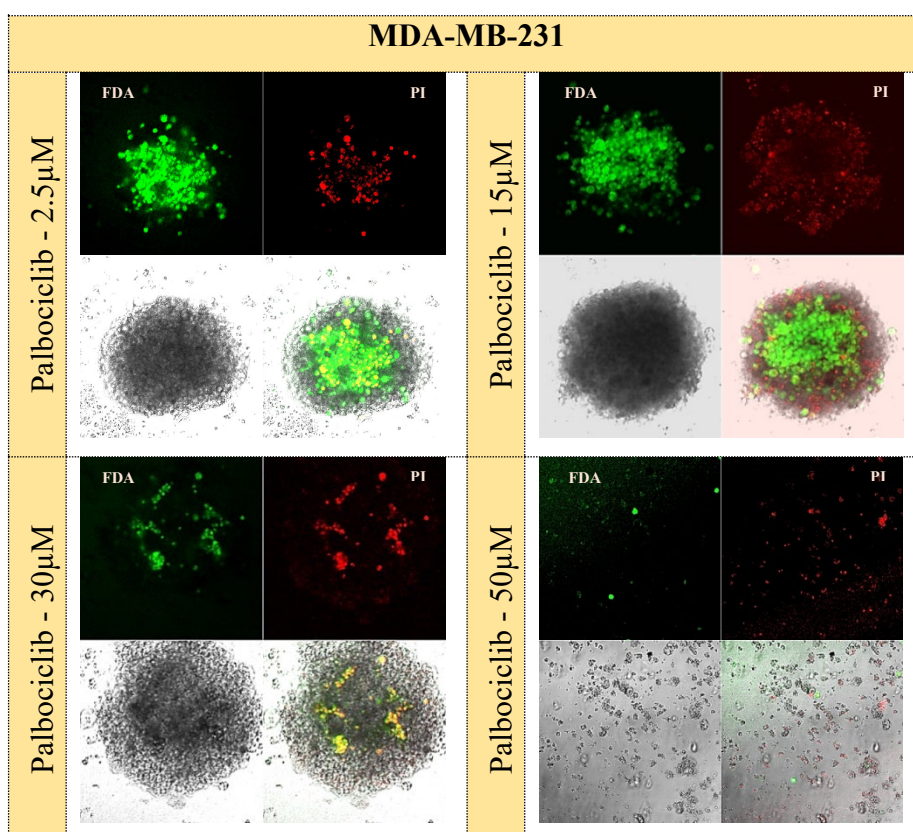


Figure 4.21. Confocal images of control and Palbociclib treated 3D MDA-MB-231 cells stained with FDA and PI.

#### 4.2.2.3.2 Cell Viability Assay

In this study, the CellTiter-Glo® 3D Cell Viability Assay is used to determine the number of viable cells in 3D cell culture. It is carried out by measuring metabolic activity by ATP production after 96 treatments with Palbociclib and PAL-DcMNPs. In a population of exponentially growing cells, an increase in ATP production was associated with higher cell viability. In addition, the viability assay is sensitive enough to detect ATP production from a single mammalian cell.

The cytotoxicity of Palbociclib and PAL-DcMNPs was dose-dependent. Similar to 2D culture, free Palbociclib has a more cytotoxic effect at higher concentrations (30-50 $\mu$ M) on 3D MCF-7, MDA-MB-231, and SKBR-3 breast cancer cell lines. Despite this, it has been observed that for all breast cancer cell lines, drug doses of Palbociclib conjugated DcMNPs can inhibit 50% of the cell viability with even

lower drug concentrations than free Palbociclib. These results show that conjugation of Palbociclib with DcMNPs improved the cytotoxic effect in lower drug concentrations. The observed effects were more evident for 3D MCF-7 cells than for 3D MDA-MB-231 and 3D SKBR3 cells.

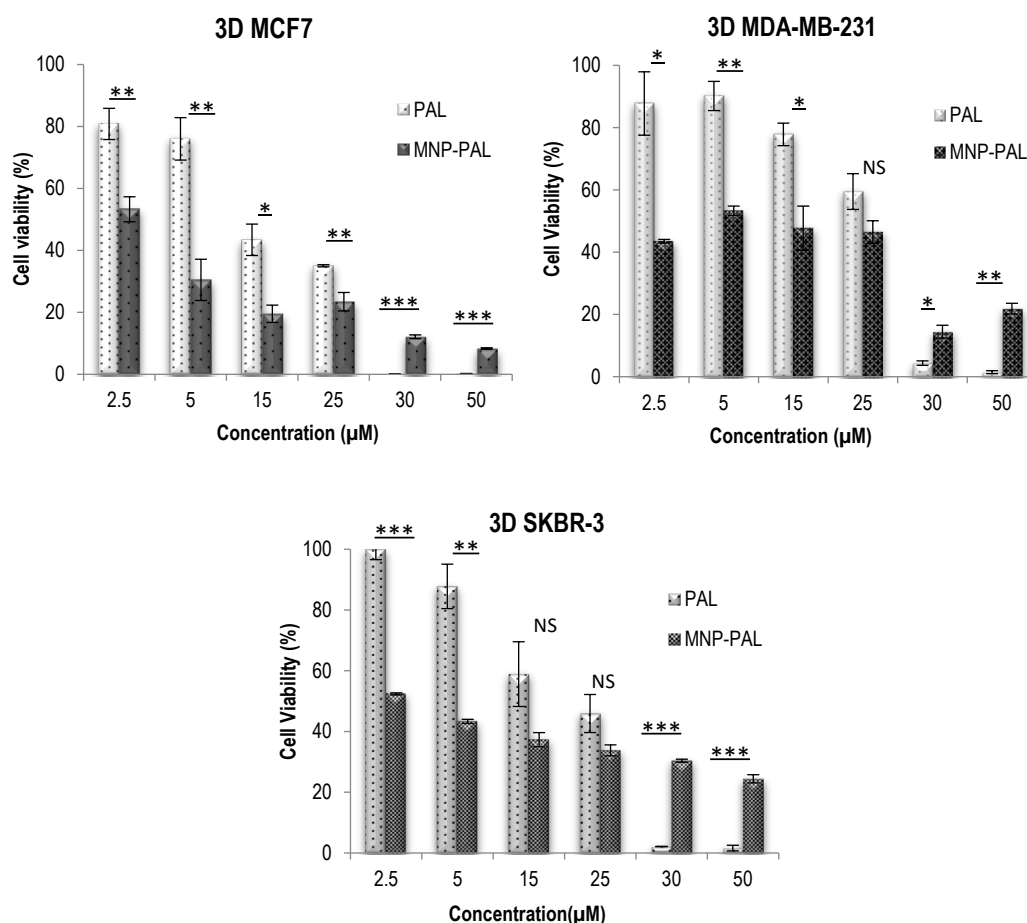


Figure 4.22. CellTiter-Glo® 3D Cell Viability Assay (A) MCF-7, (B) MDA-MB-231, and (C) SKBR-3 cell lines. Results are the mean  $\pm$ SEM (n=3). This difference was statistically significant when tested with a student t-test (\*p<0.05, \*\*p<0.01, \*\*\*p<0.001).

#### 4.2.2.3.3 LDH Assay

Lactate dehydrogenase (LDH) release level into the media is a marker of membrane integrity<sup>98</sup>. Palbociclib and PAL-DcMNPs caused a dose-dependent



release of LDH to the medium of 3D cell culture in MCF-7, MDA-MB-231, and SKBR-3 cell lines, indicating disruption of cell membrane structure. Measurements were made at 24, 48, 72, and 96 hours of incubation.

The responses of all cell lines to the increasing concentration of Palbociclib and PAL-DcMNPs are shown in Figure 4.23. The results showed the rising release of LDH due to the treatment of PAL-DcMNPs after 96 hours.

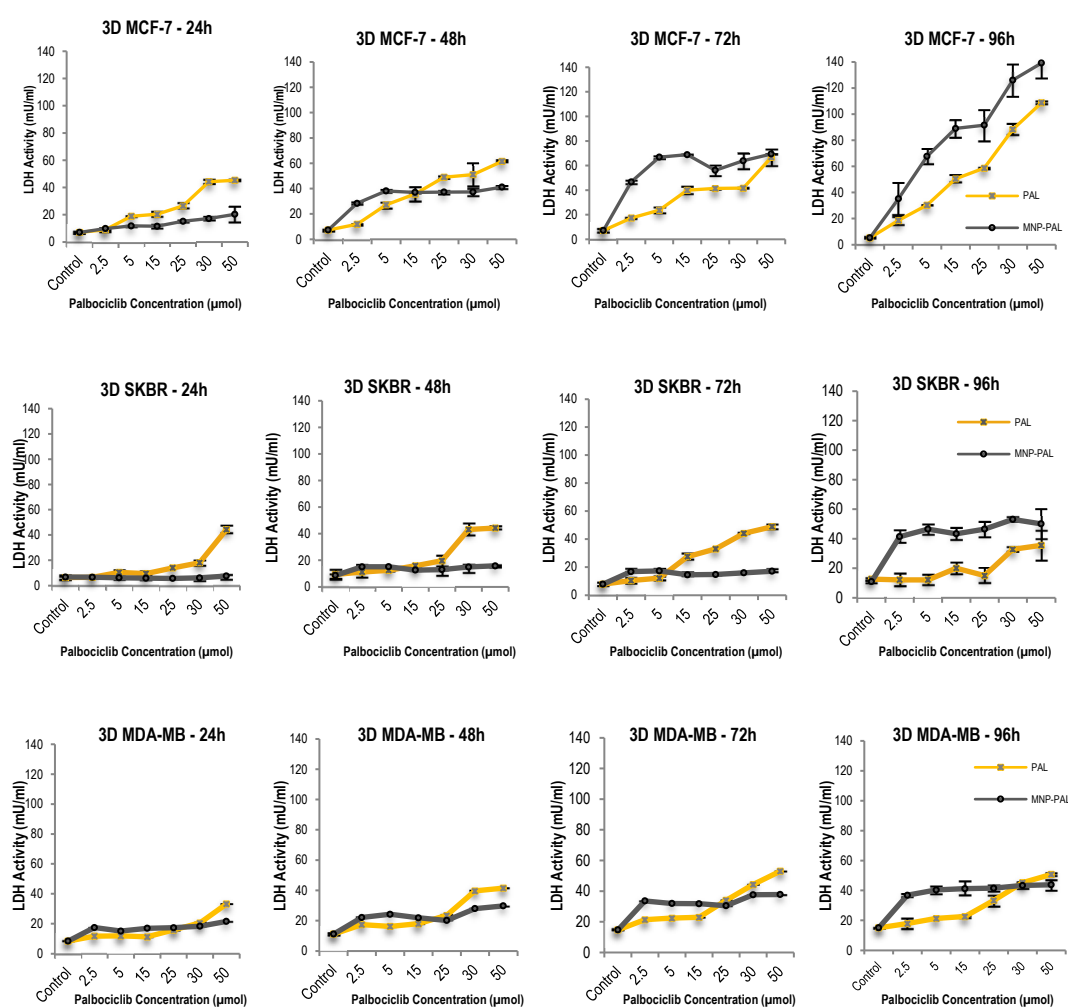


Figure 4.23. LDH activity of 3D (A) MCF-7, (B) SKBR-3, (C) MDA-MB-231

#### 4.2.2.4 RT-PCR Results

To elucidate the difference in apoptotic status between the untreated control group and Palbociclib and PAL-DcMNPs (15 $\mu$ M) treated 3D breast cancer cells, the expression pattern of the genes related to apoptosis (Bax, Bcl-2), invasion, and metastasis (IL6), and tumor suppression (BRCA1) were examined by qRT-PCR.

Interleukin (IL)-6 plays a crucial role in breast cancer's progression, invasion, and metastasis. In addition, a variety of inflammatory cytokines, including tumor necrosis factor (TNF)- $\alpha$ , interleukin (IL)-1 $\beta$ , and IL-6, are associated with chronic inflammation of the tumor microenvironment, thereby promoting tumor progression and metastasis. Breast cancer patients have much higher plasma levels of IL-6 than healthy donors, which correlates with frequent metastases and poor survival<sup>99</sup>.

The results of this study revealed that IL-6 gene expression level was significantly decreased in MCF-7 and slightly in MDA-MB-231 and SKBR-3 Palbociclib treated 3D culture groups. However, PAL-DcMNPs treatment impacts the metastatic potential of the MDA-MB-231 spheroids.

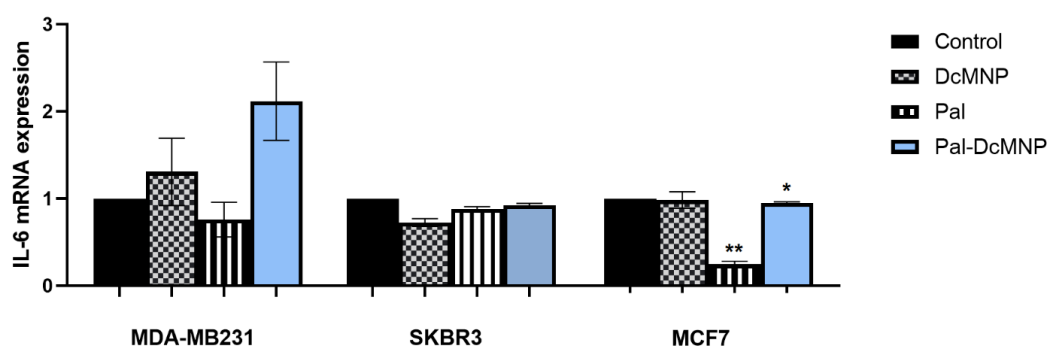


Figure 4.24. Expression levels of IL6 genes in untreated and treated MDA-MB-231, SKBR3, and MCF7 cell lines with 15 $\mu$ M Palbociclib, bare G5.5 PAMAM DcMNPs, and PAL-DcMNPs for 96h, when  $p < 0.05$ .

It is believed that IL-8 contributes to multiple hallmarks of cancer, such as increased proliferation, angiogenesis, invasion, and metastasis, in a wide range of solid tumors, including prostate, gastric, bladder, ovarian, lung, and melanoma. Breast cancer cells produce more interleukin-8 (IL-8) than normal breast tissue, which is associated with worse outcomes. In HER2-positive cancers, IL-8 promotes cancer progression by increasing cell invasion, angiogenesis, and metastasis<sup>100</sup>.

It was shown that IL-8 gene expression level was significantly decreased in MDA-MB-231, MCF-7, and SKBR-3 tumor groups treated with PAL-DcMNPs and Palbociclib treated group. Despite the increase in IL-6 gene expression in MDA-MB-231 tumor tissues treated with PAL-DcMNPs, IL-8 was significantly decreased, indicating that tumor growth can be suppressed in this way.

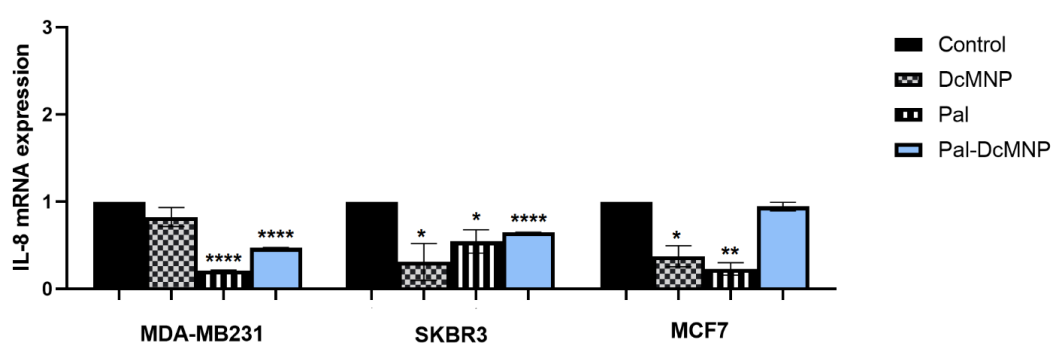


Figure 4.25. Expression levels of IL8 genes in untreated and treated MDA-MB-231, SKBR3, and MCF7 cell lines with 15 $\mu$ M Palbociclib, bare G5.5 PAMAM DcMNPs, and PAL-DcMNPs for 96h, when  $p < 0.05$ .

Apoptosis is triggered and inhibited by two cytoplasmic proteins, B-cell lymphoma protein 2 (Bcl-2)-associated X (Bax) and Bcl-2. Therefore, cells with a higher Bax/Bcl-2 ratio will be more sensitive to a given apoptotic stimulus than those with a lower Bax/Bcl-2 ratio. According to Figure 4.26, In all three cell lines, MDA-MB-231, SKBR3, and MCF7, the Bax/Bcl-2 ratio increased in response to PAL-DcMNPs stimulation. These findings might be related to decreased viability after

PAL-DcMNP treatment, which validates our result in the cell viability test and LDH release amount. However, the increased ratio, similar to the 2D culture results, was significantly more at MDA-MB-231 3D cells than in two other groups.

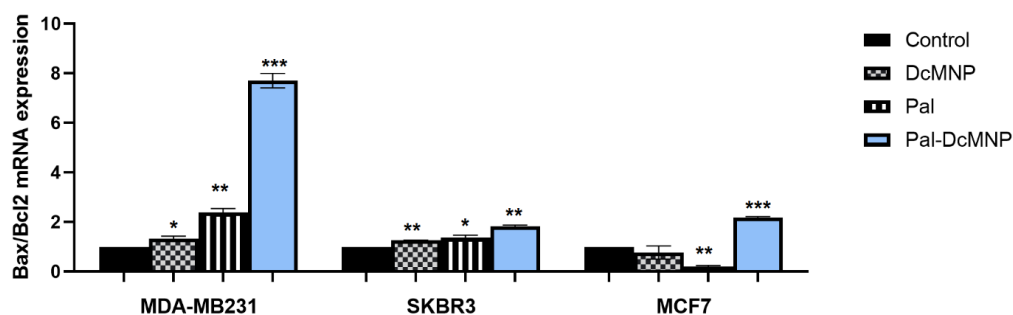


Figure 4.26. Bax/Bcl-2 gene expression ratios in untreated and treated MDA-MB-231, SKBR3, and MCF7 cell lines with 15 $\mu$ M Palbociclib, bare G5.5 PAMAM DcMNPs, and PAL-DcMNPs for 96h, when  $p < 0.05$ .

Approximately 5% of unselected breast cancer patients carry the breast cancer susceptibility gene 1 (BRCA1). BRCA1 encodes a 220 kD nuclear protein and has been linked to breast cancer susceptibility. A variety of functions are controlled by BRCA1, including DNA repair, replication fork protection, cell cycle regulation, and gene transcription<sup>101</sup>. No difference was observed in BRCA1 in spheroids after treatment by Palbociclib compared to the control.

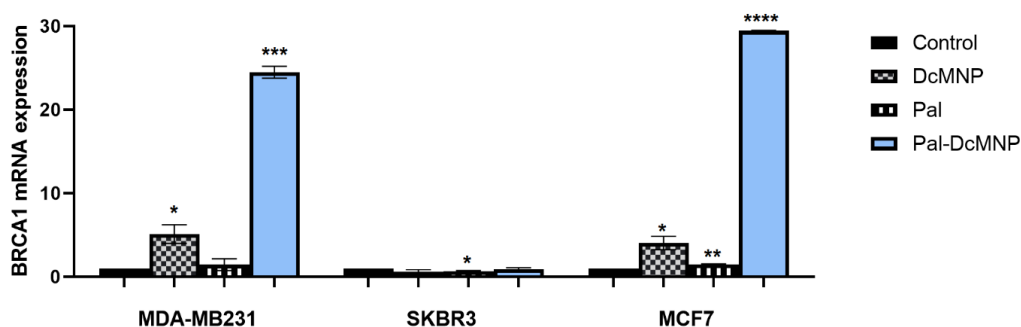


Figure 4.27. Expression levels of BRCA1 genes in untreated and treated MDA-MB-231, SKBR3, and MCF7 cell lines with 15 $\mu$ M Palbociclib, bare G5.5 PAMAM DcMNPs, and PAL-DcMNPs for 96h, when  $p < 0.05$ .

### 4.2.3 Ex-vivo Culture Results

#### 4.2.3.1 Internalization of FITC-DcMNPs in Micro-dissected Tissues

Figure 4.28 shows the confocal microscopy images obtained after culturing the SKBR-3 tumor slices with  $\sim 2$  mg/ml of FITC labeled magnetic PAMAM dendrimers for 24 hours. For comparison purposes, four micro-dissected slices and two separate microfluidic chips with and without installed magnets were used. The obtained images show the differences between targeted and nontargeted magnetic nanoparticles inside tissue slices.

According to the results, all tumor slices were able to internalize the FITC-DcMNPs. Also, it is clear that the internalization rate tended to increase at magnet-targeted slices. Six images from different parts of two slices in magnet-targeted tissues showed around 90-110  $\mu\text{m}$  internalization of nanoparticles inside layers (Figure 4.28, C and D). However, it is only the internalization rate for the first 24 hours. The intensity of fluorescent green light in deeper layers could be visible after deconvolution, which increases the object signal and correct the noises. Afterward, analysis of 3D data by maximum intensity projections (MIP) projects the visualization of voxels with maximum intensity inside the layers of the tissues. In Figure 4.22, C green signals from the FITC-DcMNPs are clearly seen at 100  $\mu\text{m}$  intervals. However, in non-targeted slices, the nanoparticle's internalization rate is around 50  $\mu\text{m}$  (Figure 4.28, E and H). Another critical difference between nanoparticle targeted and non-targeted slices seems to be consonant dispersion of DcMNPs in the targeted slices and partly aggregation in non-targeted slices (Figure 4.22, B and G).

Previously in this chapter, we mentioned the cellular uptake of magnetic nanoparticles in 2D standard culture and 3D hanging drop culture methods. Confocal microscopy images from 2D cells indicated the presence of nanoparticles inside the cells. DcMNPs are dispersed in the cytoplasm but especially around the

nucleus. Although similar to micro-dissected slices, in 3D cultures, nanoparticles' dispersion and internalization rate are higher in magnet-targeted spheroids than in non-targeted ones.

In similar studies in the literature, Albanese et al. investigated the flow of medium in a microfluidic system affected the accumulation and penetration of nanoparticles inside the spheroids. However, the flow rate does not so much affect nanoparticles' average penetration depth inside the spheroids' layers<sup>97</sup>. Also, in-vivo studies on an MDA-MB-435 tumor model by this group demonstrated the 160 nm nanoparticles did not penetrate into the tissue surrounding tumor vasculature. This agrees with tumor-on-a-chip studies data by this group, which indicated nanoparticles larger than 100 nm did not penetrate into spheroid tissues. In contrast, the results of smaller nanoparticles (50 nm) showed the increased accumulation of nanoparticles in the tumor blood vessels and more penetration to spheroids in the tumor-on-a-chip system. In addition, this group's in vitro findings showed the number of nanoparticles at the spheroid in the microfluidic system interface reflected total tissue accumulation<sup>97</sup>.

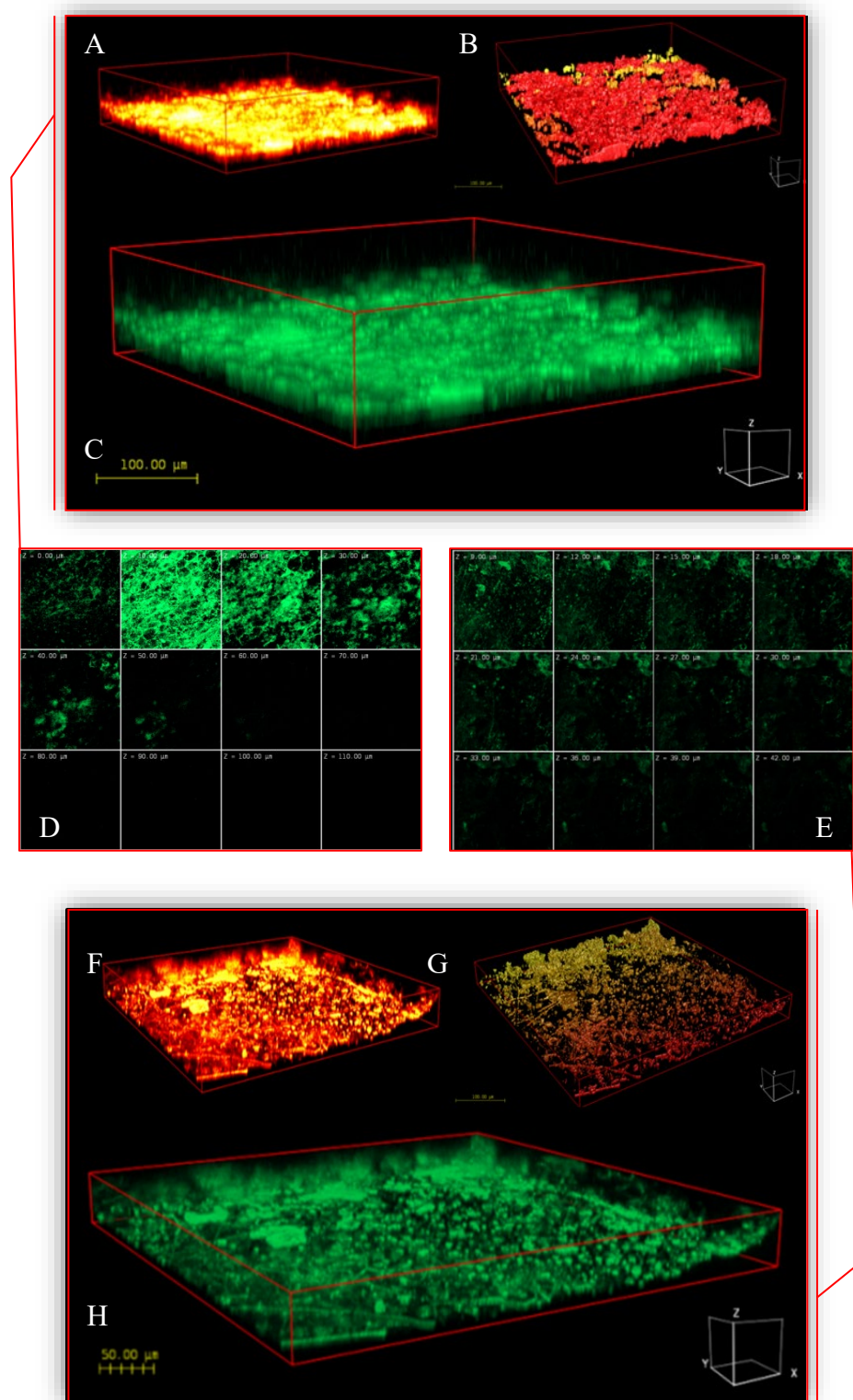


Figure 4.28. Confocal microscope images of FITC-DcMNPs internalization in microdissected slices in the microfluidic system after 24 hours. A, B, heatmap, C, maximum intensity projection and D, layer by layer images of magnet targeted SKBR-3 slices. F, G, heatmap, H, maximum intensity projection and E, layer by layer images of non-targeted SKBR-3 slices (Huygens Essential software).

#### **4.2.3.2 Anticancer Drug Sensitivity Testing in Ex-vivo Cultures**

The viability of the tumor tissue samples was evaluated by confocal microscopy, lactate dehydrogenase (LDH) release, and glucose consumption analysis. FDA has been used for the viability assessment of a wide variety of cells and tissue types. The FDA assay does not have any significant toxicity, making this assay suitable for cell and tissue culture analysis. FDA is not a fluorescent molecule and remains colorless until esterases convert it to fluorescein inside the metabolically active cells. Under the light of confocal microscopy, the intensity of fluorescence was seen; it gave the proportion of live cells in the layers of tissue<sup>102</sup>. LDH is a cytoplasmic enzyme constitutively expressed in most mammalian cells. Determining the amount of LDH released into the medium is widely used to assess plasma membrane integrity. Excessive release of LDH enzyme into the medium indicates that the cells are dead, while the consumption of glucose from the medium shows that the cells are alive. In order to determine the micro slice viability in the microfluidic chip in control and drug-treated groups, leakage of LDH and glucose consumption amount were measured every 24 hours for 96 hours.

##### **4.2.3.2.1 Assessment of Viability of Micro-dissected slices after Palbociclib and PAL-DcMNPs Treatment by Confocal Microscopy**

In chapter 2, section 2.3.2, we showed the confocal microscopy data of SKBR-3 and MDA-MB-231 tumor slices on the first day, immediately after segmentation, and after 4 days of cultivation on microfluidic systems. The layer-by-layer images and Maximum Intensity Projection (MIP) of these non-treated tumor slices showed the viability of slices for up to 96 hours. However, as seen in Figure 4.29, images' average red fluorescence intensities were increased after treatment with Palbociclib and PAL-DcMNPs. In both groups of micro-dissected slices, the intensity of live cells decreases by more than 50% after treatment by Palbociclib. In SKBR-3



images, the intensity of dead cells increased considerably after treatment with palbociclib and PAL-DcMNPs. Palbociclib-treated MDA-MB-231 slices showed over three folds increase in dead cells with respect to the control group after 96h. Due to the limited number of pieces, PAL-DcMNPs treatment couldn't be performed for MDA-MB-231 tissues.

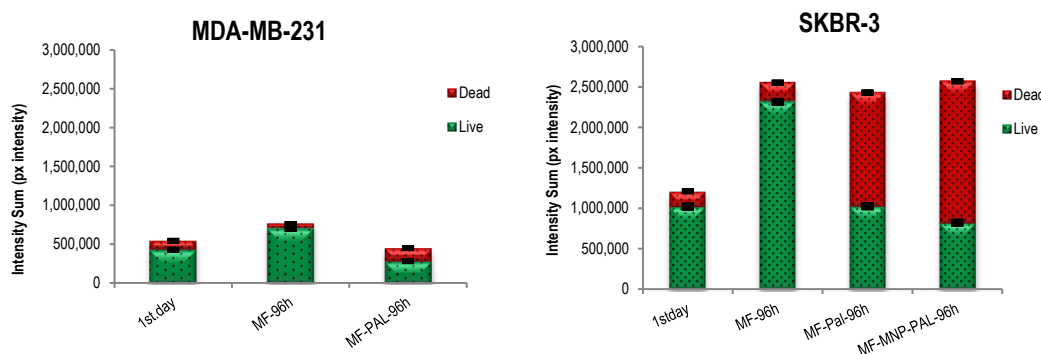


Figure 4.29. The mean sum intensities of MDA-MB-231 (A) and SKBR-3 (B) tumors from three different positions of two slices of micro-dissected tissues (slice number: n = 2, image number: n = 6). The sum intensity for live and dead images is calculated by the MIPAR program for each layer-by-layer image. The average sum intensities show differences between the first and fourth days and after Palbociclib and PAL-DcMNPs treatments.

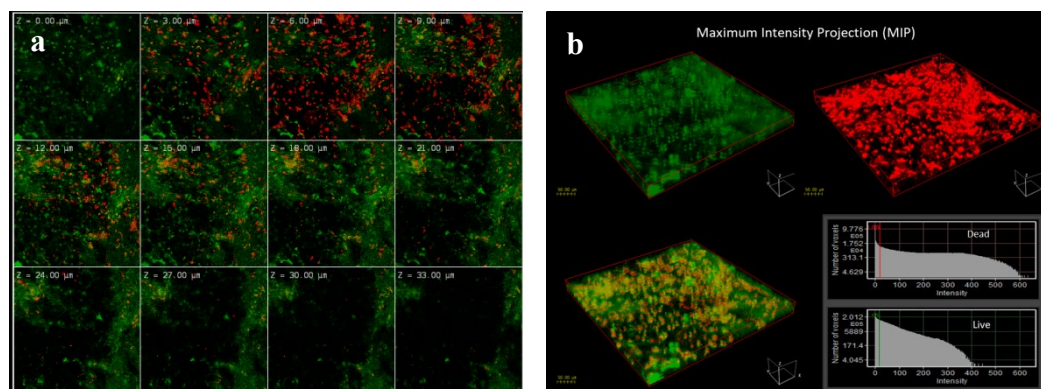


Figure 4.30. Confocal imaging and maximum intensity projection of MDA-MB-231 micro-dissected tissues. Layer-by-layer images indicated the differences between the amount of live and dead cells in micro-dissected tissues after 96h treatment by Palbociclib (a) and (b) Live and dead maximum intensity projections from a representative MDA-MB-231 slice of confocal image stacks after 96 h Palbociclib treatment from the microfluidic system (by Huygens Essential software). \* First and fourth days control group images showed in chapter 2.

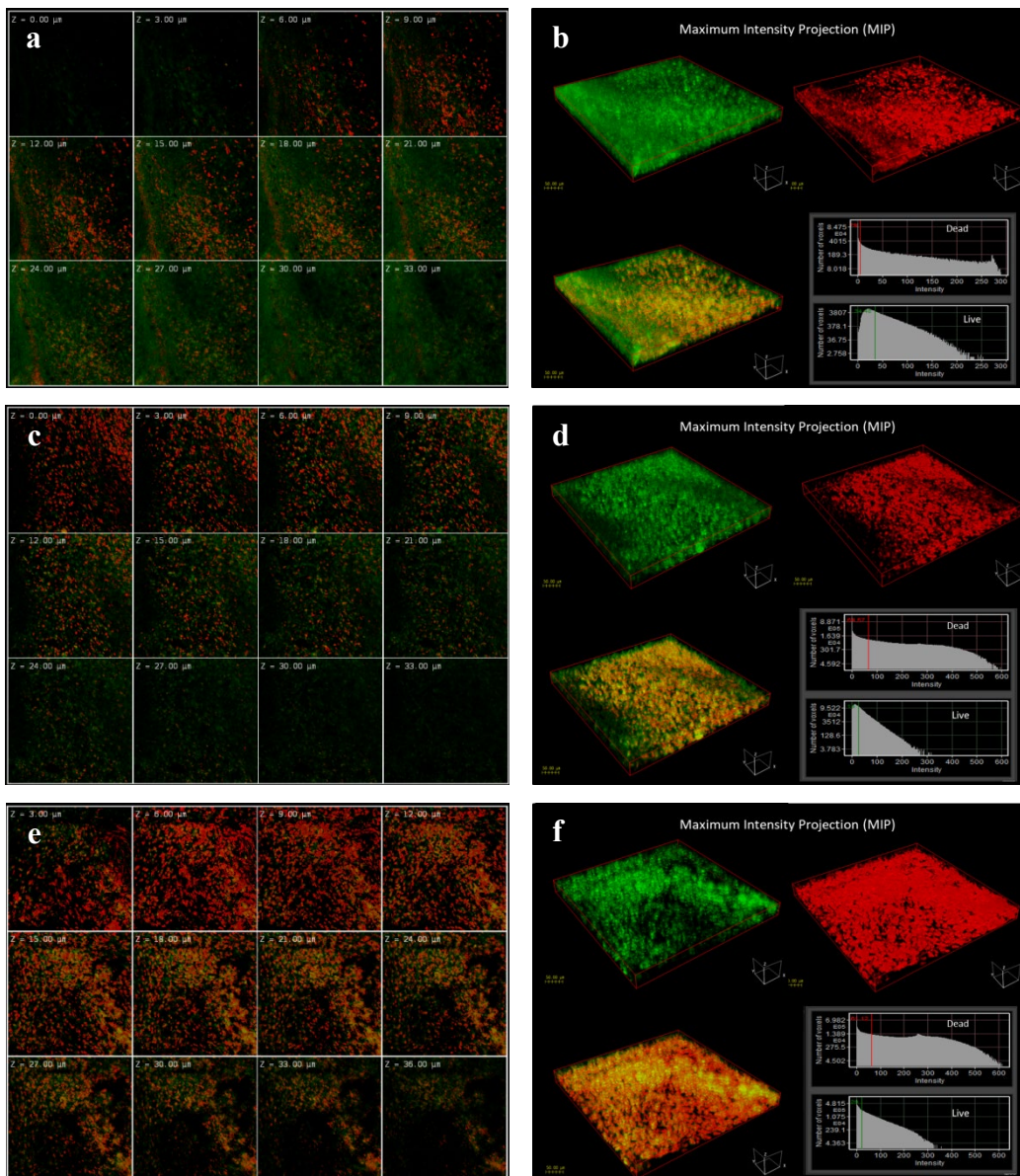


Figure 4.31. Confocal imaging and maximum intensity projection of SKBR-3 micro-dissected tissues. Layer-by-layer images indicated the differences between the amount of live and dead cells in micro-dissected tissues after 4 days of cultivation at the microfluidic chip. Control (non-treated) (a) and (b), after 96 h Palbociclib treatment(c) and (d), after 96h PAL-DcMNPs treatment (e) and (f) . Live and dead maximum intensity projections from a representative SKBR-3 slice of confocal image stacks after 96 h from the control, PAL, and PAL-DcMNPs treated slices at microfluidic systems (by Huygens Essential software) (b), (d), and (f).

#### 4.2.3.2.2 LDH Assay

In Chapter 2, we demonstrated that untreated micro-dissected tumor slices (control group) could survive for 96 hours in the microchannel system<sup>102</sup>. Afterward, LDH release analyzes were performed to determine the effects of Palbociclib and Palbociclib conjugated DcMNPs (PAL-DcMNPs), Doxorubicin, and Doxorubicin loaded DcMNPs (Dox-DcMNPs) on tissue samples. The media from the microfluidic system were collected at 24, 48, 72, and 96 hours. Another purpose of our microfluidic channel system, in addition to tissue viability tests, is to target our magnetic nanoparticles to tissue samples and to compare the effects of drug conjugated nanoparticles on the tissue with free drugs.

In all groups, as expected, an increase in the amount of LDH release was observed in the first 24 hours due to tissue damage because of microsection<sup>103</sup>. However, when the data at the end of 96 hours are examined, it is remarkable that there was more LDH release from tumor tissues to which Palbociclib and PAL-DcMNP were applied compared to control tissues in all groups. At 96 hours, PAL-DcMNPs were shown to be more effective than free Palbociclib in all groups. These results suggest that DcMNPs may have penetrated the tissue for 96 hours and started showing their effects after that. Palbociclib-loaded DcMNPs have the ability to release drugs in a controlled manner due to the destruction of DcMNPs in endosomes, which are acidic environments, after penetrating into the tissue and entering the cells. Previously, Yabbarov et al. have shown that pH-dependent linkers hydrolysis in an acidic environment<sup>67-104</sup>.

The Palbociclib conjugation method is stable in the extracellular medium due to the pH-dependent linker used to conjugate PAMAM dendrimer to Palbociclib. An absorptive endocytosis mechanism transports the carboxyl-terminal dendrimer to the cell. A lysosome's acidic environment releases the drug. We saw an increase in LDH release between 48 hours and 96 hours in all groups because the controlled release of the drug from PAL-DcMNPs caused an increase in cell death (Figures 4.32 and 4.33).

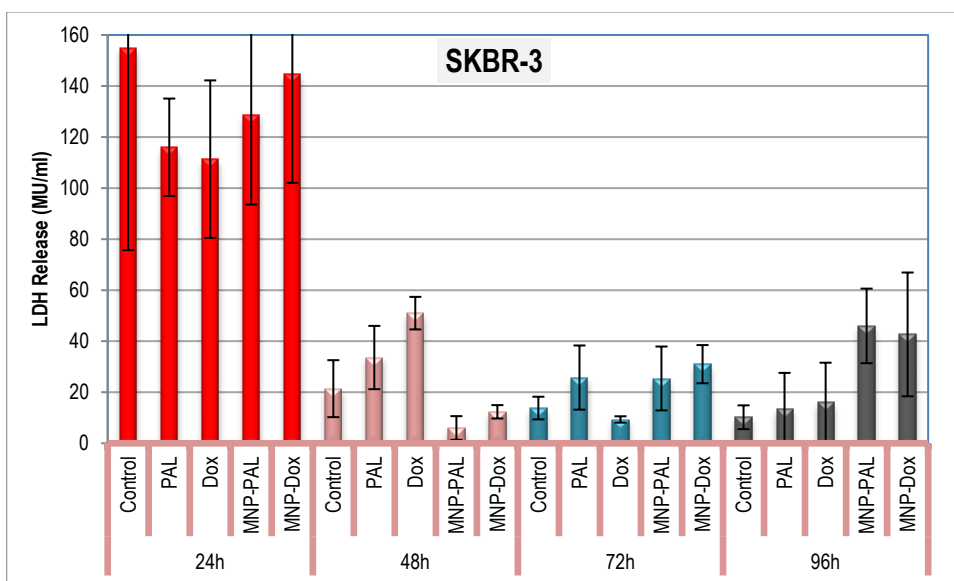


Figure 4.32. LDH release after administration of Palbociclib, Palbociclib-conjugated DcMNPs (MNP-PAL), Doxorubicin, and Doxorubicin-loaded DcMNPs (MNP-Dox) from tumor sections formed with SKBR-3 cells (n=5).

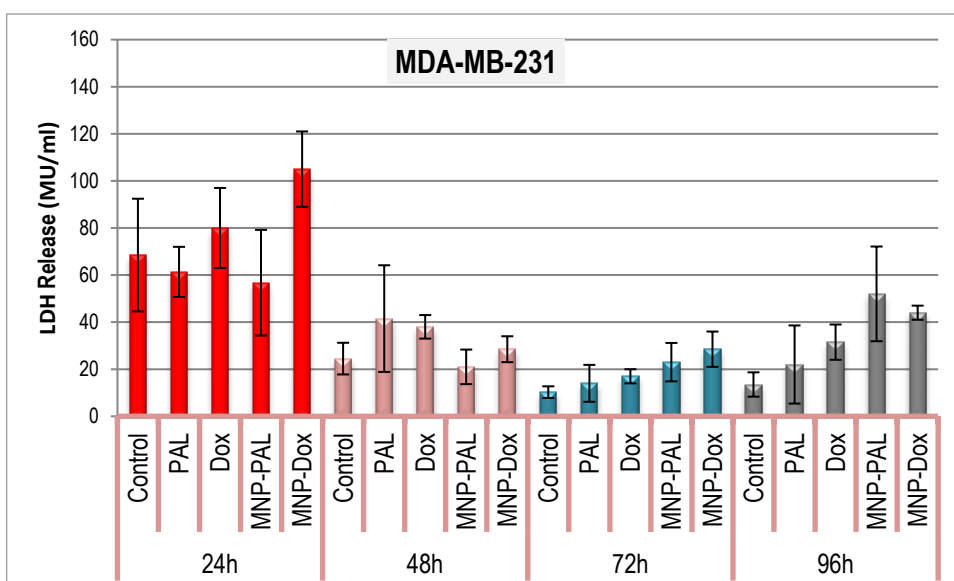


Figure 4.33. LDH release after administration of Palbociclib, Palbociclib-conjugated DcMNPs (MNP-PAL), Doxorubicin, and Doxorubicin-loaded DcMNPs (MNP-Dox) from tumor sections formed with MDA-MB-231 cells (n=4).

In the MCF-7 group, although DcMNPs loaded with Palbociclib at 48, 72, and 96 hours appeared to be more effective than Palbociclib, a statistical analysis could not be performed because the number of samples was 1 (Appendix B).

#### **4.2.3.2.3 Metabolic Activity**

Glucose levels were measured at every 24h (Figure 4.34) after treatment with Palbociclib, PAL-DcMNPs, Doxorubicin, and Dox-DcMNPs for 96h. As mentioned in Chapter 2, in contrast to LDH release, the glucose consumption of the control group in the microfluidic chip increases during four days, which shows the groups are alive inside the micro-chamber for 96h.

In MDA-MB-231 micro-dissected tissues from four mice, significant decreases in glucose consumption could be seen in Palbociclib and PAL-DcMNPs groups during four days of treatment. Also, the daily comparison of both MDA-MB-231 and SKBR-3 drug-treated groups by the control group of that day displayed an apparent decrease in glucose consumption after drug treatment.

It is possible to have fluctuating error rates due to minor differences between micro-dissected tumor slices (350  $\mu$ M) size or because of metabolic differences between the limited number of mice groups (n=4 in MDA-MB-231 and n=5 in SKBR3).

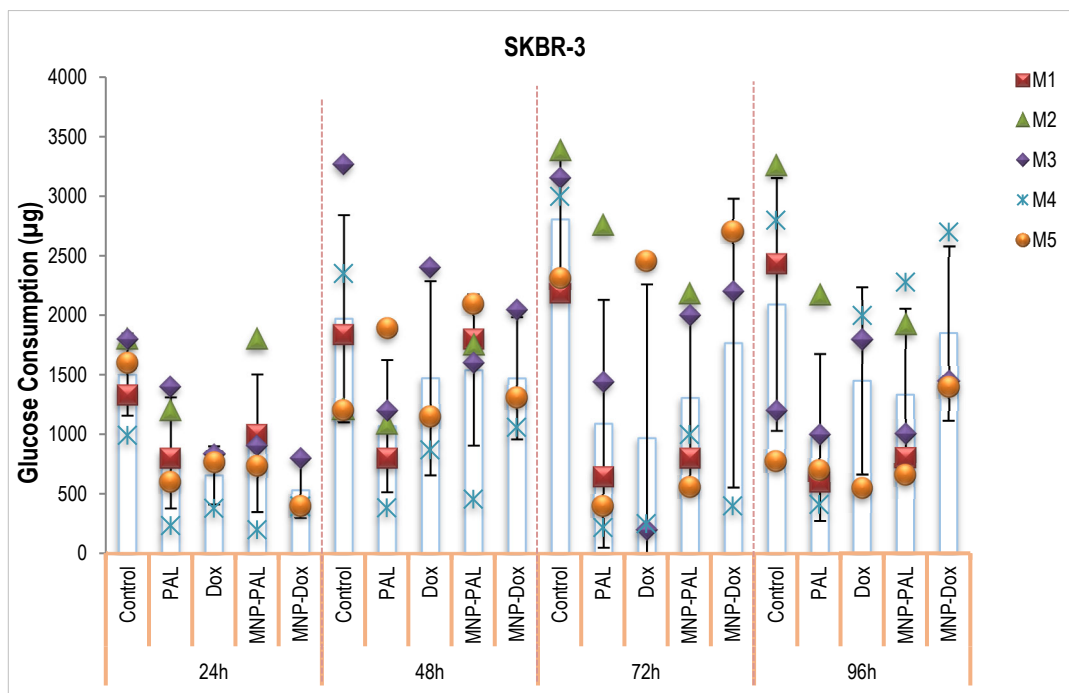
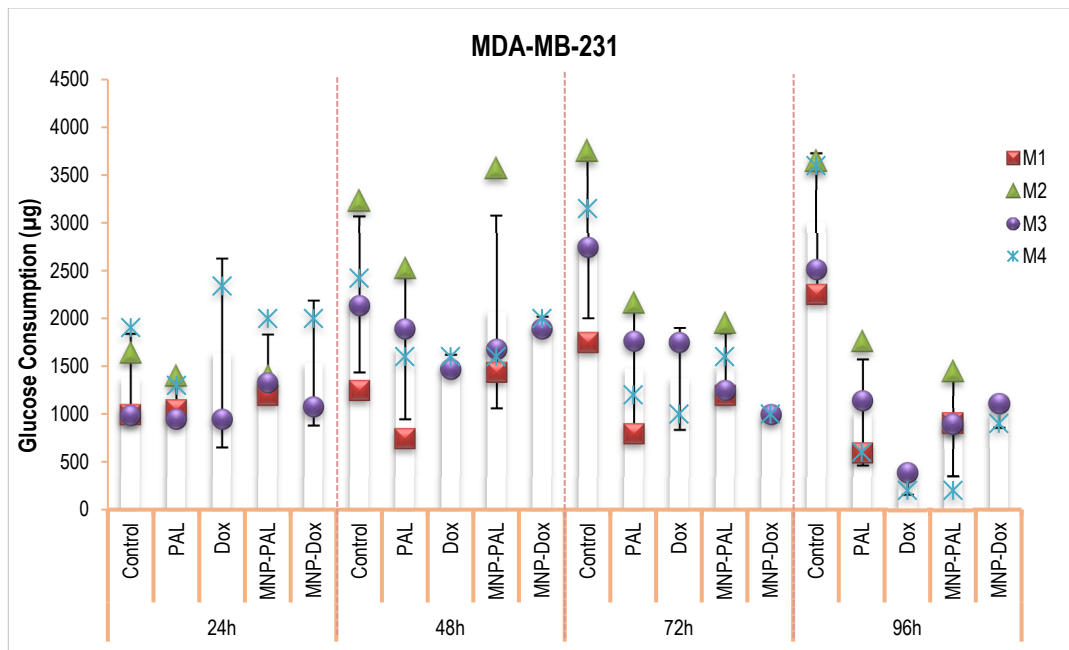


Figure 4.34. Glucose consumption after administration of Palbociclib, Palbociclib-conjugated DcMNPs (MNP-PAL), Doxorubicin, and Doxorubicin loaded DcMNPs (MNP-Dox) on MDA-MB-231 SKBR-3 tissues at the tissues of the microfluidic system.

#### 4.2.3.3 RT-PCR Results

qRT-PCR analyses were performed in duplicate for each group. Ct values ( $-2^{\Delta\Delta C_t}$ ) obtained for each gene were calculated, and changes in gene expression levels between groups were determined. The results obtained with two replicates were evaluated with the SPSS 16.0 program, and differences with p values less than 0.05 and changes in gene expression levels more than 2 times or less were considered "statistically significant". A comparison of gene expression levels with statistically significant differences between the groups can be seen in Figures 4.35-4.38 and Appendix c.

In humans, the Bcl-2 gene is a founding member of the Bcl-2 regulatory protein family, which regulates cell death by inhibiting or inducing apoptosis. Bcl-2 is localized to the outer membrane of the mitochondria, where it plays an important role in cell survival by inhibiting pro-apoptotic proteins<sup>77</sup>. While no significant differences were observed in Bcl-2 gene expression in the MDA-MB-231 (Figure 4.35) and MCF-7 groups (Appendix c), it was determined that there was an approximately 2-fold increase in the SKBR-3 group that received PAL-DcMNPs compared to the control and only Palbociclib applied groups.

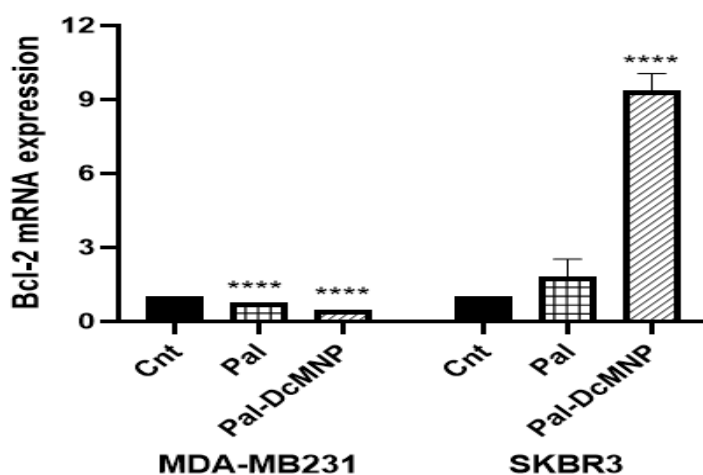


Figure 4.35: Expression levels of Bcl2 genes in untreated and treated MDA-MB-231 and SKBR3 cell lines with 15 $\mu$ M Palbociclib and PAL-DcMNPs for 96h, when  $p < 0.05$ .

Interleukin-6 (IL-6), one of the major cytokines in the tumor microenvironment, is an important factor found in high concentrations in cancer and known to be deregulated. Its overexpression has been reported in almost all tumor types<sup>77</sup>. The strong relation between inflammation and cancer is associated with high levels of IL-6 in the tumor microenvironment. All the distinctive features of cancer; it accelerates tumorigenesis by regulating multiple signaling pathways, including apoptosis, survival, proliferation, angiogenesis, and metastasis. It was shown that IL-6 gene expression level was significantly decreased by 11-fold and 4-fold in MCF-7 and SKBR-3 tumor groups treated with PAL-DcMNPs and Palbociclib treated group, respectively (Appendix c and Figure 4.36).

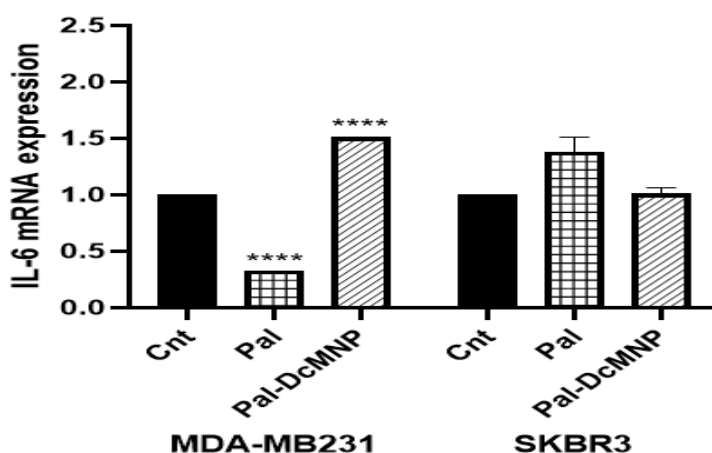


Figure 4.36: Expression levels of IL6 genes in untreated and treated MDA-MB-231 and SKBR3 cell lines with 15 $\mu$ M Palbociclib, and PAL-DcMNPs for 96h, when  $p < 0.05$ .

Despite the increase in Bcl-2 gene expression in SKBR-3 tumor tissues treated with PAL-DcMNPs, IL-6 was significantly decreased, indicating that tumor growth can be suppressed in this way. For this gene expression, no significant difference was detected in the MDA-MB-231 tumor groups treated with Palbociclib and PAL-DcMNPs compared to the control. It was determined that the IL-6 gene decreased approximately 47 times in MDA-MB-231 tumors due to free Palbociclib treatment, but there was no significant difference in MDA-MB-231 tumor groups treated with PAL-DcMNPs compared to control.



BRCA1, a human tumor suppressor gene, is normally expressed in breast and other tissue cells and helps repair damaged DNA, leading to cell death when DNA damage cannot be repaired. It is noteworthy that BRCA1 gene expression was decreased by 4 and 30 fold, respectively, in tumor tissues formed with SKBR-3 and MCF-7 cells treated with PAL-DcMNPs (Appendix c and Figure 4.37). No significant difference was observed in MDA-MB-231 tumor tissues compared to the control. While no significant difference was observed in MDA-MB-231 tumor tissues compared to the control group, it was determined that there was a 30-fold decrease in BRCA1 gene expression in these tumor tissues compared to the control group due to free Palbociclib application.

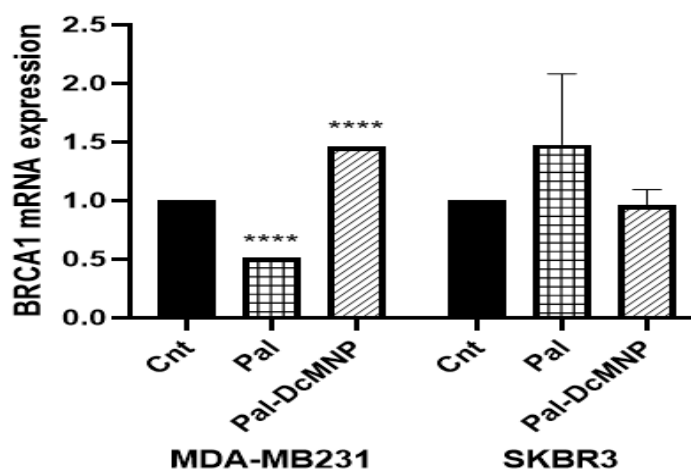


Figure 4.37: Expression levels of BRCA1 genes in untreated and treated MDA-MB-231 and SKBR3 cell lines with 15 $\mu$ M Palbociclib, and PAL-DcMNPs for 96h, when  $p < 0.05$ .

p53 is a tumor suppressor protein that regulates cell division by preventing cells from growing and dividing too quickly or uncontrollably. The expression of this gene, which is very important for tumor development, was found to be increased approximately 12-fold in MDA-MB-231 tumor tissue treated with PAL-DcMNPs. No significant difference was found for SKBR-3 and MCF-7 tumor groups. This result indicates that the tumor developed with MDA-MB-231 cells can be suppressed via the p53 gene with PAL-DcMNPs.

P-glycoprotein 1 is known as an important protein of the cell membrane, which is encoded by the MDR1 gene and pumps many foreign substances out of cells. The development of multidrug resistance (MDR) to chemotherapy is a major challenge in cancer treatment. One of the mechanisms of multidrug resistance is the significant reduction of the uptake of chemotherapeutic agents into cancer cells due to increased MDR1 gene expression and increased P-glycoprotein.

Thus, anticancer agents cannot reach the targeted dose in cancer cells; thus, drug resistance develops. When we examined the tumor groups, it was found that PAL-DcMNPs decreased MDR1 gene expression levels 7 and 6 times compared to free Palbociclib treated SKBR-3 and MCF-7 tumor groups, respectively (Figure 4.38 and Appendix c). This result indicates that the treatment of PAL-DcMNPs in this group of tumors can significantly reduce the development of drug resistance compared to the free drug. In the MDA-MB-231 tumor, however, no significant difference was found between the groups for this gene expression.

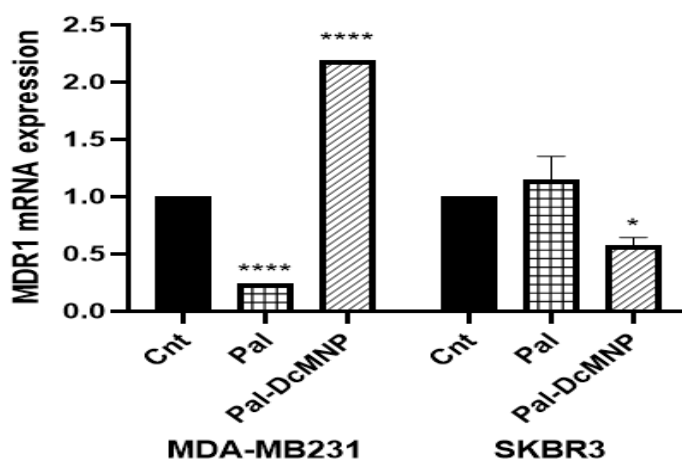


Figure 4.38: Expression levels of MDR1 genes in untreated and treated MDA-MB-231 and SKBR3 cell lines with 15 $\mu$ M Palbociclib, and PAL-DcMNPs for 96h, when  $p < 0.05$ .

When gene expression analyzes were evaluated in general in all groups, the effects of PAL-DcMNPs on gene expression levels were more similar for SKBR-3 and MCF-7 groups. It can be said that the MDA-MB-231 tumor group is affected by different pathways.

### 4.3 Conclusion

In this chapter, in the first step, 2D, 3D, and ex-vivo MCF-7, MDA-MB-231, and SKBR-3 breast cancer cell culture models were compared in terms of the cellular uptake of G5.5 PAMAM dendrimer coated magnetic nanoparticles. The cellular uptake of FITC conjugated G5.5 DcMNPs was visualized by flow cytometry and confocal microscopy. According to confocal image results, efficient cellular internalization was observed due to the small size of G5.5 DcMNPs (15-20 nm). The results concluded that the size of the nanoparticles is a critical parameter for internalization into cells and spheroids. Also, using the advantage of targetability of magnetic nanoparticles under a magnetic field increases the accumulation in the core part of the spheroids and micro-dissected tissues. Both of these properties are important factors for efficient drug delivery.

In the second step, the cytotoxicity of Palbociclib and Palbociclib conjugated magnetic PAMAM dendrimer in 2D, 3D, and Ex-vivo cultures on MCF7, MDAMB231, and SKBR3 cells were tested, and compared. The results show that the cytotoxicity of Palbociclib and PAL-DcMNPs was dose-dependent. At the higher concentrations (50 $\mu$ M), free Palbociclib has a more cytotoxic effect on breast cancer cell lines in 2D and 3D cell cultures. However, with PAL-DcMNPs treatment, it has been observed that drug doses that inhibit 50% of the cell viability can be achieved with even lower drug concentrations (15 $\mu$ M) with respect to free Palbociclib for all of the breast cancer cell lines. The observed effects were more evident for MCF-7 cells than for MDA-MB-231 and SKBR3 cells. In addition, the association between cell viability data and LDH release was also observed at a lower dosage (2.5, 5, and 15  $\mu$ M) of PAL-DcMNPs. However, the values of LDH are relatively high; approximately 2-fold increases in LDH release were seen at MCF-7 and SKBR-3 spheroids after treatment by PAL-DcMNPs.

The ex-vivo pharmacological activity of the 15  $\mu$ M Palbociclib and PAL-DcMNPs was demonstrated by measuring the LHD releases and glucose consumption in tumor-on-a-chip devices. Our results for PAL-DcMNPs after 96 h treatment

showed an increase in the toxic efficiency compared to free drugs in MCF-7, SKBR3, and MDA-MB-231 cell lines.

And finally, the quantification of expression levels of Bax/Bcl-2, CDH1, MDR1, and mTOR genes due to the treatment of free Palbociclib and PAL-DcMNPs in 2D culture were performed by qRTPCR analysis. According to the results, Bax/Bcl2 ratio and CDH1 gene expression increased, followed by PAL-DcMNPs treatments in all three cell lines. On the other hand, MDR1 and mTOR gene expression levels significantly downregulated only in SKBR3 and MDA-MB-231 cell lines, respectively, after treatment with PAL-DcMNPs.

In 3D and ex-vivo cultures, expression levels of Bax/Bcl-2, MDR1, IL-6, IL-8, and BRCA1 genes were performed by qRTPCR. The results showed that Bax/Bcl2 ratio and BRCA1 gene expression significantly increased in MDA-MB-231 and MCF-7 3D and ex-vivo cultures after treatment by PAL-DcMNPs. However, in SKBR-3 3D and ex-vivo cultures, slight upregulation could be seen in Bax/Bcl-2 genes, and downregulation in the BRCA1 gene was seen after treatment by PAL-DcMNPs.

This study's results show that PAL-DcMNPs have a more cytotoxic effect on different culture types of breast cancer cells at lower doses than free drugs and can be further investigated as a potential Palbociclib delivery system in in-vivo studies.

## CHAPTER 5

### CONCLUDING REMARKS

- ✓ The tumor-on-a-chip microfluidic device we have developed in this study allows living tumor tissue to be kept alive and available for testing for 96 hours under laboratory conditions.
- ✓ For the ex vivo culture studies of the project, tumors were first formed in CD1 nude mice with MDA-MB-231, SKBR-3, and MCF-7 cells by subcutaneous injection method. Among the groups, tumor development with estrogen receptor positive MCF-7 cells (n=1) was more complicated than with estrogen receptor negative SKBR-3 (n=5) and MDA-MB-231 (n=4) cells.
- ✓ It has been demonstrated that the device can be used as a suitable platform for cultivating tumor slices with appropriate oxygen and CO<sub>2</sub> concentrations.
- ✓ In comparison with a well-plate system, tumor slices cultivated in a microfluidic system showed the most intensive metabolic activity.
- ✓ Using micro-dissected tumor tissue in the microfluidic system will allow studying the therapeutic response in tumor tissue much more closely than in-vivo studies.
- ✓ In this study, for the first time, Palbociclib was loaded and conjugated into Magnetic PAMAM dendrimers and brought into the form of a targeted drug delivery system.
- ✓ The generation in which Palbociclib bonded most effectively to PAMAM dendrimer-coated magnetic nanoparticles was determined as G5.5 with a 51% loading and 75% conjugating efficiency.
- ✓ The conjugation of Palbociclib to PAMAM dendrimer-coated magnetic nanoparticles was demonstrated by TEM, SEM, Zeta potential, and FTIR analyses.

- ✓ It was determined that PAMAM dendrimer-coated magnetic nanoparticles did not have toxic effects on cell viability when administered alone to MCF-7, MDA-MB-231, and SKBR-3 cell lines.
- ✓ In experiments with confocal microscopy, it has been shown that FITC-labeled nanoparticles are taken into the cell in all 2D cell cultures, and it has been determined that DcMNPs gather around the cell nuclei.
- ✓ The cell viability analyses of Palbociclib and Palbociclib conjugated magnetic PAMAM dendrimer (PAL-DcMNPs) revealed that, at the same concentration, PAL-DcMNPs are more effective in 2D cell cultures than Palbociclib treatment.
- ✓ Expression of the Bax/Bcl2 ratio and CDH1 genes increased in all PAL-DcMNPs treated 2D cell lines.
- ✓ PAL-DcMNPs application caused a decrease in MDR1 and mTOR gene expression levels in MDA-MB-231 and SKBR-3 cells.
- ✓ The best three-dimensional sphere formation in 3D cell cultures was achieved at the end of 4 days with  $1 \times 10^4$  cell numbers and the hanging drop method.
- ✓ It was observed that the morphological structures of MCF-7, SKBR-3, and MDA-MB-231 cell spheres reproduced in a 3D cell culture medium differed. While MCF-7 cells form 3D spheres by connecting more smoothly and tightly to each other, MDA-MB-231 cells have a more easily dispersed structure. SKBR-3 cells, on the other hand, were cultivated in the same number as MCF-7 and MDA-MB-231 cells and formed smaller cell spheres.
- ✓ Confocal microscope images from 3D cell cultures showed that after eight days of cultivation, the cells did not have necrosis, and the number of dead cells stained with PI in the center of the 3D cells was very low.
- ✓ According to cell viability analyses performed by confocal microscopy method, it was observed that 3D-MCF-7 cells started to die from within the cell sphere due to drug application for 4 days. In 3D-MDA-MB-231 cells, it was determined that the structure of the cell spheres began to deteriorate, and the cells tended to disperse. In 3D-SKBR-3 cells, on the other hand, when the drug

was applied, it was observed that the cells outside the sphere began to die, and the cell sphere structure began to shrink.

- ✓ PAL-DcMNPs show more cytotoxicity effects in all cell lines than free Palbociclib treated spheres.
- ✓ It has been determined that the particle distribution marked with FITC is more homogeneous in the spheres with magnet application in 3D breast cancer cell lines and that the particle can penetrate up to the inner layers of the sphere. It was observed that in the spheres without magnet application, the particles entered the sphere less and their distribution was not homogeneous. This result shows that our magnetic nanoparticles have the ability to be targeted in the presence of a magnetic field.
- ✓ Compared to control 3D-MCF-7 cells treated with Palbociclib, the expression of the IL-6 and IL-8 genes decreased, and no significant change was observed in the expression of the BRCA1 gene.
- ✓ Palbociclib and PAL-DcMNPs administration caused different results in 3D-MCF-7, MDA-MB-231 and SKBR-3 cells. Although the BCL2/BAX ratio was increased in 3D-MDA-MB-231 and 3D-SKBR-3 cells, and decreased in Palbociclib treated MCF-7 cells and increased in PAL-DcMNPs treated MCF-7 cells were observed.
- ✓ Tumor sections formed with MCF-7, SKBR-3 and MDA-MB-231 cells cultured in a microfluidic system showed an increase in the amount of LDH released as expected due to tissue damage due to microsection in the first 24 hours. In addition, it was noted that there was more LDH release from tumor tissues to which PAL-DcMNPs were applied compared to control tissues and tissues to which Palbociclib was applied. These results suggest that DcMNPs conjugated Palbociclib penetrated the tissue for 96 hours and may have started to exert their effects after that.
- ✓ Similar to what we observed in 3D cell cultures, Palbociclib conjugated DcMNPs penetrate the inner parts of tumor tissues under the influence of magnets in ex vivo tumor tissues.

- ✓ When the changes in gene expression levels due to control, free drug and Palbociclib-loaded DcMNPs administration in ex vivo cultures were evaluated, significant differences were found in the expression levels of 5 genes in all groups.
- ✓ IL-6 in SKBR-3 and MCF-7 tumors compared to free Palbociclib administration of Palbociclib-loaded DcMNPs and control group; it is noteworthy that it can suppress p53 in MDA-MB-231 tumors.
- ✓ When gene expression analyzes were evaluated in general in all groups formed with SKBR-3, MDA-MB-231, and MCF-7 cells, the effects of Palbociclib conjugated DcMNPs on gene expression levels were more similar for SKBR-3 and MCF-7 groups; It can be said that the MDA-MB-231 tumor group is affected by different pathways.
- ✓ In general, it was observed that 2D and 3D culture conditions using the same cells showed different results. However, similar results were obtained in magnetic nanoparticle targeting when 3D cultures were compared with ex vivo culture conditions.

Magnetic nanoparticles with very small sizes are gaining importance among the new generation targeted chemotherapy systems by playing a role in directing the drugs to the desired area in the desired amount. However, there are some limitations in preclinical cancer models used in studies on this subject. Cell culture models are known to lack the tumor microenvironment, which is known to have a significant impact on tumor biology and therapeutic response. In vivo studies, on the other hand, are quite laborious and costly. In recent years, 3D artificial matrices have been used to bridge the gap between 2D cell culture and complex animal systems. Studies of the project comparing 2D- and 3D- cell cultures have shown that the same cell lines elicit different responses to Palbociclib and Palbociclib conjugated magnetic nanoparticles in various culture media.



The microchannel system we have developed allows living tumor tissue to be kept alive and tested in laboratory conditions for 96 hours. The importance of this is that it will allow the therapeutic response in tumor tissue to be studied most closely to the in vivo model, without the need for laborious and costly in vivo studies. Thus, it will facilitate the testing of biopsy samples to be taken from patients for the effectiveness of different chemotherapeutic agents in laboratory conditions in the future, and it will be of great benefit in the development of personalized treatments.



## REFERENCES

- (1) Özkayar, G.; Mutlu, E.; Şahin, Ş.; Yalçın, Y. D.; Töral, T.; Külah, H.; Yıldırım, E.; Zorlu, Ö.; Özgür, E. A Novel Microfluidic Method Utilizing a Hydrofoil Structure to Improve Circulating Tumor Cell Enrichment: Design and Analytical Validation. *Micromachines* **2020**, *11* (11), 1–17. <https://doi.org/10.3390/mi11110981>.
- (2) Gholizadeh, S.; Shehata Draz, M.; Zarghooni, M.; Sanati-Nezhad, A.; Ghavami, S.; Shafiee, H.; Akbari, M. Microfluidic Approaches for Isolation, Detection, and Characterization of Extracellular Vesicles: Current Status and Future Directions. *Biosens. Bioelectron.* **2017**, *91* (December 2016), 588–605. <https://doi.org/10.1016/j.bios.2016.12.062>.
- (3) Rodriguez, A. D.; Horowitz, L. F.; Castro, K.; Kenerson, H.; Bhattacharjee, N.; Gandhe, G.; Raman, A.; Monnat, R. J.; Yeung, R.; Rostomily, R. C.; et al. A Microfluidic Platform for Functional Testing of Cancer Drugs on Intact Tumor Slices. *Lab Chip* **2020**, *20* (9), 1658–1675. <https://doi.org/10.1039/c9lc00811j>.
- (4) Valente, K. P.; Khetani, S.; Kolahchi, A. R.; Sanati-Nezhad, A.; Suleman, A.; Akbari, M. Microfluidic Technologies for Anticancer Drug Studies. *Drug Discov. Today* **2017**, *22* (11), 1654–1670. <https://doi.org/10.1016/j.drudis.2017.06.010>.
- (5) Damiati, S.; Kompella, U. B.; Damiati, S. A.; Kodzius, R. Microfluidic Devices for Drug Delivery Systems and Drug Screening. *Genes (Basel)*. **2018**, *9* (2). <https://doi.org/10.3390/genes9020103>.
- (6) Astolfi, M.; Péant, B.; Lateef, M. A.; Rousset, N.; Kendall-Dupont, J.; Carmona, E.; Monet, F.; Saad, F.; Provencher, D.; Mes-Masson, A. M.; et al. Micro-Dissected Tumor Tissues on Chip: An Ex Vivo Method for Drug Testing and Personalized Therapy. *Lab Chip* **2016**, *16* (2), 312–325. <https://doi.org/10.1039/c5lc01108f>.
- (7) Perestrelo, A. R.; Águas, A. C. P.; Rainer, A.; Forte, G. Microfluidic Organ/Body-on-a-Chip Devices at the Convergence of Biology and Microengineering. *Sensors (Switzerland)* **2015**, *15* (12), 31142–31170. <https://doi.org/10.3390/s151229848>.
- (8) Vaira, V.; Fedele, G.; Pyne, S.; Fasoli, E.; Zadra, G.; Bailey, D.; Snyder, E.; Favarsani, A.; Coggi, G.; Flavin, R.; et al. Preclinical Model of Organotypic Culture for Pharmacodynamic Profiling of Human Tumors. *Proc. Natl. Acad. Sci. U. S. A.* **2010**, *107* (18), 8352–8356. <https://doi.org/10.1073/pnas.0907676107>.

- (9) Kashaninejad, N.; Nikmaneshi, M. R.; Moghadas, H.; Oskouei, A. K.; Rismanian, M.; Barisam, M.; Saidi, M. S.; Firoozabadi, B. Organ-Tumor-on-a-Chip for Chemosensitivity Assay: A Critical Review. *Micromachines* **2016**, *7* (8). <https://doi.org/10.3390/mi7080130>.
- (10) Carr, S. D.; Green, V. L.; Stafford, N. D.; Greenman, J. Analysis of Radiation-Induced Cell Death in Head and Neck Squamous Cell Carcinoma and Rat Liver Maintained in Microfluidic Devices. *Otolaryngol. - Head Neck Surg. (United States)* **2014**, *150* (1), 73–80. <https://doi.org/10.1177/0194599813507427>.
- (11) Christensen, M. G.; Cawthorne, C.; Dyer, C. E.; Greenman, J.; Pamme, N. Investigating Oxygen Transport Efficiencies in Precision-Cut Liver Slice-Based Organ-on-a-Chip Devices. *Microfluid. Nanofluidics* **2021**, *25* (4), 1–12. <https://doi.org/10.1007/s10404-021-02434-x>.
- (12) Gupta, N.; Liu, J. R.; Patel, B.; Solomon, D. E.; Vaidya, B.; Gupta, V. Microfluidics-Based 3D Cell Culture Models: Utility in Novel Drug Discovery and Delivery Research. *Bioeng. Transl. Med.* **2016**, *1* (1), 63–81. <https://doi.org/10.1002/btm2.10013>.
- (13) Graaf, I. A. M. De; Olinga, P.; Jager, M. H. De; Merema, M. T.; Kanter, R. De; Kerkhof, E. G. Van De; Groothuis, G. M. M. Preparation and Incubation of Precision-Cut Liver and Intestinal Slices for Application in Drug Metabolism and Toxicity Studies. *Nat. Protoc.* **2010**, *5* (9), 1540–1551. <https://doi.org/10.1038/nprot.2010.111>.
- (14) Azimzadeh, M.; Khashayar, P.; Amereh, M.; Tasnim, N.; Hoorfar, M.; Akbari, M. Microfluidic-Based Oxygen ( O 2 ) Sensors for On-Chip Monitoring of Cell , Tissue and Organ Metabolism. **2022**.
- (15) Baydoun, M.; Treizeibré, A.; Follet, J.; Vanneste, S. B.; Creusy, C.; Dercourt, L.; Delaire, B.; Mouray, A.; Viscogliosi, E.; Certad, G.; et al. An Interphase Microfluidic Culture System for the Study of Ex Vivo Intestinal Tissue. *Micromachines* **2020**, *11* (2). <https://doi.org/10.3390/mi11020150>.
- (16) Zhang, Y. S.; Zhang, Y. N.; Zhang, W. Cancer-on-a-Chip Systems at the Frontier of Nanomedicine. *Drug Discov. Today* **2017**, *22* (9), 1392–1399. <https://doi.org/10.1016/j.drudis.2017.03.011>.
- (17) Ramzy, G. M.; Koessler, T.; Ducrey, E.; McKee, T.; Ris, F.; Buchs, N.; Rubbia-Brandt, L.; Dietrich, P. Y.; Nowak-Sliwinska, P. Patient-Derived in Vitro Models for Drug Discovery in Colorectal Carcinoma. *Cancers (Basel)*. **2020**, *12* (6), 1–21. <https://doi.org/10.3390/cancers12061423>.
- (18) Horowitz, L. F.; Rodriguez, A. D.; Ray, T.; Folch, A. Microfluidics for Interrogating Live Intact Tissues. *Microsystems Nanoeng.* **2020**, *6* (1). <https://doi.org/10.1038/s41378-020-0164-0>.

- (19) L. F. Horowitz, D. Rodriguez, Z. Dereli-Korkut, R. Lin, K. Castro, A. Mikheev, R. J. Monnat Jr., A. Folch, and R. C. R. Multiplexed Drug Testing of Tumor Slices Using a Microfluidic Platform **AUTHORS. 2020.**
- (20) World Health Organization <https://www.who.int/news-room/fact-sheets/detail/cancer>.
- (21) Zubair, M.; Wang, S.; Ali, N. Advanced Approaches to Breast Cancer Classification and Diagnosis. **2021, 11** (February), 1–24. <https://doi.org/10.3389/fphar.2020.632079>.
- (22) Holliday, D. L.; Speirs, V. Choosing the Right Cell Line for Breast Cancer Research. *Breast Cancer Res.* **2011, 13** (4), 215. <https://doi.org/10.1186/bcr2889>.
- (23) Mohamed, A.; Krajewski, K.; Cakar, B.; Ma, C. X. Targeted Therapy for Breast Cancer. *Am. J. Pathol.* **2013, 183** (4), 1096–1112. <https://doi.org/10.1016/j.ajpath.2013.07.005>.
- (24) Carranza-Torres, I. E.; Guzmán-Delgado, N. E.; Coronado-Martínez, C.; Bañuelos-García, J. I.; Viveros-Valdez, E.; Morán-Martínez, J.; Carranza-Rosales, P. Organotypic Culture of Breast Tumor Explants as a Multicellular System for the Screening of Natural Compounds with Antineoplastic Potential. *Biomed Res. Int.* **2015, 2015**. <https://doi.org/10.1155/2015/618021>.
- (25) Lee, J. J.; Huang, J.; England, C. G.; McNally, L. R.; Frieboes, H. B. Predictive Modeling of in Vivo Response to Gemcitabine in Pancreatic Cancer. *PLoS Comput. Biol.* **2013, 9** (9), e1003231. <https://doi.org/10.1371/journal.pcbi.1003231>.
- (26) Naipal, K. A. T.; Verkaik, N. S.; Sánchez, H.; van Deurzen, C. H. M.; den Bakker, M. A.; Hoeijmakers, J. H. J.; Kanaar, R.; Vreeswijk, M. P. G.; Jager, A.; van Gent, D. C. Tumor Slice Culture System to Assess Drug Response of Primary Breast Cancer. *BMC Cancer* **2016, 16** (1), 1–13. <https://doi.org/10.1186/s12885-016-2119-2>.
- (27) Ahmad, A.; Wang, Z.; Ali, R.; Bitar, B.; Logna, F. T.; Maitah, M. Y.; Bao, B.; Ali, S. Cell Cycle Regulatory Proteins in Breast Cancer: Molecular Determinants of Drug Resistance and Targets for Anticancer Therapies. **2009.**
- (28) Shapira, A.; Livney, Y. D.; Broxterman, H. J.; Assaraf, Y. G. Nanomedicine for Targeted Cancer Therapy: Towards the Overcoming of Drug Resistance. *Drug Resist. Updat.* **2011, 14** (3), 150–163. <https://doi.org/10.1016/j.drug.2011.01.003>.
- (29) Nounou, M. I.; Elamrawy, F.; Ahmed, N.; Abdelraouf, K.; Goda, S.; Syed-Sha-Qhattal, H. Breast Cancer: Conventional Diagnosis and Treatment

Modalities and Recent Patents and Technologies Supplementary Issue:  
Targeted Therapies in Breast Cancer Treatment. *Breast Cancer Basic Clin. Res.* **2015**, *9*, 17–34. <https://doi.org/10.4137/BCBCR.S29420>.

- (30) 2021 Clinical Development Success Rates 2011-2020 V17. **2020**.
- (31) Astolfi, M.; St-Georges-Robillard, A.; Leblond, F.; Mes-Masson, A.-M.; Gervais, T. Microfluidics and Spectroscopic Imaging for Personalized Medicine in Ovarian Cancer. *SPIE Newsroom* **2016**, 10–12. <https://doi.org/10.1117/2.1201602.006352>.
- (32) Olubajo, F.; Achawal, S.; Greenman, J. Development of a Microfluidic Culture Paradigm for Ex Vivo Maintenance of Human Glioblastoma Tissue: A New Glioblastoma Model? *Transl. Oncol.* **2020**, *13* (1), 1–10. <https://doi.org/10.1016/j.tranon.2019.09.002>.
- (33) Privalova, A. M.; Uglanova, S. V; Kuznetsova, N. R.; Klyachko, N. L.; Golovin, Y. I.; Korenkov, V. V; Vodovozova, E. L.; Markvicheva, E. A. Microencapsulated Multicellular Tumor Spheroids as a Tool to Test Novel Anticancer Nanosized Drug Delivery Systems In Vitro. **2015**. <https://doi.org/10.1166/jnn.2015.10508>.
- (34) Gupta, A. K.; Sharma, S.; Dahiya, N.; Brashier, D. B. S. Palbociclib: A Breakthrough in Breast Carcinoma in Women. *Med. J. Armed Forces India* **2016**, *72*, S37–S42. <https://doi.org/10.1016/j.mjafi.2015.11.002>.
- (35) Tang, L. H.; Contractor, T.; Clausen, R.; Klimstra, D. S.; Du, Y. C. N.; Allen, P. J.; Brennan, M. F.; Levine, A. J.; Harris, C. R. Attenuation of the Retinoblastoma Pathway in Pancreatic Neuroendocrine Tumors Due to Increased Cdk4/Cdk6. *Clin. Cancer Res.* **2012**, *18* (17), 4612–4620. <https://doi.org/10.1158/1078-0432.CCR-11-3264>.
- (36) Vijayaraghavan, S.; Karakas, C.; Doostan, I.; Chen, X.; Bui, T.; Yi, M.; Raghavendra, A. S.; Zhao, Y.; Bashour, S. I.; Ibrahim, N. K.; et al. CDK4/6 and Autophagy Inhibitors Synergistically Induce Senescence in Rb Positive Cytoplasmic Cyclin e Negative Cancers. *Nat. Commun.* **2017**, *8* (May), 1–17. <https://doi.org/10.1038/ncomms15916>.
- (37) Mohamed, A.; Krajewski, K.; Cakar, B.; Ma, C. X. Targeted Therapy for Breast Cancer. *Am. J. Pathol.* **2013**, *183* (4), 1096–1112. <https://doi.org/10.1016/j.ajpath.2013.07.005>.
- (38) Rajan, M.; Praphakar, R. A.; Govindaraj, D.; Arulselvan, P.; Kumar, S. S. Cytotoxicity Assessment of Palbociclib-Loaded Chitosan-Polypropylene Glycol Nano Vehicles for Cancer Chemotherapy. *Mater. Today Chem.* **2017**, *6*, 26–33. <https://doi.org/10.1016/j.mtchem.2017.08.002>.
- (39) Marcinkowska, M.; Sobierajska, E.; Stanczyk, M.; Janaszewska, A.; Chworos, A.; Klajnert-Maculewicz, B. Conjugate of PAMAM Dendrimer,

- Doxorubicin and Monoclonal Antibody-Trastuzumab: The New Approach of a Well-Known Strategy. *Polymers (Basel)*. **2018**, *10* (2), 1–11. <https://doi.org/10.3390/polym10020187>.
- (40) Parsian, M.; Mutlu, P.; Yalcin, S.; Tezcaner, A.; Gunduz, U. Half Generations Magnetic PAMAM Dendrimers as an Effective System for Targeted Gemcitabine Delivery. *Int. J. Pharm.* **2016**, *515* (1–2), 104–113. <https://doi.org/10.1016/j.ijpharm.2016.10.015>.
- (41) Parsian, M.; Unsoy, G.; Mutlu, P.; Yalcin, S.; Tezcaner, A.; Gunduz, U. Loading of Gemcitabine on Chitosan Magnetic Nanoparticles Increases the Anti-Cancer Efficacy of the Drug. *Eur. J. Pharmacol.* **2016**, *784*, 121–128. <https://doi.org/10.1016/j.ejphar.2016.05.016>.
- (42) Arruebo, M.; Fernández-pacheco, R.; Ibarra, M. R.; Santamaría, J. Magnetic Nanoparticles for Drug Delivery. **2007**, *2* (3), 22–32.
- (43) Parsian, M.; Mutlu, P.; Yalçın, S.; Gündüz, U. Characterization of Gemcitabine Loaded Polyhydroxybutyrate Coated Magnetic Nanoparticles for Targeted Drug Delivery. *Anticancer. Agents Med. Chem.* **2020**, *20*, 1–8. <https://doi.org/10.2174/1871520620666200310091026>.
- (44) Jain, A.; Dubey, S.; Kaushik, A.; Tyagi, A. Dendrimer: A Complete Drug Carrier. *Int. J. Pharm. Sci. Res.* **2010**, *1* (4), 38–52.
- (45) Shrestha, B.; Wang, L.; Brey, E. M.; Uribe, G. R.; Tang, L. Smart Nanoparticles for Chemo-based Combinational Therapy. *Pharmaceutics* **2021**, *13* (6). <https://doi.org/10.3390/pharmaceutics13060853>.
- (46) Edwards, E. E.; Villani, T. S.; Gardner, G.; Johnson, M.; Crider, N. Comparison of 2D versus 3D Cell Culture Models for Drug Screening in the Context of Breast Cancer. **2018**, 2–5.
- (47) Tung, Y. C.; Hsiao, A. Y.; Allen, S. G.; Torisawa, Y. S.; Ho, M.; Takayama, S. High-Throughput 3D Spheroid Culture and Drug Testing Using a 384 Hanging Drop Array. *Analyst* **2011**, *136* (3), 473–478. <https://doi.org/10.1039/c0an00609b>.
- (48) Clémence, D.; Robin, D.; Pierre, D.; Corinne, A.; Claire, S.; Christelle, B.; Emmanuelle, M.; Frédérique, P.-L.; Bamdad, M. Development and Cytotoxic Response of Two Proliferative MDA-MB-231 and Non-Proliferative SUM1315 Three-Dimensional Cell Culture Models of Triple-Negative Basal-like Breast Cancer Cell Lines. *Oncotarget* **2017**, *8* (56), 95316–95331. <https://doi.org/10.18632/oncotarget.20517>.
- (49) Zhu, W.; Holmes, B.; Glazer, R. I.; Zhang, L. G. 3D Printed Nanocomposite Matrix for the Study of Breast Cancer Bone Metastasis. *Nanomedicine Nanotechnology, Biol. Med.* **2016**, *12* (1), 69–79. <https://doi.org/10.1016/j.nano.2015.09.010>.

- (50) Tavakol, D. N.; Fleischer, S.; Vunjak-Novakovic, G. Harnessing Organs-on-a-Chip to Model Tissue Regeneration. *Cell Stem Cell* **2021**, *28* (6), 993–1015. <https://doi.org/10.1016/j.stem.2021.05.008>.
- (51) Pampaloni, F.; Reynaud, E. G.; Stelzer, E. H. K. The Third Dimension Bridges the Gap between Cell Culture and Live Tissue. *Nature Reviews Molecular Cell Biology*. 2007, pp 839–845. <https://doi.org/10.1038/nrm2236>.
- (52) Carter, E. P.; Gopsill, J. A.; Gomm, J. J.; Jones, J. L.; Grose, R. P. A 3D In Vitro Model of the Human Breast Duct: A Method to Unravel Myoepithelial-Luminal Interactions in the Progression of Breast Cancer. *Breast Cancer Res.* **2017**, *19* (1), 1–10. <https://doi.org/10.1186/s13058-017-0843-4>.
- (53) Majumder, B.; Baraneedharan, U.; Thiyagarajan, S.; Radhakrishnan, P.; Narasimhan, H.; Dhandapani, M.; Brijwani, N.; Pinto, D. D.; Prasath, A.; Shanthappa, B. U.; et al. Predicting Clinical Response to Anticancer Drugs Using an Ex Vivo Platform That Captures Tumour Heterogeneity. *Nat. Commun.* **2015**, 1–14. <https://doi.org/10.1038/ncomms7169>.
- (54) Astolfi, M.; Péant, B.; Lateef, M. A.; Rousset, N.; Kendall-Dupont, J.; Carmona, E.; Monet, F.; Saad, F.; Provencher, D.; Mes-Masson, A. M.; et al. Micro-Dissected Tumor Tissues on Chip: An Ex Vivo Method for Drug Testing and Personalized Therapy. *Lab Chip* **2016**, *16* (2), 312–325. <https://doi.org/10.1039/c5lc01108f>.
- (55) Midwoud, P. M. Van; Verpoorte, E.; Groothuis, G. M. M. An Alternative Approach Based on Microfluidics to Study Drug Metabolism and Toxicity Using Liver and Intestinal Tissue. *Ph. D. Diss.* **2010**.
- (56) Asghar, W.; El Assal, R.; Shafiee, H.; Pitteri, S.; Paulmurugan, R.; Demirci, U. Engineering Cancer Microenvironments for in Vitro 3-D Tumor Models. *Mater. Today* **2015**, *18* (10), 539–553. <https://doi.org/10.1016/j.mattod.2015.05.002>.
- (57) Spinelli, J. B.; Yoon, H.; Ringel, A. E.; Jeanfavre, S.; Clish, C. B.; Haigis, M. C. Supports Breast Cancer Biomass. *Science (80-. )*. **2017**, *358* (6365), 941. <https://doi.org/10.1126/science.aam9305>.Metabolic.
- (58) Baxter, L. T.; Jain, R. K. Transport of Fluid and Macromolecules in Tumors. I. Role of Interstitial Pressure and Convection. *Microvasc. Res.* **1989**, *37* (1), 77–104. [https://doi.org/10.1016/0026-2862\(89\)90074-5](https://doi.org/10.1016/0026-2862(89)90074-5).
- (59) Sosa, J. M.; Huber, D. E.; Welk, B.; Fraser, H. L. Development and Application of MIPAR™: A Novel Software Package for Two- and Three-Dimensional Microstructural Characterization. *Integr. Mater. Manuf. Innov.* **2014**, *3* (1), 123–140. <https://doi.org/10.1186/2193-9772-3-10>.



- (60) Gantenbein-Ritter, B.; Sprecher, C. M.; Chan, S.; Illien-Jünger, S.; Grad, S. Confocal Imaging Protocols for Live/Dead Staining in Three-Dimensional Carriers. *Methods Mol. Biol.* **2011**, *740*, 127–140. [https://doi.org/10.1007/978-1-61779-108-6\\_14](https://doi.org/10.1007/978-1-61779-108-6_14).
- (61) Collins, T.; Pyne, E.; Christensen, M.; Iles, A.; Pamme, N.; Pires, I. M. Spheroid-on-Chip Microfluidic Technology for the Evaluation of the Impact of Continuous Flow on Metastatic Potential in Cancer Models in Vitro. *Biomicrofluidics* **2021**, *15* (4). <https://doi.org/10.1063/5.0061373>.
- (62) Armour, A. D.; Powell, H. M.; Boyce, S. T. Fluorescein Diacetate for Determination of Cell Viability in Tissue-Engineered Skin. *Tissue Eng. - Part C Methods* **2008**, *14* (1), 89–96. <https://doi.org/10.1089/tec.2007.0228>.
- (63) Zlatskiy, I. A.; Zlatska, A. V.; Antipova, N. V.; Dolenko, S. A.; Gordiienko, I. M.; Gubar, O. S.; Vasyliiev, R. G.; Zubov, D. A.; Novikova, S. N.; Syroeshkin, A. V. Comparative Analysis of the Different Dyes' Potential to Assess Human Normal and Cancer Cell Viability in Vitro under Different D / H Ratios in a Culture Medium. *Sci. World J.* **2020**, *2020*. <https://doi.org/10.1155/2020/2373021>.
- (64) Van Midwoud, P. M.; Groothuis, G. M. M.; Merema, M. T.; Verpoorte, E. Microfluidic Biochip for the Perifusion of Precision-Cut Rat Liver Slices for Metabolism and Toxicology Studies. *Biotechnol. Bioeng.* **2010**, *105* (1), 184–194. <https://doi.org/10.1002/bit.22516>.
- (65) Misra, S.; Moro, C. F.; Del Chiaro, M.; Pouso, S.; Sebestyén, A.; Löhr, M.; Björnstedt, M.; Verbeke, C. S. Ex Vivo Organotypic Culture System of Precision-Cut Slices of Human Pancreatic Ductal Adenocarcinoma. *Sci. Rep.* **2019**, *9* (1), 1–16. <https://doi.org/10.1038/s41598-019-38603-w>.
- (66) Khodadust, R.; Unsoy, G.; Yalcin, S.; Gunduz, G.; Gunduz, U. PAMAM Dendrimer-Coated Iron Oxide Nanoparticles: Synthesis and Characterization of Different Generations. *J. Nanoparticle Res.* **2013**, *15* (3), 1488. <https://doi.org/10.1007/s11051-013-1488-6>.
- (67) Marcinkowska, M.; Stanczyk, M.; Janaszewska, A.; Sobierajska, E.; Chworos, A.; Klajnert-Maculewicz, B. Multicomponent Conjugates of Anticancer Drugs and Monoclonal Antibody with PAMAM Dendrimers to Increase Efficacy of HER-2 Positive Breast Cancer Therapy. *Pharm. Res.* **2019**, *36* (11). <https://doi.org/10.1007/s11095-019-2683-7>.
- (68) Khandare, J.; Kolhe, P.; Pillai, O.; Kannan, S.; Lieh-Lai, M.; Kannan, R. M. Synthesis, Cellular Transport, and Activity of Polyamidoamine Dendrimer-Methylprednisolone Conjugates. *Bioconjug. Chem.* **2005**, *16* (2), 330–337. <https://doi.org/10.1021/bc0498018>.
- (69) Zhang, M.; Xiong, X.; Suo, Z.; Hou, Q.; Gan, N.; Tang, P.; Ding, X.; Li, H. Co-Amorphous Palbociclib-Organic Acid Systems with Increased

Dissolution Rate, Enhanced Physical Stability and Equivalent Biosafety. *RSC Adv.* **2019**, *9* (7), 3946–3955. <https://doi.org/10.1039/c8ra09710k>.

- (70) Taghavi Pourianazar, N.; Gunduz, U. CpG Oligodeoxynucleotide-Loaded PAMAM Dendrimer-Coated Magnetic Nanoparticles Promote Apoptosis in Breast Cancer Cells. *Biomed. Pharmacother.* **2016**, *78*, 81–91. <https://doi.org/10.1016/j.biopha.2016.01.002>.
- (71) Arya, G.; Vandana, M.; Acharya, S.; Sahoo, S. K. Enhanced Antiproliferative Activity of Herceptin (HER2)-Conjugated Gemcitabine-Loaded Chitosan Nanoparticle in Pancreatic Cancer Therapy. *Nanomedicine* **2011**, *7* (6), 859–870. <https://doi.org/10.1016/j.nano.2011.03.009>.
- (72) Jochums, A.; Friehs, E.; Sambale, F.; Lavrentieva, A.; Bahnemann, D.; Scheper, T. Revelation of Different Nanoparticle-Uptake Behavior in Two Standard Cell Lines NIH/3T3 and A549 by Flow Cytometry and Time-Lapse Imaging. *Toxics* **2017**, *5* (3), 15. <https://doi.org/10.3390/toxics5030015>.
- (73) Simon Kaja#,\*, Andrew J. Payne\*, Tulsi Singh, Jasleen K. Ghuman, Erin G. Sieck, and P. K. An Optimized Lactate Dehydrogenase Release Assay for Screening of Drug Candidates in Neuroscience. *J Pharmacol Toxicol Methods* **2016**. <https://doi.org/10.1016/j.vascn.2015.02.001.An>.
- (74) Smith, S. M.; Wunder, M. B.; Norris, D. A.; Shellman, Y. G. A Simple Protocol for Using a LDH-Based Cytotoxicity Assay to Assess the Effects of Death and Growth Inhibition at the Same Time. *PLoS One* **2011**, *6* (11). <https://doi.org/10.1371/journal.pone.0026908>.
- (75) Kim, R.; Emi, M.; Tanabe, K.; Toge, T. Therapeutic Potential of Antisense Bcl-2 as a Chemosensitizer for Cancer Therapy. *Cancer* **2004**, *101* (11), 2491–2502. <https://doi.org/10.1002/cncr.20696>.
- (76) Zapata, J. M.; Krajewska, M.; Krajewski, S.; Huang, R. P.; Takayama, S.; Wang, H. G.; Adamson, E.; Reed, J. C. Expression of Multiple Apoptosis-Regulatory Genes in Human Breast Cancer Cell Lines and Primary Tumors. *Breast Cancer Res. Treat.* **1998**, *47* (2), 129–140. <https://doi.org/10.1023/A:1005940832123>.
- (77) Basu, A.; Haldar, S. The Relationship between Bcl2, Bax and P53: Consequences for Cell Cycle Progression and Cell Death. *Mol. Hum. Reprod.* **1998**, *4* (12), 1099–1109. <https://doi.org/10.1093/molehr/4.12.1099>.
- (78) Li, F.; Ackermann, E. J.; Bennett, C. F.; Rothermel, A. L.; Plescia, J.; Tognin, S.; Villa, A.; Marchisio, P. C.; Altieri, D. C. Pleiotropic Cell-Division Defects and Apoptosis Induced by Interference with Survivin Function. *Nat. Cell Biol.* **1999**, *1* (8), 461–466. <https://doi.org/10.1038/70242>.

- (79) Qian, Z. R.; Sano, T.; Yoshimoto, K.; Asa, S. L.; Yamada, S.; Mizusawa, N.; Kudo, E. Tumor-Specific Downregulation and Methylation of the CDH13 (H-Cadherin) and CDH1 (E-Cadherin) Genes Correlate with Aggressiveness of Human Pituitary Adenomas. *Mod. Pathol.* **2007**, *20* (12), 1269–1277. <https://doi.org/10.1038/modpathol.3800965>.
- (80) Tsanou, E.; Peschos, D.; Batistatou, A.; Charalabopoulos, A.; Charalabopoulos, K. The E-Cadherin Adhesion Molecule and Colorectal Cancer. A Global Literature Approach. *Anticancer Res.* **2008**, *28* (6 A), 3815–3826.
- (81) Lu, M. H.; Huang, C. C.; Pan, M. R.; Chen, H. H.; Hung, W. C. Prospero Homeobox 1 Promotes Epithelial-Mesenchymal Transition in Colon Cancer Cells by Inhibiting e-Cadherin via MiR-9. *Clin. Cancer Res.* **2012**, *18* (23), 6416–6425. <https://doi.org/10.1158/1078-0432.CCR-12-0832>.
- (82) Kwak, J. M.; Min, B. W.; Lee, J. H.; Choi, J. S.; Lee, S. Il; Park, S. S.; Kim, J.; Um, J. W.; Kim, S. H.; Moon, H. Y. The Prognostic Significance of E-Cadherin and Liver Intestine-Cadherin Expression in Colorectal Cancer. *Dis. Colon Rectum* **2007**, *50* (11), 1873–1880. <https://doi.org/10.1007/s10350-007-9034-1>.
- (83) Karamitopoulou, E.; Zlobec, I.; Patsouris, E. S.; Peros, G.; Lugli, A. Loss of E-Cadherin Independently predicts the Lymph Node Status in Colorectal Cancer. *Pathology* **2011**, *43* (2), 133–137. <https://doi.org/10.1097/PAT.0b013e3283425b7f>.
- (84) Lugli, A.; Zlobec, I.; Minoo, P.; Baker, K.; Tornillo, L.; Terracciano, L.; Jass, J. R. Prognostic Significance of the Wnt Signalling Pathway Molecules APC,  $\beta$ -Catenin and E-Cadherin in Colorectal Cancer - A Tissue Microarray-Based Analysis. *Histopathology* **2007**, *50* (4), 453–464. <https://doi.org/10.1111/j.1365-2559.2007.02620.x>.
- (85) Filiz, A. I.; Senol, Z.; Sucullu, I.; Kurt, Y.; Demirbas, S.; Akin, M. L. The Survival Effect of E-Cadherin and Catenins in Colorectal Carcinomas. *Color. Dis.* **2010**, *12* (12), 1223–1230. <https://doi.org/10.1111/j.1463-1318.2009.01994.x>.
- (86) Jie, D.; Zhongmin, Z.; Guoqing, L.; Sheng, L.; Yi, Z.; Jing, W.; Liang, Z. Positive Expression of LSD1 and Negative Expression of E-Cadherin Correlate with Metastasis and Poor Prognosis of Colon Cancer. *Dig. Dis. Sci.* **2013**, *58* (6), 1581–1589. <https://doi.org/10.1007/s10620-012-2552-2>.
- (87) Peng Zhao; Su, X.; Ge, T.; Fan, J. An in Vivo Study of Cdh1/APC in Breast Cancer Formation. *Physiol. Behav.* **2016**, *176* (1), 139–148. <https://doi.org/10.1002/ijc.24399>.
- (88) Harada, M.; Morikawa, M.; Ozawa, T.; Kobayashi, M.; Tamura, Y.; Takahashi, K.; Tanabe, M.; Tada, K.; Seto, Y.; Miyazono, K.; et al.

- Palbociclib Enhances Activin-SMAD-Induced Cytostasis in Estrogen Receptor-Positive Breast Cancer. *Cancer Sci.* **2019**, *110* (1), 209–220. <https://doi.org/10.1111/cas.13841>.
- (89) Wang, C.-X.; Fisk, B. C.; Wadehra, M.; Su, H.; Braun, J. Overexpression of Murine Fizzy-Related (Fzr) Increases Natural Killer Cell-Mediated Cell Death and Suppresses Tumor Growth. *Blood* **2000**, *96* (1), 259–263. <https://doi.org/10.1182/blood.v96.1.259>.
- (90) Zhang, H. W.; Hu, J. J.; Fu, R. Q.; Liu, X.; Zhang, Y. H.; Li, J.; Liu, L.; Li, Y. N.; Deng, Q.; Luo, Q. S.; et al. Flavonoids Inhibit Cell Proliferation and Induce Apoptosis and Autophagy through Downregulation of PI3K Mediated PI3K/AKT/MTOR/P70S6K/ULK Signaling Pathway in Human Breast Cancer Cells. *Sci. Rep.* **2018**, *8* (1), 1–13. <https://doi.org/10.1038/s41598-018-29308-7>.
- (91) Hare, S. H.; Harvey, A. J. MTOR Function and Therapeutic Targeting in Breast Cancer. *Am. J. Cancer Res.* **2017**, *7* (3), 383–404.
- (92) Hua, H.; Kong, Q.; Zhang, H.; Wang, J.; Luo, T.; Jiang, Y. Targeting MTOR for Cancer Therapy. *J. Hematol. Oncol.* **2019**, *12* (1), 1–19. <https://doi.org/10.1186/s13045-019-0754-1>.
- (93) Asby, D. J.; Killick-Cole, C. L.; Boulter, L. J.; Singleton, W. G. B.; Asby, C. A.; Wyatt, M. J.; Barua, N. U.; Bienemann, A. S.; Gill, S. S. Combined Use of CDK4/6 and MTOR Inhibitors Induce Synergistic Growth Arrest of Diffuse Intrinsic Pontine Glioma Cells via Mutual Downregulation of MTORC1 Activity. *Cancer Manag. Res.* **2018**, *10*, 3483–3500. <https://doi.org/10.2147/CMAR.S167095>.
- (94) Zhang, J.; Xu, K.; Liu, P.; Geng, Y.; Wang, B.; Gan, W.; Wu, F.; Chin, Y. R.; Berrios, C.; Lien, E. C.; et al. Inhibition of Rb Phosphorylation Leads to MTORC2-Mediated Activation of Akt. *Mol Cell* **2017**, *62* (6), 929–942. <https://doi.org/10.1016/j.molcel.2016.04.023>.Inhibition.
- (95) Bonelli, M. A.; Digiacoimo, G.; Fumarola, C.; Alfieri, R.; Quaini, F.; Falco, A.; Madeddu, D.; La Monica, S.; Cretella, D.; Ravelli, A.; et al. Combined Inhibition of CDK4/6 and PI3K/AKT/MTOR Pathways Induces a Synergistic Anti-Tumor Effect in Malignant Pleural Mesothelioma Cells. *Neoplasia (United States)* **2017**, *19* (8), 637–648. <https://doi.org/10.1016/j.neo.2017.05.003>.
- (96) Cretella, D.; Ravelli, A.; Fumarola, C.; La Monica, S.; Digiacoimo, G.; Cavazzoni, A.; Alfieri, R.; Biondi, A.; Generali, D.; Bonelli, M.; et al. The Anti-Tumor Efficacy of CDK4/6 Inhibition Is Enhanced by the Combination with PI3K/AKT/MTOR Inhibitors through Impairment of Glucose Metabolism in TNBC Cells. *J. Exp. Clin. Cancer Res.* **2018**, *37* (1), 1–12. <https://doi.org/10.1186/s13046-018-0741-3>.

- (97) Albanese, A.; Lam, A. K.; Sykes, E. A.; Rocheleau, J. V.; Chan, W. C. W. Tumour-on-a-Chip Provides an Optical Window into Nanoparticle Tissue Transport. *Nat. Commun.* **2013**, *4*, 1–8. <https://doi.org/10.1038/ncomms3718>.
- (98) Al Wafai, R.; El-Rabih, W.; Katerji, M.; Safi, R.; El Sabban, M.; El-Rifai, O.; Usta, J. Chemosensitivity of MCF-7 Cells to Eugenol: Release of Cytochrome-c and Lactate Dehydrogenase. *Sci. Rep.* **2017**, *7* (January 2016), 1–13. <https://doi.org/10.1038/srep43730>.
- (99) Lee, H. H.; Jung, J.; Moon, A.; Kang, H.; Cho, H. Antitumor and Anti-Invasive Effect of Apigenin on Human Breast Carcinoma through Suppression of IL-6 Expression. *Int. J. Mol. Sci.* **2019**, *20* (13). <https://doi.org/10.3390/ijms20133143>.
- (100) Singh, J. K.; Simões, B. M.; Howell, S. J.; Farnie, G.; Clarke, R. B. Recent Advances Reveal IL-8 Signaling as a Potential Key to Targeting Breast Cancer Stem Cells. *Breast Cancer Res.* **2013**, *15* (4), 1–9. <https://doi.org/10.1186/bcr3436>.
- (101) Fu, X.; Tan, W.; Song, Q.; Pei, H.; Li, J. BRCA1 and Breast Cancer: Molecular Mechanisms and Therapeutic Strategies. *Front. Cell Dev. Biol.* **2022**, *10* (March), 1–11. <https://doi.org/10.3389/fcell.2022.813457>.
- (102) Parsian, M.; Mutlu, P.; Yildirim, E.; Ildiz, C.; Ozen, C.; Gunduz, U. Development of a Microfluidic Platform to Maintain Viability of Micro-Dissected Tumor Slices in Culture. *Biomicrofluidics* **2022**, *16* (3). <https://doi.org/10.1063/5.0087532>.
- (103) Hattersley, S. M.; Sylvester, D. C.; Dyer, C. E.; Stafford, N. D.; Haswell, S. J.; Greenman, J. A Microfluidic System for Testing the Responses of Head and Neck Squamous Cell Carcinoma Tissue Biopsies to Treatment with Chemotherapy Drugs. *Ann. Biomed. Eng.* **2012**, *40* (6), 1277–1288. <https://doi.org/10.1007/s10439-011-0428-9>.
- (104) Yabbarov, N. G.; Posypanova, G. A.; Vorontsov, E. A.; Popova, O. N.; Severin, E. S. Targeted Delivery of Doxorubicin: Drug Delivery System Based on PAMAM Dendrimers. *Biochem.* **2013**, *78* (8), 884–894. <https://doi.org/10.1134/S000629791308004X>.



## APPENDICES

### A. Measuring Cell Death by Propidium Iodide (PI) Uptake

For 2D cell culture, MCF-7 cell was cultured at 96 well plates ( $1 \times 10^4$  cell /well). After 24h, cells were treated with different concentrations of Palbociclib for 96h, and then the medium, which contains dead and mitotic cells, was removed and saved. Detached live with trypsin–EDTA and kept all washes by PBS. Add the cells in the medium and the cells from any washes to the detached cells and harvest all cells by centrifugation at 500g for 5 min and counting by hemocytometer.  $4 \times 10^5$  live cells were resuspended in PI-PBS buffer and incubated the cells at room temperature for 15 min in the dark. Centrifuged and removed the PI and washes the cell twice with PBS. Resuspend the cells at 1ml PBS and put them at dark 96 well plates (100  $\mu$ l/ well). The SpectraMax iD3 microplate reader was set to fluorescent mode with an excitation wavelength of 493 nm and an emission wavelength of 636nm.

For 3D cell culture, MCF-7 cell was cultured at plates ( $1 \times 10^4$  cell /drops). After 4 days, cells were treated with different concentrations of Palbociclib for 96h. The medium and spheroids were removed and centrifuged. The spheroids were trypsinized and washed with PBS and continued like 2D culture.

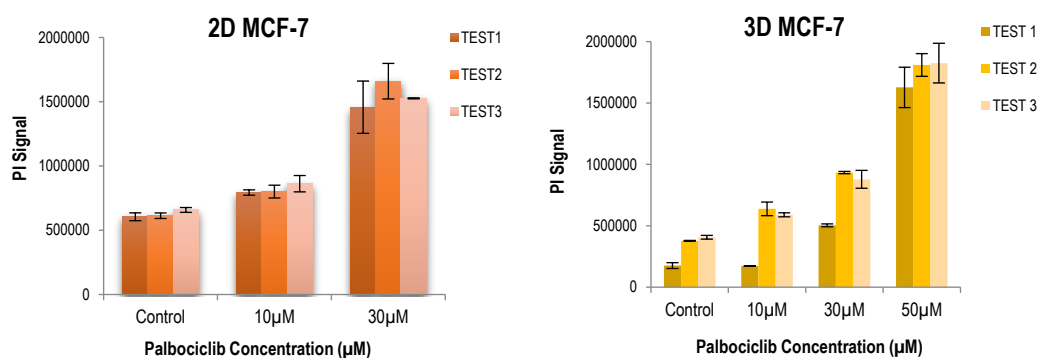


Figure A.1. Dose-response curve for the cytotoxic effects of Palbociclib. (A) Shows the maximum PI signal for 2D MCF-7 cell cultures (B) Shows the maximum PI signal for 3D MCF-7 cell culture.

### B. Anticancer Drug Sensitivity Testing in MCF-7 Ex-vivo Cultures

LDH release analyzes were performed to determine the effects of Palbociclib and Palbociclib conjugated DcMNPs (PAL-DcMNPs), Doxorubicin, and Doxorubicin loaded DcMNPs (Dox-DcMNPs) on MCF-7 tissue samples.

In the MCF-7 group, PAL-DcMNPs at 48, 72, and 96 hours appeared to be more effective than Palbociclib. Statistical analysis could not be performed because the number of samples was 1.

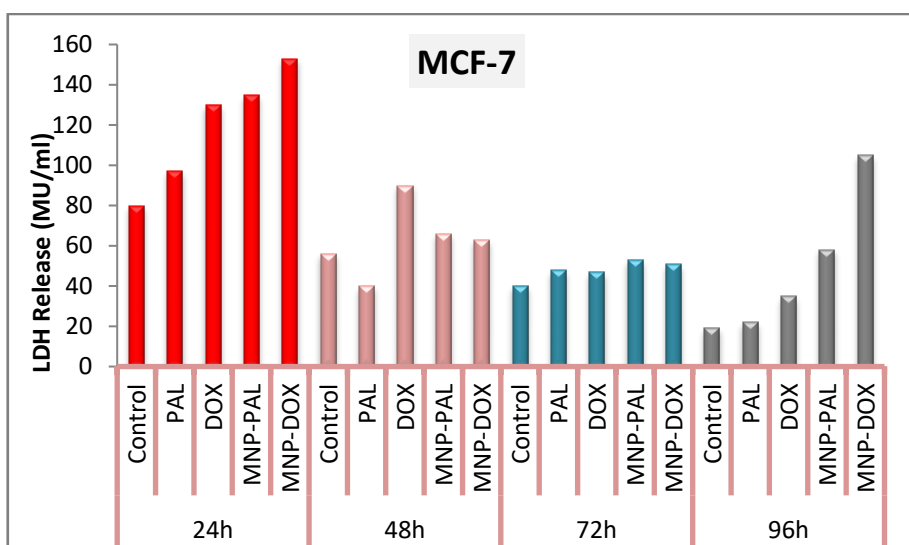


Figure A.2. LDH release after administration of Palbociclib, Palbociclib-loaded DcMNPs (MNP-PAL), Doxorubicin, and Doxorubicin-loaded DcMNPs (MNP-Dox) from tumor sections formed with MCF-7 cells (n=1).



### C. MCF-7 ex-vivo culture RT-PCR results

qRT-PCR analyzes were performed in duplicate for the MCF-7 group. The results obtained with two replicates were evaluated with the SPSS 16.0 program. Differences with p values less than 0.05 and changes in gene expression levels more than 2 times or less were considered "statistically significant". Considering that only one mouse was present, the result was not significant.

Table A. 1. Changes in gene expression levels compared to the MCF-7 control group

| Gene         | MCF-7 Control | MCF-7 Palbociclib |                                    | MCF-7 Pal-DcMNP |                                    |
|--------------|---------------|-------------------|------------------------------------|-----------------|------------------------------------|
|              | Ct            | Ct                | Fold Change $2^{-\Delta\Delta Ct}$ | Ct              | Fold Change $2^{-\Delta\Delta Ct}$ |
| <b>Bcl-2</b> | 33,26         | -                 | -                                  | 28,87           | +1,36                              |
| <b>MDR1</b>  | 35,92         | -                 | -                                  | 34,47           | -5,65                              |
| <b>IL-6</b>  | 33,65         | -                 | -                                  | 33,17           | -11,08                             |
| <b>BRCA1</b> | 31,14         | -                 | -                                  | 32,08           | -29,65                             |
| <b>P53</b>   | 37,07         | -                 | -                                  | 36,14           | -                                  |
| <b>IL8</b>   | 34,77         | -                 | -                                  | 31,02           | -1,15                              |



## CURRICULUM VITAE

Surname, Name: Parsian, Maryam  
Nationality: Iranian  
E-mail: smaryamparsian@gmail.com  
LinkedIn: linkedin.com/in/maryam-parsian

### EDUCATION

| Degree | Institution   | Year of Graduation |
|--------|---|--------------------|
| MS     | <b>Middle East Technical University</b><br>Biotechnology                    | 2014               |
| BS     | <b>Azad University, Iran</b><br>Cellular & Molecular Biology / Microbiology | 2000               |

### LANGUAGES

English (Proficient), Turkish (Proficient), Azeri (Native), Farsi (Native)

### PUBLICATIONS

#### • Papers Published in International Journals

1. **Parsian, M.**, Mutlu, P., Taghavi Pourianazar, N., and Gunduz, U., 2022. Investigation of the Therapeutic Effects of Palbociclib Conjugated Magnetic Nanoparticles on Different Types of Breast Cancer Cell Lines. Submitted
2. **Parsian, M.**, Mutlu, P., Yildirim, E., Ildiz, C., Ozen, C., and Gunduz, U., 2022. Development of a microfluidic platform to maintain viability of micro-dissected tumor slices in culture. *Biomicrofluidics*, 16(3), 034103; <https://doi.org/10.1063/5.0087532>
3. **Parsian, M.**, Mutlu, P., Yalcin, S. and Gunduz, U., 2020. Characterization of Gemcitabine Loaded Polyhydroxybutyrate Coated Magnetic Nanoparticles for Targeted Drug Delivery. *Anti-Cancer Agents in Medicinal Chemistry (Formerly Current Medicinal Chemistry-Anti-Cancer Agents)*, 20(10), pp.1233-1240. DOI: <https://doi.org/10.2174/1871520620666200310091026>
4. **Parsian, M.**, Mutlu, P., Yalcin, S., Tezcaner, A. and Gunduz, U., 2016. Half generations magnetic PAMAM dendrimers as an effective system for targeted

- gemcitabine delivery. *International journal of pharmaceutics*, 515(1-2), pp.104-113. <https://doi.org/10.1016/j.ijpharm.2016.10.015>
5. **Parsian, M.**, Unsoy, G., Mutlu, P., Yalcin, S., Tezcaner, A. and Gunduz, U., 2016. Loading of Gemcitabine on chitosan magnetic nanoparticles increases the anti-cancer efficacy of the drug. *European journal of pharmacology*, 784, pp.121-128. <https://doi.org/10.1016/j.ejphar.2016.05.016>
  6. Yalçın, S., Erkan, M., Ünsoy, G., **Parsian, M.**, Kleeff, J. and Gündüz, U., 2014. Effect of gemcitabine and retinoic acid loaded PAMAM dendrimer-coated magnetic nanoparticles on pancreatic cancer and stellate cell lines. *Biomedicine & Pharmacotherapy*, 68(6), pp.737-743. <https://doi.org/10.1016/j.biopha.2014.07.003>
  7. Unsoy, G., Yalcin, S., Khodadust, R., **Parsian, M.**, Mutlu, P., Bayanbold, K. and Gunduz, U., 2014. PAMAM dendrimer coated MNPs for siRNA delivery and gene silencing. *J Cancer Stud Ther*, 1(1), pp.1-5. [J. Cancer Stud. Ther.](#)

- **Abstracts Published in International Conferences**

1. Yalçın, GD., **Parsian, M.**, Akolpoğlu, DD., Mutlu, P., Gunduz, U. “2D and 3D Breast Cancer Cells Respond Differently to Chemotherapeutic Drug Palbociclib” – Conference Abstract. [FEBS Congress, 2019](#)
2. **Parsian, M.**, Mutlu, P., Yalcin, S., Gunduz, U. “Stability and pH Dependent Release Pattern of Gemcitabine Loaded Polyhydroxybutyrate Magnetic Nanoparticles” – Conference Abstract. [EurasianBioChem, 2019](#)
3. Değirmenci, B., Tübcil, MS., **Parsian, M.**, Gunduz, U. “3D Cell Culture Method by Using Magnetic Levitation for Breast Cancer Treatment” – Conference Abstract. [EurasianBioChem, 2019](#)
4. Tübcil, MS., Değirmenci, BS., **Parsian, M.**, Gunduz, U. “Comparison of Magnetic Levitation Method in 2D and 3D Hela Cell Culture Models for its Effectiveness in Cervical Cancer” – Conference Abstract. [EurasianBioChem, 2019](#)
5. **Parsian, M.**, Mutlu, P., Yalcin, S., Gunduz, U. “Targeting Ability and Internalization of Gemcitabine Loaded Polyhydroxybutyrate Coated Magnetic Nanoparticles on Breast Cancer Cell Lines” – Conference Abstract. [Cancer Research & Oncology Congress, 2018](#)
6. Yalçın, GD., Akolpoğlu, DD., **Parsian, M.**, Gunduz, U. “The Effects of Anti-cancer Agents on 2D and 3D cell cultures in Breast Cancer Cell Lines” – Conference Abstract. [MolBiyoKon, 2018](#)

7. **Parsian, M.**, Mutlu, P., Yalcin, S., Gunduz, U. “Polyhydroxybutyrate (Phb) Coated Magnetic Nanoparticles for Targeting Delivery of Gemcitabine” – Conference Abstract. [EurasianBioChem, 2018](#)
8. **Parsian, M.**, Atik, A., Dundar, M., Gunduz, U., Kulah, H., Ozgur, E., Yildirim, E. “On-Chip Insulated Micro Well Array for Cell Viability Assays” – Conference Abstract. [Microfluidics - EMBL, 2016](#)
9. Congun, F., Yildirim, E., **Parsian, M.** “Effect of Preheating on Channel Geometry and Surface Texture in Fabrication of Plastic Microfluidic Chip by Ultrasonic Hot Embossing” – Conference Abstract. [Microfluidics - EMBL, 2016](#)
10. **Parsian, M.**, Mutlu, P., Yalcin, S., Tezcaner, A., Gunduz, U. “Magnetic PAMAM Dendrimers for Targeted Gemcitabine Delivery” – Conference Abstract. [MolBiyoKon, 2015](#)
11. **Parsian, M.**, Mutlu, P., Yalcin, S., Tezcaner, A., Gunduz, U. “Magnetic Half Generation PAMAM Dendrimeric Nanoparticles for Targeting Delivery of Gemcitabine” – Conference Abstract. [ISOPS-11, 2015](#)
12. **Parsian, M.**, Taghavi PourianAzar, N., Yalcin, S., Mutlu, P., Gunduz, U. “Conjugation of Gemcitabine to Pamam Dendrimer-Coated Magnetic Nanoparticles For Targeted Delivery” – FEBS Journal 281 (Suppl.1) (2014) pp. 449. [FEBS-EMBO Congress, 2014](#)
13. **Parsian, M.**, Unsoy, G., Mutlu, P., Yalcin, S., Taghavi PourianAzar, N., Gunduz, U. “Chitosan-Coated Magnetic Nanoparticles as Vehicles for the Delivery of the Antitumor Drug Gemcitabine” – FEBS Journal 281 (Suppl.1) (2014) pp. 445. [FEBS-EMBO Congress, 2014](#)
14. Taghavi Pourianazar, N., **Parsian, M.**, Unsoy, G., Yalcin, S., Gunduz, U. “Comparison of two polymeric nanocarriers for targeted CpG-ODN delivery: chitosan and poly (amidoamine) dendrimer-coated magnetic nanoparticles” - FEBS Journal 281 (Suppl.1) (2014) pp. 449. [FEBS-EMBO Congress, 2014](#)
15. S. Yalcin, P. Mutlu, G. Unsoy, **M. Parsian**, N. Taghavi, Pourianazar, U. Gunduz. “Cellular Internalization Of Polyhydroxybutyrate Coated Magnetic Nanoparticles In Skbr-3 Cell Lines” – FEBS Journal 281 (Suppl.1) (2014) pp. 444. [FEBS-EMBO Congress, 2014](#)
16. Yalcin, S., Unsoy, G., Mutlu, P., Khodadust, R., Taghavi Pourianazar, N., **Parsian, M.**, Gunduz, U. “The cytotoxic analysis of free doxorubicin and doxorubicin loaded PHB-MNPs on sensitive and doxorubicin resistant MCF-7 cell lines” – FEBS Journal 281 (Suppl.1) (2014) pp.507. [FEBS-EMBO Congress, 2014](#)
17. Unsoy, G., Khodadust, R., Yalcin, S., Mutlu, P., Taghavi Pourianazar, N., **Parsian, M.**, Gunduz, U. “Effect of doxorubicin loaded CS MNPs on cell

proliferation in sensitive and doxorubicin resistant MCF-7 cell lines” – FEBS Journal 281 (Suppl.1) (2014) pp. 457. [FEBS-EMBO Congress, 2014](#)

- **Abstracts Published in National Conferences**

1. **Parsian, M.**, Mutlu, P., Taghavi Pourianazar, N., Yalcin, S., and Gunduz, U. “Cytotoxic Effect of Palbociclib Conjugated PAMAM Dendrimer Coated Magnetic Nanoparticles on Different Types of Breast Cancer Cell Lines”- Oral Presentation. [NANOTR16](#)
2. **Parsian, M.**, Mutlu, P., Gunduz, U. “Cellular Uptakes Studies of PAMAM Dendrimers Coated Magnetic Nanoparticles on 2D and 3D cell Cultures” – Conference Abstract. [MOKAD, 2021](#)
3. **Parsian, M.**, Mutlu, P., Gunduz, U. “Conjugation of Palbociclib to PAMAM Dendrimer Coated Magnetic Nanoparticles for Targeted Drug Delivery” – Conference Abstract. [MOKAD, 2021](#)
4. **Parsian, M.**, Mutlu, P., Yalcin, S., Gunduz, U. “Comparison of Different Magnetic Nanoparticles as an Effective Gemcitabine Delivery System for Breast Cancer” – Oral Presentation. [Biotechnology Congress, 2019](#)
5. **Parsian, M.**, Mutlu, P., Yalcin, S., Tezcaner, A., Gunduz, U. “Gemsitabin Yüklü Yarım Jenerasyon PAMAM Dendrimer Kaplı Manyetik Nanoparçacıkların Meme Kanseri Hücre Hatları Üzerindeki Sitotoksik Etkileri” – Conference Abstract. [Yaşam Bilimleri Sempozyumu, 2016](#)
6. Yalcin, S., Unsoy, G., Mutlu, P., Khodadust, R., Taghavi, N., **parsian, M.**, Gunduz, U. “Doksorubisin Yüklü Kitosan Manyetik Nanoparçacıkların Hücre İçerisine Girmesi ve Hücre Çoğalmasını Önlemesi” – Conference Abstract. [METU-Biotechnology, 2014](#)
7. Taghavi, N., **Parsian, M.**, Unsoy, G., Yalcin, S., Gunduz, U. “CpG-ODN taşıyıcıları olarak kitosan. ve poli(amidoamin) dendrimer-kaplı manyetik nanoparçacıkların karşılaştırılması” – Conference Abstract. [METU-Biotechnology, 2014](#)
8. **Parsian, M.**, Unsoy, G., Mutlu, P., Yalcin, S., Taghavi, N., Gunduz, U. “Anti-kanser İlacı Gemsitabin’in Taşınmasında Kitosan Kaplı Manyetik Nanoparçacıkların Kullanılması” – Conference Abstract. [METU-Biotechnology, 2014](#)
9. **Parsian, M.**, Taghavi, N., Yalcin, S., Unsoy, G., Mutlu, P., Gunduz, U. “İlaç Hedeflemesinde Gemsitabin Yüklü PAMAM Dendrimer Kaplı Manyetik Nanoparçacıkların Kullanılması” – Conference Abstract. [METU-Biotechnology, 2014](#)